APTw imaging in paediatric brain tumours: no waste of time and energy

Assessment of precision and feasibility at 3T and 7T MRI

I.V. Obdeijn

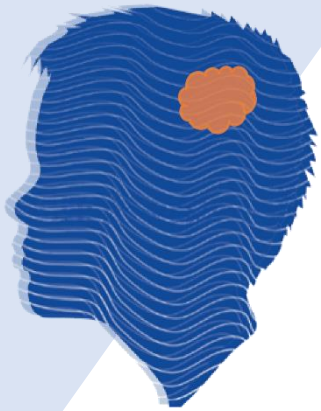

Master thesis
3 December 2021

Technical Medicine – Medical Imaging and Interventions
Neuro-oncology – Princess Máxima Centre
High Field MRI Group – UMC Utrecht

Graduation committee

Chairman:
Prof. Dr. Ir. B. ten Haken

Medical Supervisor:
Dr. M.H. Lequin

Technical Supervisors UMCU:
Dr. Ir. J.P. Wijnen
Dr. Ir. E.C. Wiegers

Technical Supervisor UT:
Dr. Ir. L. Alic

Process Supervisor:
Dr. M. Groenier

Extra Supervisor:
Dr. Ir. A.M. Leferink

Acknowledgements

It always seems impossible until it's done – Nelson Mandela

Almost one year ago I got the opportunity to combine my interest for paediatric neuro-oncology with the clinical implementation of advanced MR techniques. For me, the ultimate goal is to improve the healthcare of children to offer them future prospects by deploying advanced technology. During this year, I got fascinated by working for and with critically ill children. These children strengthened my intrinsic drive to get everything out of my internship in both the clinical and research area.

My deep gratitude go to Maarten, Jannie and Evita who gave me the opportunity to graduate in the field of paediatric neuro-oncology, which has stolen my heart. Maarten, the way you provided me insights in the clinical work, which also consists of difficulties and pitfalls, was always passionate and that motivated me. Furthermore, you involved me in the clinical work and the translation of my research into clinical practice, which I really appreciated. Jannie and Evita, you gave me the trust to became the go-getter regarding the clinical study. This gave me confidence in the contact with physicians, researchers and patients, but above all I had the feeling that I could complement the research team as technical physician. Jannie, you made me feel comfortable in situations I felt insecure or saw trouble looming ahead by helping me defining proper and realistic goals. In addition, you always wanted to think along in a pragmatic and creative way, which encouraged me to come up with new ideas. Evita, you were always approachable for a discussion in which I could share my ideas, but also my insecurities. In our conversations you always tried to put my thoughts and suggestions on the first place with the result that the research really has become my project.

Furthermore, I want to thank my supervisors from the university. Lejla, I am grateful for your critical, dedicated and honest feedback to get most out of the research. You always had time to discuss and I learned a lot from your perspective on scientific writing to improve my thesis. Marleen, you guided me to take steps in my personal development past year. You showed me even more about the importance of job satisfaction and the balance between rational thinking and emotional thinking. This have resulted in more self-acceptance and self-love.

There are many more people I want to thank, but some in particular. Sabine, your willingness and enthusiasm to share your expertise on paediatric brain tumours during outpatient clinic have enhanced my clinical knowledge, thank you. Maxime, my trusted roommate, I appreciated your sympathetic ear and motivating talks in both fun and stressful situations. Lastly, I am grateful to my parents for the opportunity they gave me to study. Through the year they encouraged and supported me with trust and love, which enabled me to continue my graduation with enthusiasm.

Abstract

INTRODUCTION: Brain tumours are the most prevalent type of solid tumours among children. During treatment brain tumours are evaluated with conventional MRI. However, conventional MRI is not always conclusive in the evaluation of treatment response in paediatric brain tumours. From clinical perspective timely differentiation between tumour progression and treatment effects is essential to prevent overtreatment and premature discontinuation of treatment. To improve diagnosis and treatment evaluation of paediatric brain tumours non-invasive characterisation of tumour metabolism could offer a solution. Amide proton transfer weighted (APTw) imaging has potency to become an imaging biomarker for treatment response. However, present applications of APTw imaging are evaluated in adult brain tumours not allowing direct translation to the paediatric population. Furthermore, for application of APTw imaging in clinical decision making insight in precision is required.

OBJECTIVES: To investigate to what extent APTw imaging can aid in the evaluation of treatment in paediatric brain tumours considering the precision in a phantom and healthy subjects at both 3T and 7T MRI. In addition, feasibility of APTw imaging at 7T MRI is assessed in paediatric brain tumours.

MATERIAL AND METHODS: APTw images belonging to the phantom and healthy subjects were acquired at 3T and 7T. APTw images at 3T include four z-spectrum acquisitions, i.e. 9 z-spectral points (clinical protocol), 15 z-spectral points, 23 z-spectral points and a full z-spectrum (36 z-spectral points), while at 7T only a full z-spectrum (35 z-spectral points) was acquired. The APTw images of three paediatric patients were obtained at 7T with a full z-spectrum acquisition. Depending on the acquisition protocol, normalized and B_0-corrected z-spectra were processed pixel-wise by MTR_{asym} and/or Lorentzian fitting to obtain APTw maps.
To assess precision, the APTw images for phantom and healthy subjects were acquired twice with an interval of one week. The phantom contained five submerged falcon tubes with solutions of nicotinamide (20, 50 and 100 mM), glutamate (10 mM) and glycine (20 mM) at brain pH. APTw images in supratentorial and infratentorial brain region were acquired in five healthy subjects. The root-mean-squared deviation (RSMD) and within-coefficient-of-variation (wCV) were calculated for the phantom and healthy subjects based on average APTw values in different regions of interest (i.e. solutes, brain regions and brain tissue types). To assess the feasibility, longitudinal APTw maps of three children with a brain tumour were obtained at 7T. The longitudinal changes in average APTw value inside tumours were evaluated by calculating the percentage change between time points.

RESULTS: APTw maps generated by Lorentzian fitting at both 3T and 7T show the potential to discern longitudinal difference in APTw values concerning precision, wCV ≤ 20%. Besides, processing of z-spectra with Lorentzian fitting improved the repeatability. The repeatability is not affected by the brain region (i.e. supratentorial or cerebellum) and tissue type (i.e. grey matter and white matter). Nevertheless, the repeatability drops when considering small volume of brain tissue segments. Longitudinal change in average APTw values of paediatric brain tumours were superior to the intrasubject variability. Most striking is one patient in which the average APTw value increased over time, with no measurable change in tumour volume.

CONCLUSION: APTw maps belonging to the full z-spectrum acquisition and processed with Lorentzian fitting, facilitate the use of APTw imaging as an imaging biomarker for brain tumour metabolism. The APTw maps of paediatric brain tumours seem to indicate the feasibility of APTw imaging at 7T in the detection of changes in paediatric brain tumour metabolism.

KEYWORDS: APTw magnetic resonance imaging, paediatric brain tumours, precision, feasibility.

Table of content

List of figures

List of tables

Abbreviations

^{31}P MRS	phosphorus magnetic resonance spectroscopy
AC-PC	anterior commisure – posterior commisure
APT	amide proton transfer
APTw	amide proton transfer weighted
B_0	static magnetic field
B_1	radiofrequency pulse amplitude
CEST	chemical exchange saturation transfer
CSF	cerebral spinal fluid
DIPG	diffuse intrinsic pontine glioma
DLGNT	diffuse leptomenigeal glioneuronal tumour
DS	direct water saturation
FWHM	full width half maximum
GLU	glutamate
GLY	glycine
GM	grey matter
LF	lorentzian fitting
LGG	low grade glioma
MITCH	metabolic imaging of tumours in children
MNI	montreal neurological institute
MRI	magnetic resonance imaging
MT	magnetization transfer
MTR_{asym}	magnetization transfer ratio asymmetry
NAM	nicotinamide
NOE	nuclear overhauser effect
OPG	optic pathway glioma
PTR	proton transfer ratio
RAN(P)O	response assessment in neuro (paediatric) oncology
RF	radiofrequency
RMSD	root mean squared deviation
ROI	region of interest
S_0	unsaturated z-spectral point
SEGA	subependymal giant cell astrocytoma
S_{sat}	saturated z-spectral point
WASABI	water shift and B_1
wCV	within coefficient of variation
WM	white matter

1 Introduction

Clinical background of paediatric brain tumours

Approximately 120 children are diagnosed with a brain tumour in the Netherlands every year [1]. In paediatric oncology, tumours in the central nervous system are the most common type of solid tumours worldwide and have the highest mortality rate of approximately 30% [2][3][4][5]. Paediatric brain tumours compromise a large heterogeneous group considering anatomy and biology. The histopathological tumour type, tumour location, tumour size and age at time of diagnosis influence the prognosis [6]. Low-grade gliomas (LGG) are the most common in the paediatric population (> 40%) and are accompanied with 10-year overall survival rate around 90% [2][7][8]. Diffuse intrinsic pontine gliomas (DIPGs) are most lethal, showing a mean overall survival rate of 8-11 months [9][10].

Tumour location, tumour growth rate and tumour size determine the presentation of symptoms. Non-specific symptoms such as headache, nausea or vomiting, epileptic seizures and diplopia arise as a result of increased intracranial pressure. Specific symptoms correlate with the tumour location, for example tumours in the cerebellum could cause hydrocephalus resulting in symptoms such as ataxia and hemiparesis and tumours in the midline or suprasellar region could cause visual impairment and endocrinopathies [11][12][13]. The gold standard to diagnose tumours in paediatric neuro-oncology is magnetic resonance imaging (MRI) in combination with histopathology. Ideally, the tumour is completely resected. However, complete resection is often challenging or impossible due to the location and/or invasive nature of the tumour with the consequence that adjuvant chemotherapy and/or radiotherapy must be considered [14][15][16].

Conventional MR imaging in paediatric brain tumours

During treatment, brain tumours are monitored with conventional MRI (e.g. T2w, FLAIR and Gd-T1w) to evaluate treatment response. For the evaluation of paediatric brain tumours the Response Assessment in Paediatric Neuro-Oncology (RAPNO) working group developed guidelines, regarding e.g. tumour size and contrast enhancement [17]. However, these criteria are not always conclusive in terms of tumour activity and treatment effects, e.g. pseudoprogression as a benign therapy effect that mimics tumour progression on conventional MRI [18][19][20]. Tumour progression requires revision of the treatment to pursue curative treatment but pseudoprogression, on the other hand, is treated conservatively. Therefore, timely differentiation between treatment effects and true tumour progression is crucial to prevent an overtreatment of patients or a premature discontinuation of treatment. Non-invasive detection of tumour activity and aggressiveness, and underlying tumour changes at the metabolic level will aid in clinical decision making concerning diagnosis and treatment evaluation.

Non-invasive characterisation of paediatric brain tumour metabolism: APTw imaging

Advanced MRI sequences can contribute to the non-invasive characterisation of paediatric brain tumour metabolism. Amide proton transfer weighted (APTw) imaging is a MR technique providing information about tissue-bound mobile proteins and peptides levels. APTw maps demonstrate a great correlation with the histopathological cell proliferation marker Ki-67 [21][22]. Therefore, APTw maps seem to be an auspicious imaging biomarker for tumour activity and tumour aggressiveness at the metabolic level.

Promising clinical applications of APTw imaging in neuro-oncology include differentiation of low and high grade glioma [21][22][23][24][25]. Additionally, APTw imaging is also reported to differentiate between pseudoprogression and tumour progression in high grade gliomas [26][27]. Moreover, APTw imaging is reported as a potential imaging biomarker for the assessment of treatment effects in brain tumours [28][29][30][31][32]. However, all these studies are performed in adult brain tumours that are intrinsically different from paediatric brain tumours in terms of clinical, biological and radiological

appearance [33][34]. Consequently, the present applications of APTw maps are not directly translatable to the paediatric population, and need careful evaluation to identify its applicability in this population.

Therefore, insight in precision[1] of APTw imaging in terms of repeatability[2] and reproducibility[3] is needed to distinguish true changes in APTw levels from intrasubject variability [35], which will enable clinical decision making regarding treatment effects in paediatric brain tumours. Repeatability and reproducibility of APTw imaging is addressed earlier in general terms [36][37]. However, the effect of acquisition method, processing method and magnetic field strength on the precision of APTw imaging is not evaluated yet. Compared to 3T MRI, APTw imaging at 7T MRI enables improved signal-to-noise-ratio, high spectral and spatial resolution within normal imaging time slots [38][39].

Aim of the study

Ultimately, we aim to assess paediatric brain tumour metabolism with APTw imaging to improve diagnosis and treatment evaluation. In this study we investigate to what extent APTw imaging at both 3T and 7T MRI can aid in the evaluation of treatment effects in paediatric brain tumours considering precision in a phantom and healthy subjects. Furthermore, feasibility of APTw maps as imaging biomarker for treatment response is assessed in children diagnosed with a brain tumour.

[1] Precision: degree of agreement between measured values obtained by repeated measurements with uniform or similar measurement conditions

[2] Repeatability: the measurement precision determined with the repetition of measurements with uniform conditions (i.e. procedure and instrument) in a short period of time

[3] Reproducibility: the measurement precision determined with the repetition of measurements with varying conditions (i.e. procedure and instrument) in a short period of time

2 Background APTw imaging

2.1 General principles of APTw imaging

Amide proton transfer weighted (APTw) imaging is a non-invasive MR technique based upon chemical exchange saturation transfer (CEST) providing information about peptide and proton levels in the tissue. CEST is an advanced MR technique in which exogenous or endogenous compounds are detected through an indirect reduction of the water signal [40]. The specific and indirect reduction of water is possible due to difference in resonance frequency for different molecules, known as chemical shift. Chemical shift arises due to difference in electron shielding of protons of a solute. Increased electron shielding results in a slightly lower magnetic field and thus a lower resonance frequency and vice versa. Since exchangeable solute protons of a certain compound resonate at a frequency that slightly different from water (chemical shift), these molecules can be selectively saturated through irradiation with frequency selective radiofrequency (RF) pulses [41][42]. The saturated molecules are in a temporary state showing no net magnetization [42]. Subsequently, saturated protons are exchanged with unsaturated protons from bulk water causing attenuation of the water signal. Since the pool of exchangeable solute protons is small relative to the water pool, each saturated proton of the exchangeable solute is replaced by a non-saturated proton of the water pool, which can be saturated again. The saturation time must be long enough to cause accumulation of saturated protons in the bulk water. As a result low concentration of solutes become visible indirectly [40][41][43]. The principle of saturation and magnetization transfer is present in Figure 2.1.

Important factors that affect the attenuation of the water signal, also known as the proton transfer ratio (PTR), are the exchange rates between the protons of the solute and bulk water, the saturation time and longitudinal relaxation. Increase in exchange rate induces more attenuation of the water signal and prolonged saturation causes more saturated protons in bulk water, both making the CEST effect more pronounced [41]. The longitudinal relaxation indicates the regrowth of longitudinal magnetization after saturation ensuing prolonged storage of saturation at a longer T_{1w}. Consequently, the longitudinal relaxation of water limits the saturated state and therefore the proton transfer ratio [41]. The PTR can be expressed with Equation 2.1.

$$PTR = x_s \cdot \alpha \cdot k_{sw} \cdot T_{1w}(1 - e^{\frac{-t_{sat}}{T_{1w}}}) \tag{2.1}$$

With x_s the fractional concentration of solute protons, α the saturation efficiency, k_{sw} the exchange rate from solute protons to water protons, t_{sat} the saturation time and $\frac{1}{T1w}$ the longitudinal relaxation [41]. To obtain APTw maps the tissue is irradiated with different RF offsets causing saturation and transfer of protons belonging to molecules resonating at the specific offset. The normalized water saturation is

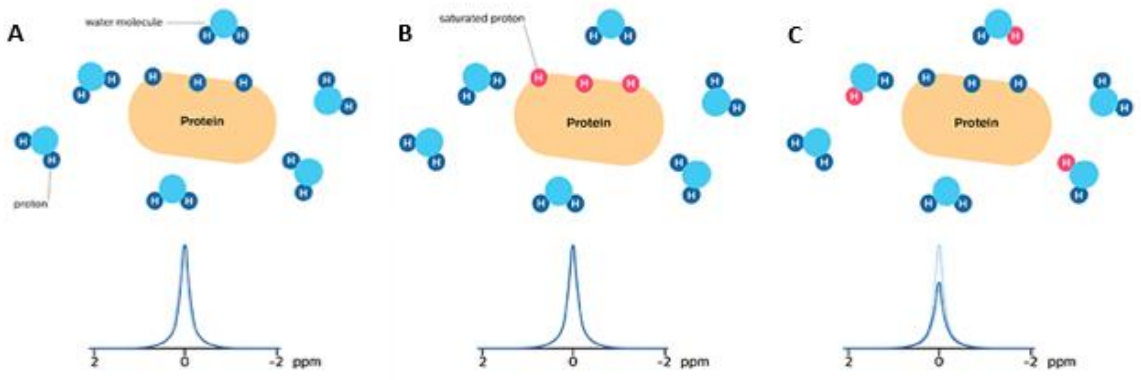

Figure 2.1: Principle of chemical exchange saturation transfer incorporating (a) unsaturated state (b) saturated state and (c) after magnetization transfer. The bottom row shows the effect of the saturation and magnetization transfer on the proton spectrum [43].

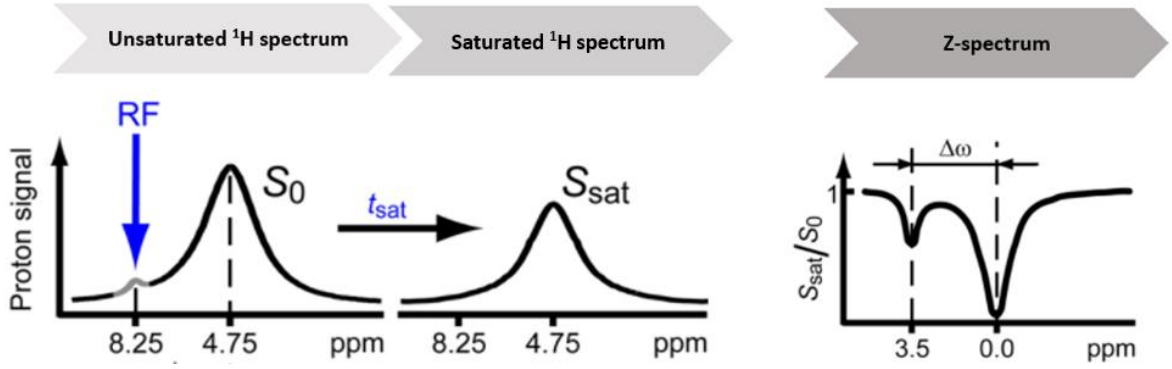

Figure 2.2: Z-spectrum acquisition with the effect on proton spectrum when saturating with a specific RF pulse and full z-spectrum obtained with RF pulses of multiple frequencies (x-axis: frequency of the RF pulse (ppm); y-axis: normalized water signal)[40].

determined (S_{sat}/ S_0; S_{sat} is the saturated water signal and S_0 is the unsaturated water signal) for the different offsets, by dividing the water signal (amplitude of the water peak in the proton spectrum) before saturation by the water signal after saturation [41]. The normalized water saturation is plotted as a function of the offset frequency, known as the z-spectrum [40][41]. Illustration of the steps to acquire a z-spectrum is present in Figure 2.2. Since the difference in resonance frequency between solute protons and water, is in the order of a few hundred to a few thousand Hertz (Hz) and the reference frequency (i.e. used magnetic field strength) is measured in MHz, difference in the frequencies of the RF pulses is expressed in units of ppm making it independent of the field strength. Symmetry of the z-spectrum is present around the water resonance frequency and therefore 0 ppm is assigned to the water frequency in CEST imaging. The other resonance frequencies are scaled with respect to the water frequency

To quantify endogenous contrast, i.e. obtaining APTw maps, CEST metrics are used. For quantification it is necessary to cancel out competing effects, among which magnetization transfer effect (MT) and direct water saturation (DS). MT arises because of magnetization transfer of saturated protons of semi-solid macromolecules and non-saturated water protons. When water is saturated directly by the RF pulse, it is referred to as DS. Elimination of these effect can be achieved by post-processing with CEST metrics, such as magnetic transfer ratio asymmetry (MTR_{asym}) or Lorentzian fitting. CEST quantification images based on MTR_{asym} compare the water signal reduction on opposite spectral positions ($+\Delta\omega$ and $-\Delta\omega$ with respect to water) [40][41][44]. The MTR_{asym} can be calculated with Equation 2.2.

$$MTR_{asym}(+\Delta\omega) = \frac{S_{-\Delta\omega} - S_{+\Delta\omega}}{S_0} \tag{2.2}$$

$S_{+\Delta\omega}$ and $S_{-\Delta\omega}$ are the measured water signals after saturation with a specific RF pulse at $+\Delta\omega$ and $-\Delta\omega$, respectively. The chemical shift of amides (-NH) is around +3.5 ppm. Therefore, the MTR_{asym} for APTw imaging is performed at 3.5 ppm [40].

The other CEST quantification metric is Lorentzian fitting, were the z-spectrum is fitted by the sum of various Lorentzian functions. The Lorentzian functions are based on prior knowledge about the amplitude, full width half maximum (FWHM) and frequency offset for different endogenous contrasts [45]. The Levenberg-Marquardt algorithm is often used for the fitting of the parameters. Equation 2.3 shows the Lorentzian function according to this algorithm.

$$L_i(\Delta\omega) = A_i \frac{\frac{\Gamma_i^2}{4}}{\frac{\Gamma_i^2}{4} + (\Delta\omega - \delta i)^2} \tag{2.3}$$

L_i is the Lorentzian function corresponding to the offset frequency $\Delta\omega$. The amplitude A_i, full width half maximum Γ_i and the frequency shift from the free water protons δi are considered [46]. The Lorentzian fitting corresponding to MT, DS, nuclear overhauser enhancement (NOE) and APT are often used for the creation of quantitative CEST images. The NOE effect is caused by a change of transition through dipolar or magnetic coupling of proximity nuclei [24][47]. APTw maps are created by the selection of the APT fit of the z-spectrum.

Examples of APTw maps of brain tumours are present in Figure 2.3 and 2.4. Figure 2.3 shows the difference in APTw values between low and high grade glioma. Figure 2.4 illustrate the possibility to differentiate between true progression and pseudoprogression with APTw imaging.

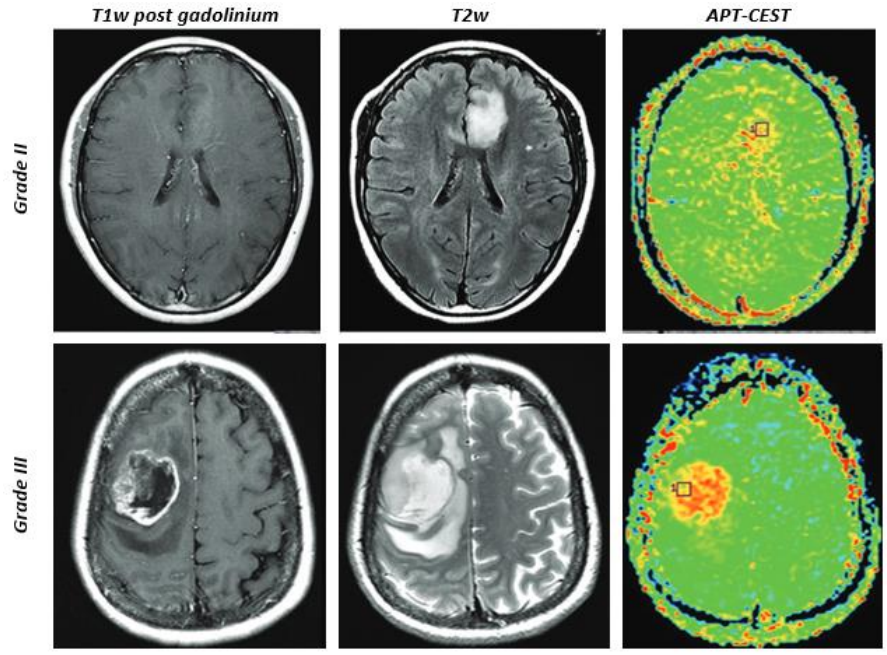

Figure 2.3: Low (upper row) and high (bottom row) glioma on conventional MRI (T1w post gadolinium and T2w) and APTw imaging. Difference is present between the APT levels of low and high grade glioma with MTR_{asym} values of 2.83% and 4.39% respectively. [21]

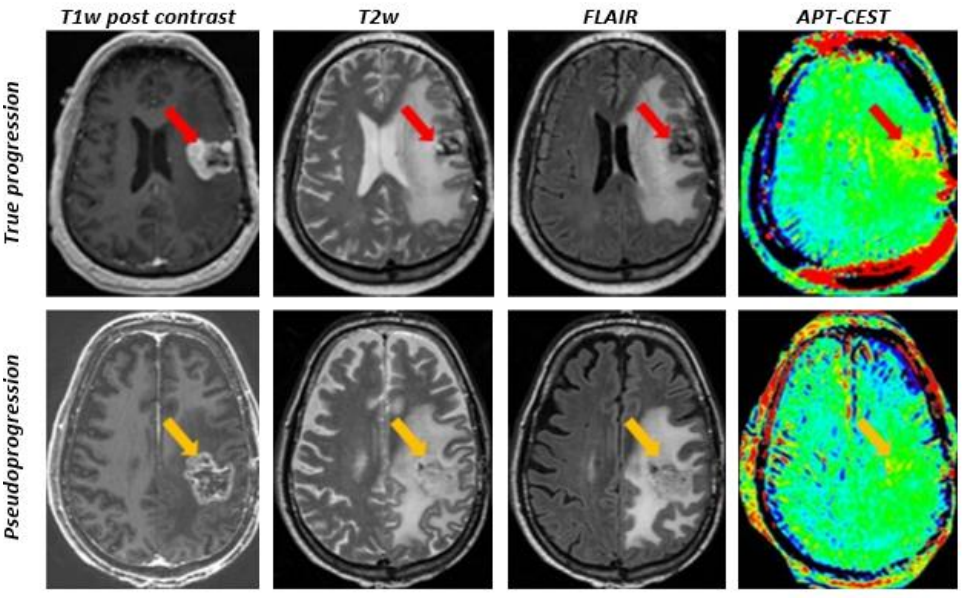

Figure 2.4: True progression (upper row) and pseudoprogression (bottom row) visualized with conventional (T1w post gadolinium, T2w and FLAIR) and APTw imaging. In both cases, true and pseudoprogression, contrast enhancement is present. Contrary, APT levels are higher in true progression in comparison with the APT levels in pseudoprogression. [26]

2.2 Acquisition APTw imaging at 3T with product and patch of Philips

To generate APTw maps, z-spectral images with different saturation frequencies densely sampled around the frequency of interest (i.e. ±3.5 ppm for APT), are acquired. Furthermore, dense sampling around the water frequency is required to correct for B_0-inhomogeneity. The acquisition of full z-spectrum at 3T is time consuming, since scan time is directly related to the number of offsets. Therefore, APTw imaging is hard to implement in clinical routine. Philips has developed an APT product making it possible to create APTw maps within 4 minutes. The designed protocol (APT product) for 3T uses only nine z-spectrum points (9p z-spectrum), saving scan time. Furthermore, the product includes online processing routines considering MTR_{asym}. With the APT product, z-spectral points are only determined around the offset frequency of interest, i.e. ±3.5 ppm for amides [43]. The APT product allows the acquisition of a z-spectrum using seven different frequency offsets, the two remaining sample points are used to acquire B_0-information. The acquisition at offset frequency +3.5 ppm was performed three times with different TEs ($\Delta TE = 0 \pm 0.4$ ms) to obtain a TSE-Dixon B_0-map. The B_0-map indicates the deviation (in ppm) between the measured frequency and the true frequency for each pixel, allowing correction. Figure 2.5 illustrate the z-spectrum when obtained with the APT product [48].

With the APT patch (extensions of the product) it is possible to make adjustment to the acquisition parameters. This allows to measure with different numbers of z-spectrum points and frequency stepsize, but also the free definition of the z-spectrum. With the free definition a full z-spectrum can be generated, suitable as a gold standard reference. Furthermore, acquisition with the patch allows to obtain raw data, enabling offline processing[43][48].

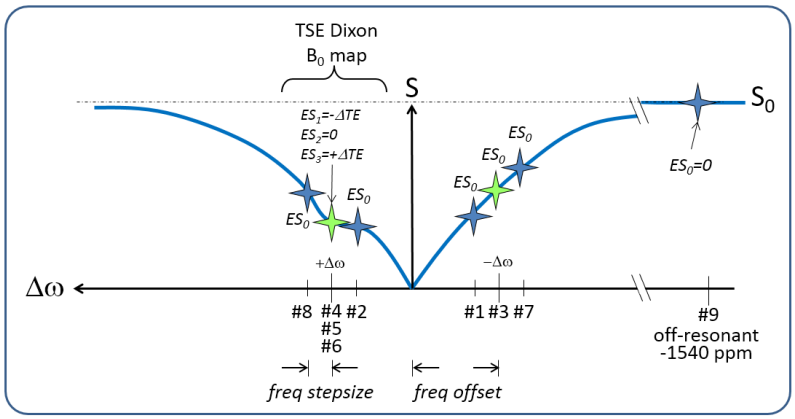

Figure 2.5: Illustration of z-spectrum sampling for APTw imaging when using the APT product (9 z-spectrum acquisitions) developed by Philips [43].

3 General image acquisition and processing

3.1 APTw image acquisition

For signal reception at the 3T system (Ingenia Elition X, Philips Healthcare, Best, The Netherlands) a 32-channel receive coil for the head was used. Transmission was performed with the bore-coil. Acquisition at the 7T system (Achieva, Philips Healthcare, Best, The Netherlands) was performed using a 32-channel receive-only and 8-channel transmit coil for the head (Nova Medical).

Acquisition at 3T system. The z-spectral images at the 3T system were obtained using the APT product in combination with the APT patch (extension of the APT product) developed by Philips Healthcare (detailed description in section 2.2). The z-spectral images were acquired with a 3D turbo spin echo sequence. Z-spectral images were created by using four different acquisition settings. The settings of the APT product were used; 9p z-spectrum with a frequency stepsize of 0.8 ppm around the frequency offset of 3.5 ppm. In addition two scans were performed with fifteen z-spectral points (15p z-spectrum) and twenty-three z-spectral points (23p z-spectrum) by applying a stepsize of 0.4 ppm around the frequency offsets of 3.5 ppm. To create a TSE-Dixon B_0-map for the 15p and 23p z-spectrum acquisitions the last six acquisitions were performed with different TEs (ΔTE = ± 0.4 ms). The last three acquisitions with positive frequency offset were used for the TSE-Dixon B_0-mapping. The final scan is performed with a full z-spectrum, including acquisition with thirty-six different frequency offsets disproportionally distributed across the spectrum. Table 3.1 shows the characteristics of the four different settings. The offsets are sampled by alternation between the positive and negative offsets.

All scans were performed with the following imaging parameters: TR = 5925 ms; TE = 8.3 ms; matrix = 128 x 128 x 10; FOV = 230 x 230 x 60 mm; resolution = 1.8 x 1.8 x 6.0 mm; flip angle = 90°. The RF pulse amplitude (B_1) is set to 2.0 µT and the saturation time equals 2000 ms for the APTw imaging at 3T.

Acquisition at 7T system. The z-spectral images at the 7T system were acquired with a 3D gradient echo sequence. Acquisition is performed for thirty-five different frequency offsets (Table 3.1). The sampling order is not arbitrary, since the offsets can be sampled from negative to positive offset (and vice versa) or by alternation between positive and negative offsets during sampling. The imaging parameters were TR = 3.75 ms; TE = 1.8 ms; matrix = 128 x 128 x 12; FOV = 256 x 256 x 24 mm; resolution = 2.0 x 2.0 x 2.0 mm; flip angle = 5°. The z-spectral images were acquired twice with different RF pulse amplitudes, 1.5 µT (low B_1) and 2.1 µT (high B_1). The saturation time equals 1400 ms (56 block pulses of 25 ms).

Table 3.1: Frequency offsets and scan duration of multiple APTw image acquisitions at 3T and 7T

	Frequency offsets (Δω) (ppm)	**Scan duration (min:s)**
9p z-spectrum acquisition	±2.70, ± 3.50 [+ 3.50 with three acquisition at different TEs], ± 4.30 and -1560.00*	03:45
15p z-spectrum acquisition	± 2.30, ± 2.70, ± 3.10, ± 3.50, ± 3.90 [-ΔTE], ± 4.30 [ΔTE=0], ± 4.70 [+ΔTE] and -1560.00*	06:08
23p z-spectrum acquisition	± 1.50, ± 1.90, ± 2.30, ± 2.70, ± 3.10, ± 3.50, ± 3.90, ± 4.30, ± 4.70 [-ΔTE], ± 5.10 [ΔTE=0], ± 5.50 [+ΔTE] and -1560.00*	09:18
Full z-spectrum acquisition†	0, ± 0.20, ± 0.27, ± 0.50, ± 1.17, ± 1.84, ± 2.60, ± 2.80, ± 3.00, ± 3.20, ± 3.34, ± 3.65, ± 3.80, ± 4.20, ± 6.71, ± 20.00, ± 40.00, ± 600.00* and -1560.00*‡	14:27 (3T) 04:51 (7T)

* Unsaturated z-spectral points (S_0) for offline normalization purposes (3T: Δω = -1560.00 ; 7T: Δω = ±600.00)
† Performed at 3T and 7T scanner. At 7T the acquisition is performed twice with different B_1-values.
‡ saturation with Δω = -1560 ppm is not performed at 7T. At 3T the APT patch is used for which it is advised to use Δω = -1560 ppm for normalization purposes during the acquisition.

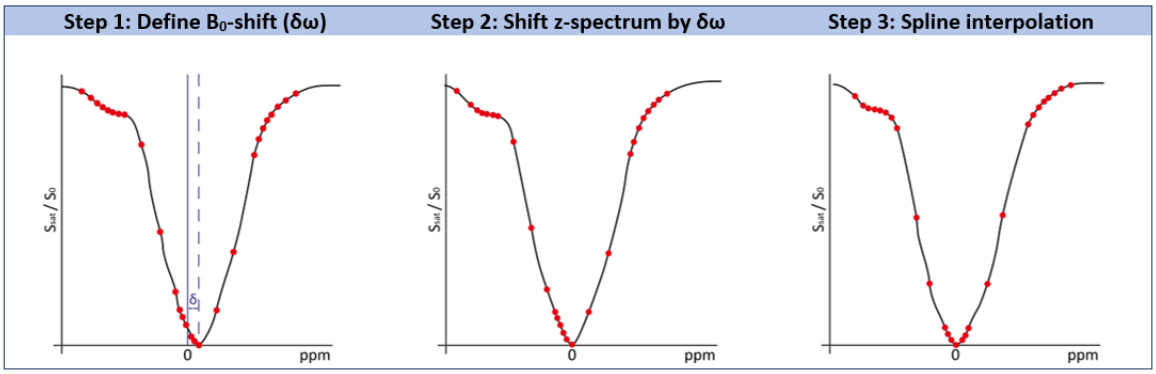

Figure 3.1: Visualization of B_0-correction which can be divided in three steps. From left to right: define B_0-shift (δω), shift z-spectrum by δω and spline interpolation of z-spectral points.

3.2 Image processing

All acquired z-spectra were normalized by dividing the saturated z-spectral points by the unsaturated z-spectral point (S_{sat}/S_0)(detailed in Table 3.1) followed by a three-steps procedure for B_0-correction as illustrated in Figure 3.1.

- Step 1: Identify the B_0-shift for each individual voxel. The resulting shift in ppm is characteristic for the B_0-inhomogeneity of the voxel concerned. The B_0-shift for the 9p, 15p and 23p z-spectrum acquisitions at 3T is defined by the TSE-Dixon B_0-map. The B_0-shift for the full z-spectrum at 3T is based on the TSE-Dixon B_0-map obtained during the acquisition of the 23p z-spectrum. The B_0-shift at 7T is obtained in another way by defining the position (ppm) of absolute minimum of the z-spectrum with respect to water resonance frequency (i.e. 0 ppm).
- Step 2: Voxel-wise shifting by the B_0-shift to align the z-spectral points with the position (ppm) at which they were actually measured.
- Step 3: Spline interpolation between the shifted z-spectral points to obtain a symmetric distribution of the z-spectral points with respect to 0 ppm and obtain the z-spectral points at the frequency offsets of interest as intended during acquisition (Table 3.1).

For z-spectra acquired with 9p, 15p and 23p, the APTw value was calculated by defining MTR_{asym} for amides at +3.5 ppm (Equation 2.2), resulting in APTw maps based on MTR_{asym} for each acquisition. For the full z-spectrum acquisition, at both 3T and 7T, the APTw value of each voxel was calculated in two ways, MTR_{asym} at +3.5 ppm and Lorentzian fitting using the Levenberg-Marquardt algorithm (Equation 2.3, Chapter 2). The Lorentzian fitting utilize independent distributions of different endogenous contrast, referred to as pools. To fit the full z-spectrum with Lorentzian functions prior knowledge of amplitude, full width half maximum (FWHM) and frequency offset of different pools (i.e. direct water saturation (DS), magnetization transfer (MT), nuclear overhauser effect (NOE), amines and amides (APT) and/or hydroxyl) was used [49][50]. The fitting parameters, including initial values, upper and lower boundaries, for 3T and 7T are listed in Appendix A. All image processing was performed with MATLAB (R2019b, The MathWorks, Natick: MA).

3.3 Quality assessment of z-spectrum

Inhomogeneities of the static magnetic field (B_0) and the radiofrequency transmit field (B_1) impact the quality of APTw maps, especially when applied at high magnetic field. Therefore, quality assessment of the z-spectrum is performed for the acquisition at 7T [39][51]. We performed an field mapping method, simultaneous mapping of water shift and B_1 (WASABI), to get information about the B_0- and B_1-inhomogeneity. Thereafter, fitting of the WASABI spectra was performed to obtain B_0- and B_1-maps. Detailed explanation of the WASABI acquisition and processing, including typical examples, are present in Appendix B. If the B_0- and B_1- maps indicate areas where the quality of the z-spectra is questioned, the z-spectra were checked by two researchers (I.V.O and E.C.W). Based on this information, the concerned areas were excluded in the quantitative analysis.

4 Phantom study

4.1 Materials and methods

4.1.1 Study design

The study (illustrated in Figure 4.1) was designed to test the repeatability and the reproducibility of APTw maps of a phantom at 3T and 7T MRI. For assessment of the repeatability two measurements were performed on both the 3T and 7T scanner using the same phantom within an interval of seven days. The reproducibility was evaluated by comparing the APTw maps belonging to different acquisition methods at 3T. The phantom contained different fluids, which made it possible to evaluate the specificity of the APTw imaging.

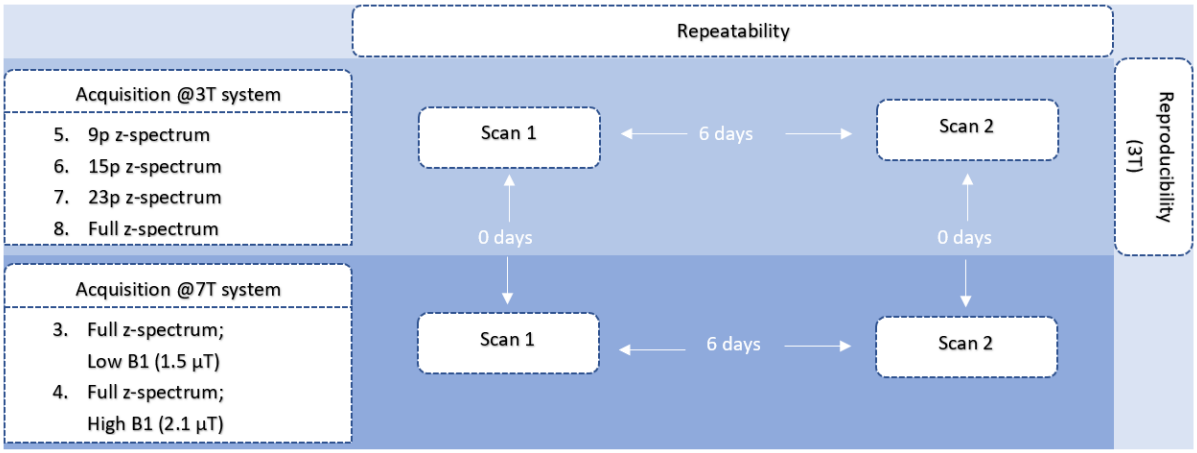

Figure 4.1: Scan-rescan protocol for phantom study to evaluate the repeatability and reproducibility of APTw maps. At 3T four acquisitions with different number of z-spectral points were performed twice. At 7T two acquisitions with different B1 were carried out at two time points.

4.1.2 Phantom characteristics

The phantom is a thermos flask filled with 0.9% saline solution, containing five falcon tubes consisting of different amide and/or amine concentrations. Amides contain a nitrogen atom connected to a carbonyl and amines are molecules containing carbon-nitrogen bonds [52]. Due to their different chemical composition and organization of electrons, the molecules have a different chemical shift (amides: ~3.5 ppm and amines: ~1.8-3.0 ppm) with respect to water [21]. The amide and amine solutes are solved in phosphate buffered saline (pH ~ 7.4). The pH influence the measured APTw value and therefore the fluids are titrated to a pH range of ~7.0 (brain pH) with hydrochloric acid [53]. pH was measured after each added drop of hydrochloric acid with pH indicator strips till the strip indicated the pH was ~7.0 (range of pH: 6.8-7.2). A description including a schematic drawing of the phantom is shown in Figure 4.2. Measurements of the phantom were performed at a room temperature.

Compound and concentration	Amide and/or amine?
20 mM NAM	Amides
50 mM NAM	Amides
100 mM NAM	Amides
10 mM Glu	Amides and amines
20 mM Gly	Amines
NAM = nicotinamide; Glu = glutamate; Gly = glycine	

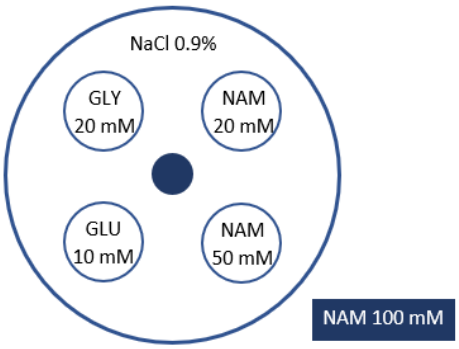

Figure 4.2: Schematic drawing of the phantom containing five different concentrations of solute amides and/or amines. Three concentrations of nicotinamide (NAM): 20 mM, 50 mM and 100 mM. A tube with 20 mM glycine (Gly) and a tube with 10 mM glutamate (Glu). The tubes were surrounded with 0.9 % saline solution(NaCl) [54][55][56]

4.1.3 APT-weighted image acquisition

APTw maps of the phantom were acquired according to the protocol described in Chapter 3, see Table 3.1, for both 3T and 7T. Screenshot of the planning of the acquisition slabs were used to ensure reproducible planning between the scan session and between 3T and 7T. The planning in the second scan session was executed in consensus of two researchers (I.V.O with J.P.W or E.C.W).

4.1.4 Image processing

Image processing starts with the normalization and B_0-correction of the z-spectra. Subsequently, the APTw maps were calculated by MTR_{asym} and/or Lorentzian fitting for each acquisition at 3T and 7T (described in section 3.2). The Lorentzian fitting incorporate six different pools (DS, MT, NOE, amines, amides (APT) and hydroxyl). The used prior knowledge regarding the Lorentzian fitting is listed in Table A.2 (3T) and Table A.4 (7T) of Appendix A.

Since the phantom consist of different concentrations of solute amides and/or amines three-dimensional cylindrical regions of interest (ROIs) were segmented, to evaluate the average APTw value in the different falcon tubes. The cylindrical ROIs with a radius of ten pixels, smaller ROI for 100 NAM with radius of five pixels, were draw manually in the unsaturated z-spectral image (Δω = -1560 ppm for 3T and Δω = ± 600.00 ppm for 7T) slice-wise, for each MR system and time point.

4.1.5 Data analysis

The APTw values, mean ± standard deviation, of the five ROIs were assessed for all acquisition, i.e. four acquisition at 3T (9p, 15p, 23p and full z-spectrum) and one acquisition at 7T, and time points separately based on the APTw maps. In case of the full z-spectrum acquisition the analysis was performed for both the MTR_{asym} and Lorentzian fitting.

The repeatability of all APTw maps was assessed by the root mean square deviation (RMSD)(Eq. 4.1), and by the within subject coefficient of variation (wCV)(Eq. 4.2). Both were calculated by pairs of repeated measurements at 3T and 7T using the averages of the five ROIs (n=5) for each acquisition and processing method. The reproducibility of APTw maps at 3T was assessed by the RMSD and by the wCV to signify differences between APTw maps originating from a full z-spectrum and APTw maps originating from 9p, 15p, 23p z-spectrum using the average APTw values of the five ROIs.

$$RMSD = \sqrt{\frac{\sum_{i=1}^{n}(x_{1,i} - x_{2,i})^2}{n}} \tag{4.1}$$

$$wCV = \frac{SD}{mean} \times 100\% \tag{4.2}$$

$$mean = \frac{\sum_{i=1}^{n} x_{1,i} + x_{2,i}}{2n} \tag{4.2.a}$$

$$SD = \sqrt{\frac{\sum_{i=1}^{n}(x_{1,i} - x_{2,i})^2}{2n}} \tag{4.2.b}$$

With x_1 and x_2 the average APTw values of each ROI for the different time points (repeatability) or acquisition methods (reproducibility) and n the number of ROIs.

4.2 Results

Figure 4.3 shows normalized and B_0-corrected z-spectra acquired with the full z-spectrum acquisition at 3T and 7T corresponding to the two acquisition sessions. As illustrated in Figure 4.3, the average z-spectra for all ROIs (i.e. 20 mM NAM, 50 mM NAM, 100 mM NAM, 10 mM Glu and 20 mM Gly) acquired at 3T are wider compared to the average z-spectra acquired at 7T. The higher the concentration of amides (20 to 100 mM NAM) the greater the drop in the z-spectrum around 3.5 ppm. No drop is visible in the full z-spectra of 10 mM Glu and 20 mM Gly at 3T. Contrary, the z-spectra of Glu and Gly show some small peaks around frequency offsets of amides (3.5 ppm) and amines (3 ppm). In Appendix C the z-spectra for each ROI and acquisition session are visualized separately.

APTw maps are considered repeatable for the different acquisitions at both 3T and 7T (Figure 4.4 and 4.5). However, the APTw maps belonging to the full z-spectrum acquisition processed with Lorentzian fitting at 3T show circular patterns, which are not equally distributed between the two sessions. The tubes containing 50 mM and 100 mM NAM show high APTw values compared to the tubes containing 20 mM NAM, 10 mM Glu and 20 mM Gly. The quantitative analysis of all acquisitions indicate that the

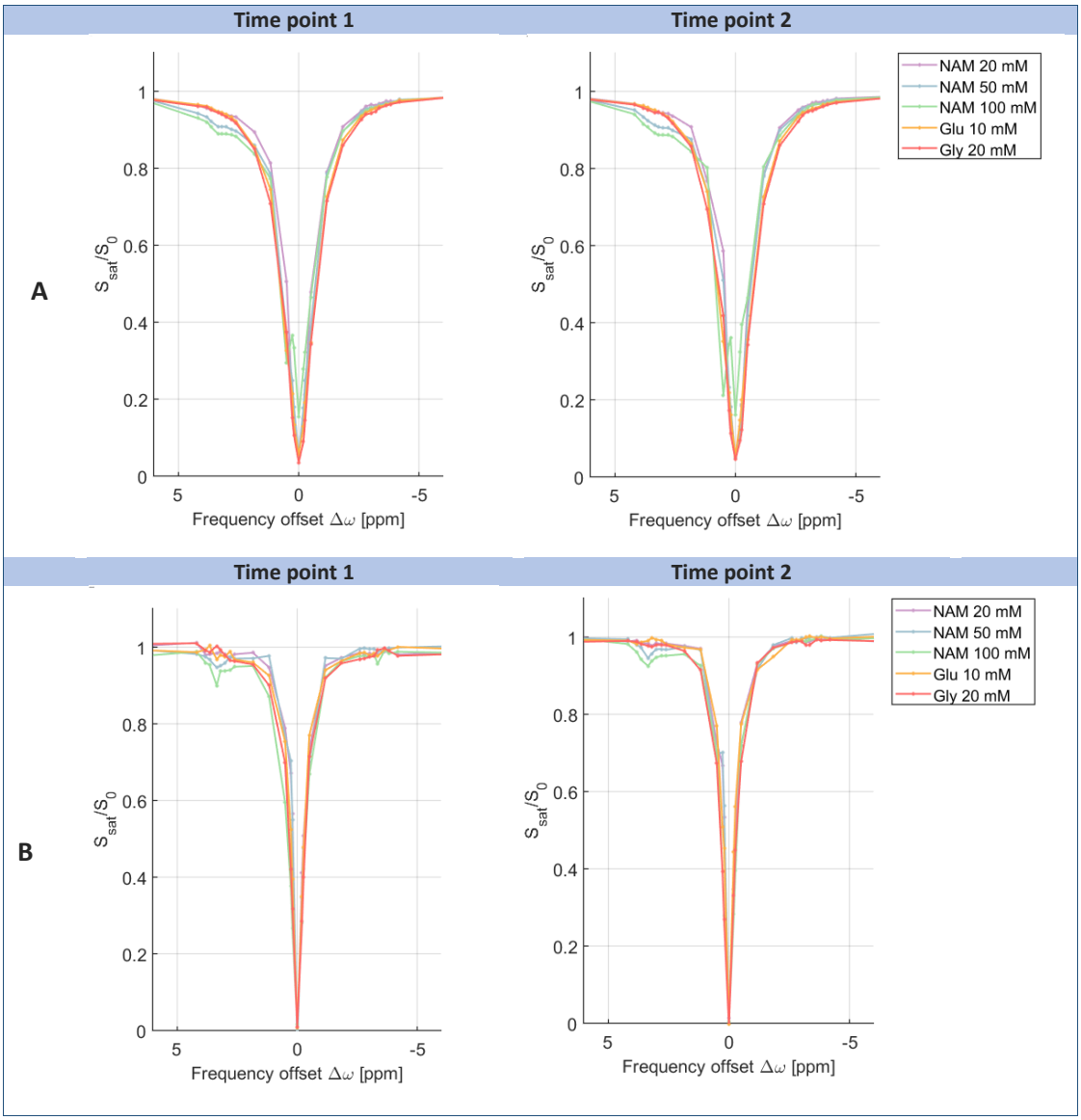

Figure 4.3: Visualization of the full z-spectrum acquisition at 3T (panel A) and 7T (panel B). Averaged z-spectra are present for five different ROIs (i.e. NAM 100 mM; NAM 50 mM; NAM 20 mM; GLU 10 mM; GLY 20 mM) belonging to time point 1 and time point 2.

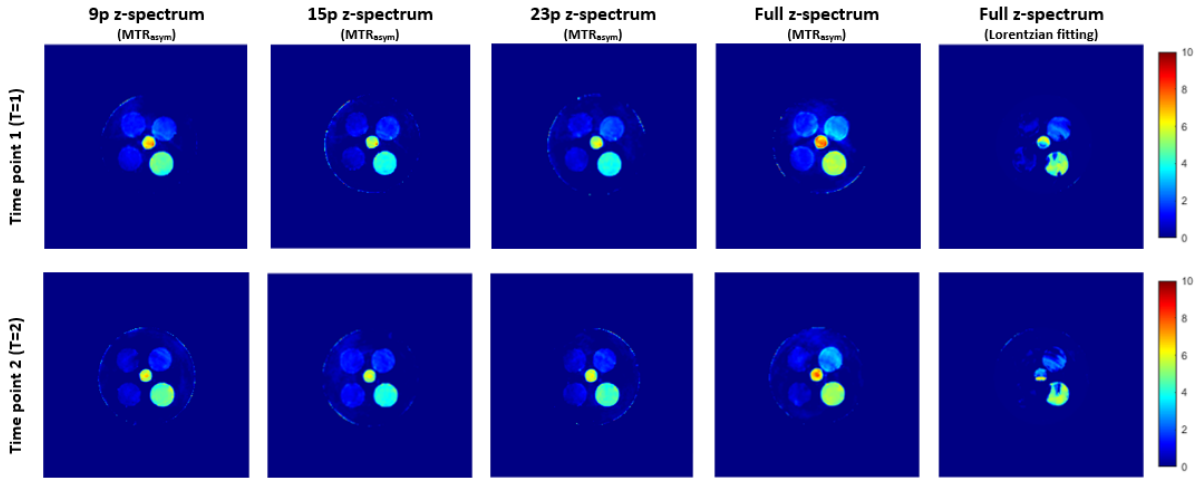

Figure 4.4: APTw maps based on MTR_{asym} and/or Lorentzian fitting for acquisition with nine, fifteen, twenty-three z-spectral points and full z-spectrum acquisition at 3T. Upper row present the APTw maps measured at time point 1 and the lower row present the APTw maps measured at time point 2.

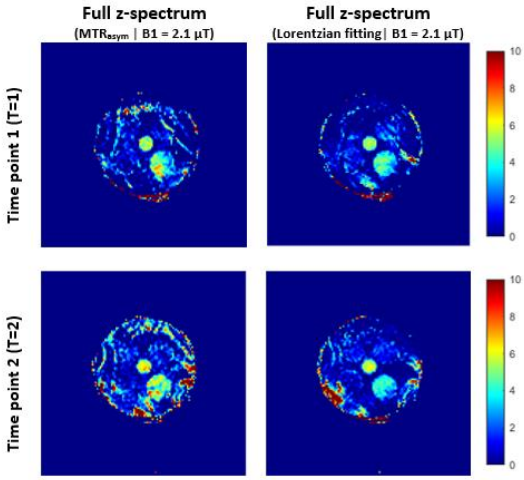

Figure 4.5: APTw maps based on MTR_{asym} and Lorentzian fitting for full z-spectrum acquisition at 7T (B_1 = 2.1 µT). Upper row present the APTw maps measured at time point 1 and the lower row present the APTw maps measured at time point 2.

APTw value in the 20 mM NAM is slightly higher than the values of 10 mM Glu and 20 mM Gly (Table 4.1). Furthermore, increase of the amide concentration results in a non-linear increase of APTw values.

The overall repeatability of the phantom for the different acquisitions and processing methods at 3T and 7T is supported by boxplots and repeatability metrics, shown in Figure 4.6 and Table 4.2 respectively. Furthermore, processing with Lorentzian fitting results in medians close or equal to zero for the 10 mM Glu and 20 mM Gly solutes suggesting diminished sensitivity. Remarkable is the difference in interquartile range of the boxplots related to the APTw values of the 50 mM NAM ROI based on the full z-spectrum acquisition at 3T and processed with Lorentzian fitting.

Comparison of the APTw values of the ROIs for the 9p, 15p, 23p and full z-spectrum acquisition at 3T constructed by MTR_{asym}, indicate that the 9p z-spectrum acquisition reproduces the full z-spectrum acquisition best (Figure 4.7). This is supported by both reproducibility metrics; RMSD and wCV (Table 4.3). The different acquisition methods do not have major impact on the APTw values measured in the 10 mM Glu and 20 mM Gly solutes.

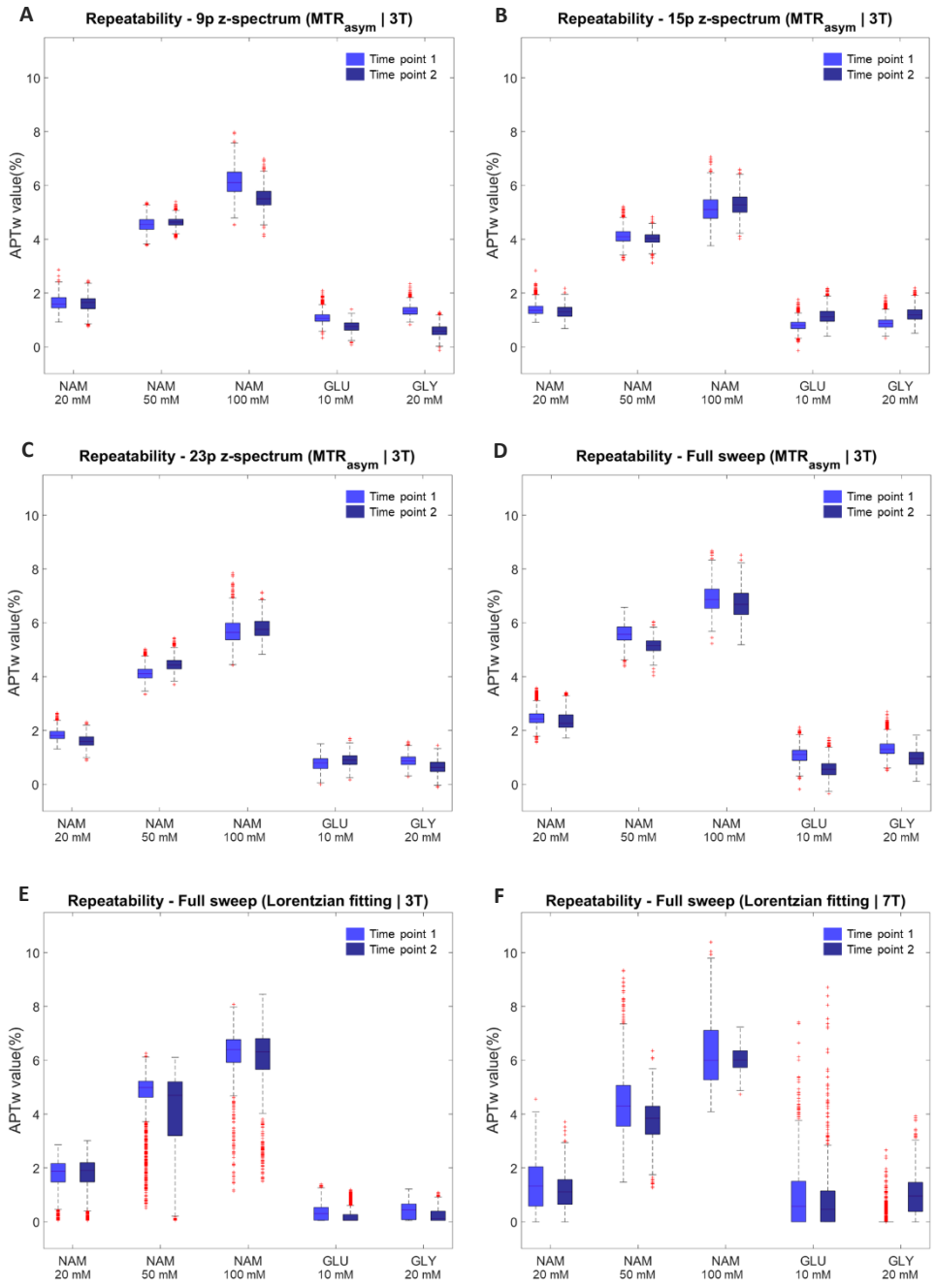

Figure 4.6: Boxplots for the different APTw acquisition and processing methods (A-E: 3T, F: 7T) to evaluate the repeatability of APTw values within each ROI.

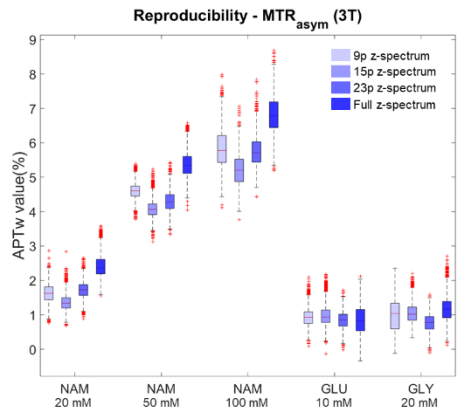

Figure 4.7: Boxplots for the different APTw acquisition at 3T (processed with MTR$_{asym}$) for the evaluation of the reproducibility of APTw values within each ROI.

Table 4.1: APTw values (mean ± standard deviation) for the different acquisitions at 3T and 7T. The APTw values correspond to five different ROIs measured at two time points.

APTw values (%) at 3T	NAM 20 mM (Mean ± STD)	NAM 50 mM (Mean ± STD)	NAM 100 mM (Mean ± STD)	Glu 10 mM (Mean ± STD)	Gly 20 mM (Mean ± STD)
APTw value based on 9p z-spectrum*					
Time point 1	1.65 ± 0.27	4.56 ± 0.27	6.16 ± 0.55	1.09 ± 0.20	1.35 ± 0.19
Time point 2	1.62 ± 0.27	4.64 ± 0.17	5.54 ± 0.42	0.75 ± 0.19	0.61 ± 0.21
APTw value based on 15p z-spectrum*					
Time point 1	1.39 ± 0.22	4.13 ± 0.27	5.15 ± 0.49	0.80 ± 0.20	0.89 ± 0.20
Time point 2	1.31 ± 0.23	4.02 ± 0.21	5.29 ± 0.43	1.15 0.27	1.22 ± 0.27
APTw value based on 23p z-spectrum*					
Time point 1	1.26 ± 0.46	4.04 ± 0.78	4.62 ± 1.62	1.12 ± 0.30	0.86 ± 0.42
Time point 2	1.61 ± 0.22	4.46 ± 0.23	5.78 ± 0.39	0.90 ± 0.23	0.65 ± 0.26
APTw value based on full z-spectrum*					
Time point 1	2.50 ± 0.32	5.61 ± 0.35	6.91 ± 0.53	1.08 ± 0.29	1.34 ± 0.31
Time point 2	2.38 ± 0.34	5.14 ± 0.25	6.72 ± 0.58	0.58 ± 0.32	0.99 ± 0.30
APTw value based on full z-spectrum+					
Time point 1	1.73 ± 0.62	4.77 ± 0.86	6.12 ± 1.11	0.35 ± 0.28	0.42 ± 0.30
Time point 2	1.73 ± 0.69	4.09 ± 1.54	5.95 ± 1.40	0.19 ± 0.21	0.24 ± 0.22
APTw values (%) at 7T	**NAM 20 mM (Mean ± STD)**	**NAM 50 mM (Mean ± STD)**	**NAM 100 mM (Mean ± STD)**	**Glu 10 mM (Mean ± STD)**	**Gly 20 mM (Mean ± STD)**
APTw value based on full z-spectrum*					
Time point 1	0.09 ± 2.16	3.30 ± 1.56	5.50 ± 6.08	-0.23 ± 2.03	0.36 ± 1.53
Time point 2	0.97 ± 1.04	4.47 ± 1.43	6.61 ± 0.86	1.19 ± 1.82	0.86 ± 1.51
APTw value based on full z-spectrum+					
Time point 1	1.36 ± 0.93	4.36 ± 1.32	6.35 ± 1.38	1.01 ± 1.27	0.11 ± 0.32
Time point 2	1.11 ± 0.67	3.76 ± 0.78	6.02 ± 0.46	0.84 ± 1.21	1.01 ± 0.79

* z-spectrum processed with MTR_{asym}
\+ z-spectrum processed with Lorentzian fitting

Table 4.2: Repeatability metrics of the phantom for the different APTw acquisitions and processing methods.

Magnetic field strength	Acquisition	RMSD	wCV (%)
3T	9p z-spectrum*	0.46	11.61
	15p z-spectrum*	0.23	6.48
	23p z-spectrum*	0.59	16.47
	Full z-spectrum*	0.36	7.63
	Full z-spectrum+	0.33	9.16
7T	Full z-spectrum*	1.06	32.49
	Full z-spectrum+	0.52	14.28

* z-spectrum processed with MTR_{asym}
\+ z-spectrum processed with Lorentzian fitting

Table 4.3: Reproducibility metrics of phantom by comparing the shortened APTw acquisitions (i.e. 9, 15, 23 z-spectral points) with the full z-spectrum acquisition both processed with MTR_{asym} at 3T.

Comparison acquisitions	RMSD	wCV (%)
9p z-spectrum vs full z-spectrum (3T)	0.69	15.97
15p z-spectrum vs full z-spectrum (3T)	1.08	26.01
23p z-spectrum vs full z-spectrum (3T)	1.08	26.05

5

In vivo study

5.1 Materials and methods

5.1.1 Study design

Repeatability and reproducibility of APTw maps of two locations of the brain, supratentorial and infratentorial, was assessed at 3T and 7T MRI. Difference in repeatability is mentioned for these brain regions, explained by the sensitivity of APTw maps to magnetic field inhomogeneity [36][57]. In particular APTw imaging of infratentorial regions are vulnerable due to air-tissue and air-bone transitions, which can induce susceptibility-associated B_0-inhomogeneities [58][59]. Figure 5.1 illustrates the study design. To determine the repeatability of APTw maps at 3T and 7T, each subject is scanned twice on both magnetic field strengths with an interval of one week. The reproducibility is assessed for multiple acquisition methods by comparing APTw maps acquired at the same day. In total five healthy subjects (mean age, 25.8 ± 1.7 years old; male: female ratio, 3:2) were included. The APTw data was processed by MTR_{asym} and/or Lorentzian fitting to obtain APTw maps. Quantitative analysis of the APTw maps is conducted by applying atlas-based segmentation of grey matter (GM) and white matter (WM).

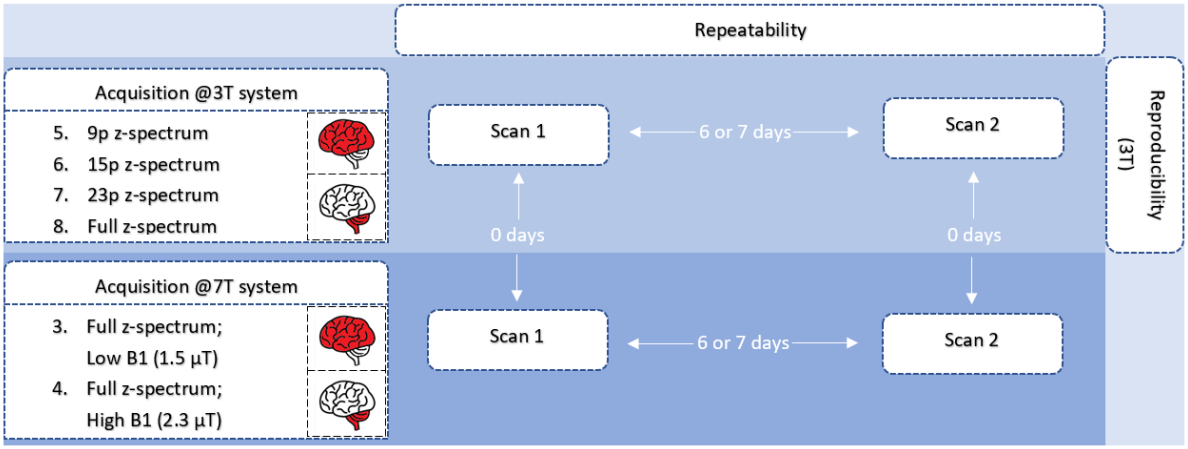

Figure 5.1: Scan-rescan protocol for in vivo study to evaluate the repeatability and reproducibility of APTw maps. At 3T four acquisitions with different number of z-spectral points were performed. At 7T two acquisitions with different B1 were carried out. At both 3T and 7T the acquisition were performed at two anatomical areas (supra- and infratentorial) and at two time points.

5.1.2 APT-weighted image acquisition

The acquisitions of APTw images were performed on 3T and 7T in agreement with the acquisition protocol described in Chapter 3, see Table 3.1. As illustrated in Figure 5.2, the APTw image acquisition scanned a partial brain (slab). Since two regions of interest are present, supratentorial (orange slab) and infratentorial (green slab), APTw maps of both regions were acquired for each APTw acquisition. The supra- and infratentorial region of the brain is separated by the tentorium cerebelli, respectively above and below the tentorium cerebelli [60].

The slab positioning is based on anatomical brain landmarks on T1w images. The first slice of the supratentorial slab (orange slab) is positioned through the anterior commissure- posterior commissure line (AC-PC line) [61]. The last slice of the infratentorial slab (green slab) is placed in line with the superior pontine notch and the inferior edge of the quadrigeminal plate [62][63]. The anatomical landmarks were used to guarantee a reproducible position of the brain slabs between different scanners (3T and 7T), over the two time points and between subjects. The brain slabs were positioned in consensus of two researchers (I.V.O with J.P.W or E.C.W) to achieve accurate positioning of the supra- and infratentorial brain slabs between the two time points and the measurements at 3T and 7T.

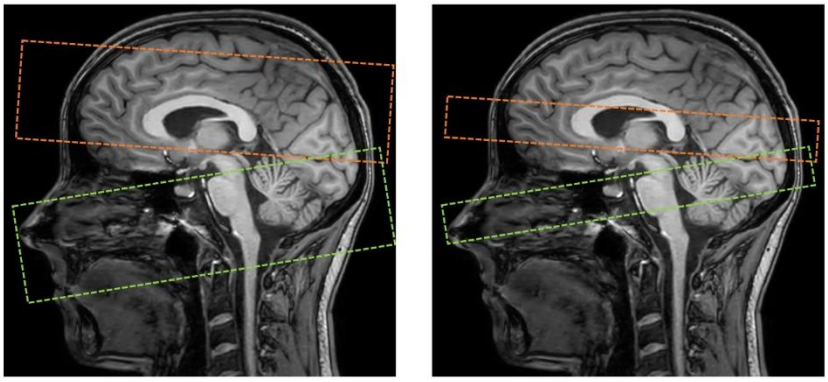

Figure 5.2: Positioning of brain slab for APTw image acquisition based on anatomical landmarks for 3T (A) and 7T (B). Supratentorial and infratentorial areas are marked with orange and green striped boxes respectively. At 3T the FOV in the z-direction is greater (10 slices of 6 mm) compared to 7T (12 slices of 2 mm)

5.1.3 Image processing

After normalization and B_0-correction of the z-spectra, APTw maps were determined by MTR_{asym} and/or Lorentzian fitting for each acquisition at 3T and 7T (section 3.2). The Lorentzian fitting includes five-pools (i.e. DS, MT, NOE, amines and amides (APT)). The prior knowledge (i.e. amplitude, FWHM and frequency offsets of the pools) to fit the full z-spectra of the brain are mentioned in Table A.1 (3T) and A.3 (7T) of Appendix A .

5.1.4 Atlas-based segmentation of region of interest

Regions of interest for assessment of repeatability and reproducibility were defined upon atlas-based segmentation of GM and WM. In atlas-based segmentation a transformation, determined by registration of the template to the target image, is applied to the labels assigned to structures in the atlas [64]. The MNI-152 nonlinear symmetric atlas (2009c, International Consortium for Brain Mapping (ICBM)) was used. This atlas contains anatomical images, T1w, T2w and PDw, based on intensity matching algorithms from MRI data of the brain of 152 young adults (aged 18.5-43.5 years) acquired on a 1.5T scanner (Gyroscan, Philips Healthcare, Best, The Netherlands) at the Montreal Neurological Institute (MNI) [65][66]. Corresponding probability maps of GM, WM and cerebral spinal fluid (CSF) were incorporated in the atlas [67]. Furthermore, appurtenant brain mask and labels of the brain lobes were available.

To obtain segments of GM and WM a threshold was applied to the probability maps (probability ≥ 0.5). GM and WM segments were multiplied with the atlas of the brain lobes to acquire segments of GM and WM for the brain lobes. This process is visualized in Appendix E. Quantification of APTw maps in the supratentorial area was enabled by GM and WM segments in frontal and parietal lobe, while for the infratentorial area, segments of GM and WM for the cerebellum and the segment of the pons (WM) were preserved. Besides seven segments of WM and six segments of GM, we have also evaluated smaller WM segments with a volume of approximately 1.2 mL based upon Response Assessment in Neuro Oncology (RANO) criteria [19]. The purpose of the small segments is to be more specific with regard to repeatability and reproducibility, since small segments do not tend to average inaccuracies compared to greater segments [68]. To generate small WM segments, volume reduction of the full WM segments was performed with morphological operations combining opening and closing followed by erosion. Elliptical structuring elements were adapted for different brain regions and type of morphological operation (Appendix D).

Atlas-based segmentation is performed by alignment of the T1w image of the MNI-152 atlas to T1w image of a subject, and the within subject registration of the T1w image to the unsaturated z-spectral images (S_0) using Elastix [69][70]. This process is visualized in Figure 5.3. The alignment of T1w image of the MNI-152 atlas with the T1w image of a subject started with rigid, followed by affine registration and was finalized by Bspline transformation. Subsequently, for all subjects the T1w image was aligned

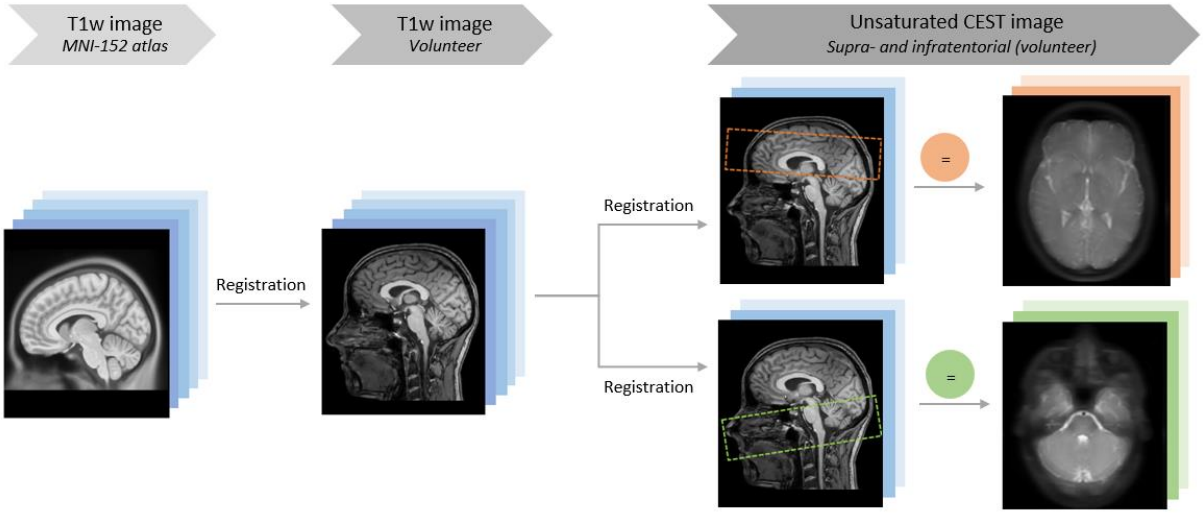

Figure 5.3: Registration steps performed to be able to perform atlas-based segmentation. Rigid, affine and bspline registration are applied to align the T1w image of the MNI-152 atlas with the T1w image of the subject. Solely rigid registration to register the T1w image of the subject with the CEST image of two specific brain areas.

to the unsaturated z-spectral images, individually for the supra- and infratentorial brain slabs. Details about the registration parameters are mentioned in Appendix F. Visual inspection of the registered images was performed in MeVisLab (version 3.4.2; MeVis Medical Solutions AG, Fraunhofer MEVIS).

5.1.5 Data analysis

Differences in APTw maps between the different acquisition sessions and within an acquisition session were visually evaluated for 3T and 7T. Quantitative analysis is performed based on the mean APTw values for several brain tissue segments i.e. GM, WM and small segment of WM. The brain tissue segments are visualized in Figure 5.4. The three clusters of the brain tissue segments of the supratentorial area contain twenty means, four segments for five subjects. The three clusters of the brain tissue segments of the cerebellum include ten means, two segments for five subjects and the two clusters of the segments of the pons enclose five means, one segment for five subjects. For each cluster of means, the mean ± standard deviation of APTw values were defined for the two acquisition sessions and the different acquisitions at 3T and 7T.

Based on the cluster of means belonging to the different brain regions and brain tissue segment the repeatability for each acquisition and magnetic field strength was further evaluated by calculating the

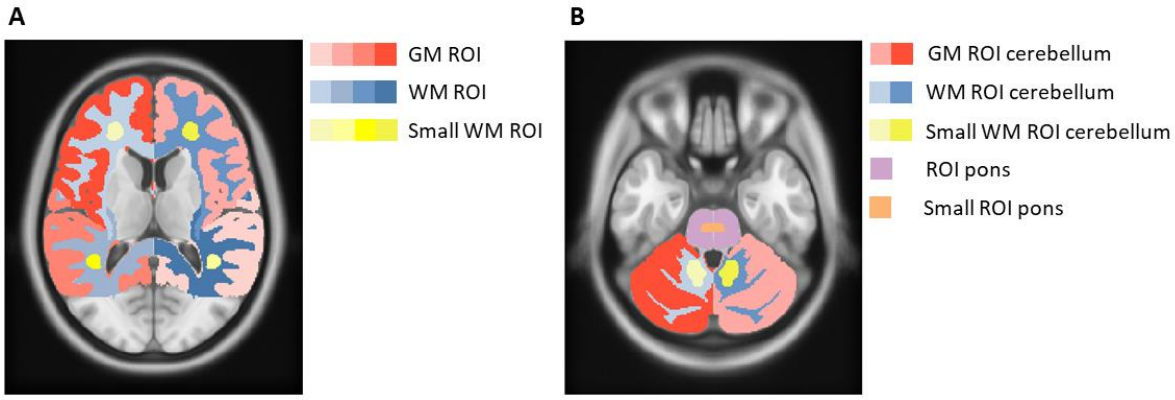

Figure 5.4: Tissue segments for supratentorial brain region (A) and infratentorial brain region (B). The colour bars for the different brain tissue types indicate that within one subject multiple segments were created to increase the number of samples. Supratentorial four tissue segments for each tissue type per subject (i.e frontal/ parietal and left/ right). Infratentorial two segments for the tissue types of the cerebellum (i.e. left/right) and one segment for the tissue types of the pons.

RMSD (*Eq. 5.1*) and wCV (*Eq. 5.2*). Both were calculated by pairs of repeated measures at 3T and 7T using the clusters of brain tissue segments for each acquisition and processing method. The reproducibility of APTw maps at 3T was evaluated by the RMSD and by the wCV to indicate difference between APTw maps generated from a full z-spectrum and APTw maps generated from 9p, 15p, 23p z-spectrum using the clusters of means of the brain tissue segments.

$$RMSD = \sqrt{\frac{\sum_{i=1}^{n}(x_{1,i} - x_{2,i})^2}{n}} \tag{5.1}$$

$$wCV = \frac{SD}{mean} \times 100\% \tag{5.2}$$

$$mean = \frac{\sum_{i=1}^{n}(x_{1,i} + x_{2,i})}{2n} \tag{5.2.a}$$

$$SD = \sqrt{\frac{\sum_{i=1}^{n}(x_{1,i} - x_{2,i})^2}{2n}} \tag{5.2.b}$$

With x_1 and x_2 the average APTw values of brain tissue segments for the different time points (repeatability) or acquisition methods (reproducibility) and n the number means in a cluster.

5.2 Results

5.2.1 Evaluation of registration

The registration indicate good alignment between the T1w image (MNI-152 atlas), the T1w image of subject and unsaturated CEST image for both the supratentorial and infratentorial brain region (Appendix G). Considering the performance of the registration adequate segmentation of the different brain tissue segments was achieved.

5.2.2 Supratentorial APTw imaging

APTw maps in the supratentorial area appear to be repeatable between the two acquisition sessions for the different acquisitions at both 3T (Figure 5.5) and 7T (Figure 5.6). Additionally, the inhomogeneous B_1-magnitude at 7T is repeatable within each subject (for example see Appendix B, Figure B.2). Comparing the different acquisition methods at 3T, the 15p z-spectrum acquisition is

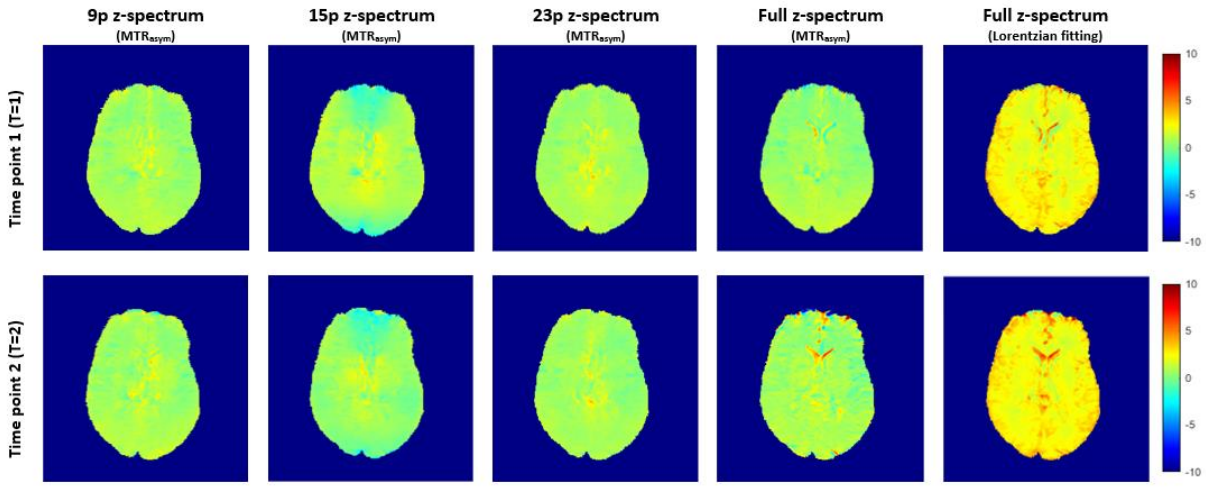

Figure 5.5: APTw maps of supratentorial brain region based on MTR_{asym} and/or Lorentzian fitting for acquisition with nine, fifteen, twenty-three z-spectral points and full z-spectrum acquisition at 3T. Upper row present the APTw maps measured at time point 1 and the lower row present the APTw maps measured at time point 2.

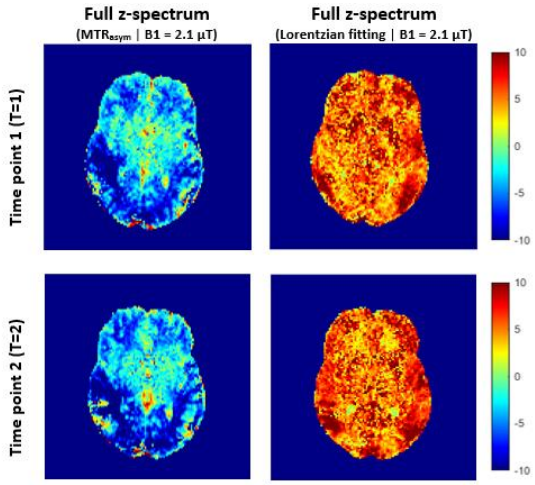

Figure 5.6: APTw maps of supratentorial brain region based on MTR_{asym} and Lorentzian fitting for full z-spectrum acquisition at 7T (B_1 = 2.1 µT). Upper row present the APTw maps measured at time point 1 and the lower row present the APTw maps measured at time point 2.

deviant, especially the frontal lobe shows lower APTw values compared to the other acquisitions. Moreover, higher APTw values are present when the full z-spectrum acquisition is processed by Lorentzian fitting compared to the APTw values obtained with MTR_{asym}. The greater amplitude of the Lorentzian function fitting APT, support the higher APTw values at 7T relative to the APTw values at 3T (Figure 5.7). The full z-spectrum at 7T shows evident asymmetry around 0 ppm compared to 3T ensuing the great difference between APTw maps constructed by MTR_{asym} and Lorentzian fitting at 7T.

The two acquisition session resulted in comparable APTw values for all three brain tissue segments considering the boxplots in Figure 5.8. However, this does not apply for the 15p z-spectrum acquisition that shows the greatest deviation between the two sessions. It is also noticeable, that the small WM segments have the greatest interquartile range in all acquisitions. These findings are supported by repeatability metrics mentioned in Table 5.1 for the different acquisition methods at 3T and 7T. Furthermore, the repeatability metrics indicate improvement of repeatability when the full z-spectrum acquisition at 3T was processed with Lorentzian fitting relative to processing with MTR_{asym}.

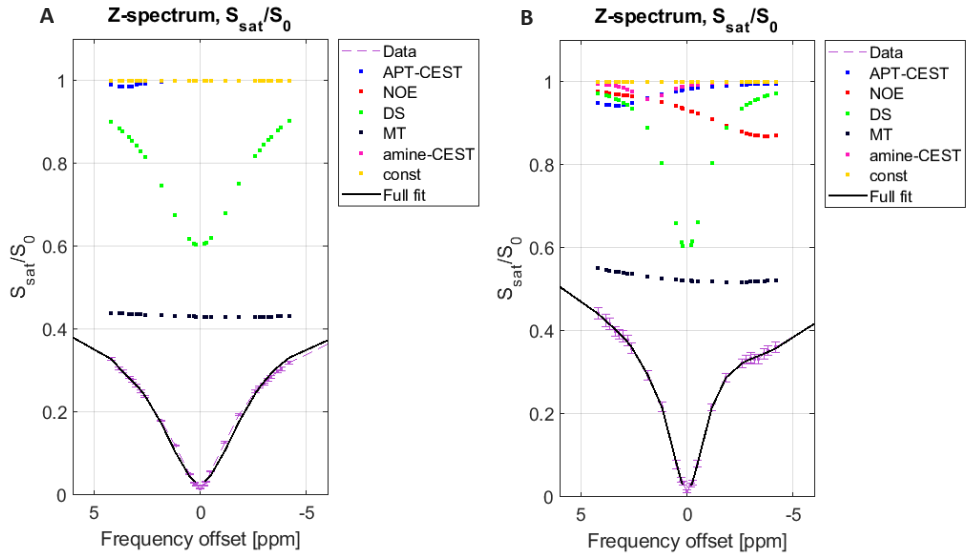

Figure 5.7: Full z-spectrum in supratentorial brain region including the Lorentzian functions resulting from the 5-pool fitting at 3T (A) and 7T (B)

The effect of further subdivision of the supratentorial brain segments (i.e. individual assessment of frontal and parietal lobe) on the repeatability are demonstrated in Appendix H.

No major difference is visible between the APTw values of the 9p and 23p z-spectrum acquisitions compared to the full z-spectrum acquisition, visualized by boxplots in figure 5.9. The reproducibility metrics in Table 5.2 argue best agreement between the 23p z-spectrum acquisition and full z-spectrum acquisition for the supratentorial brain regions.

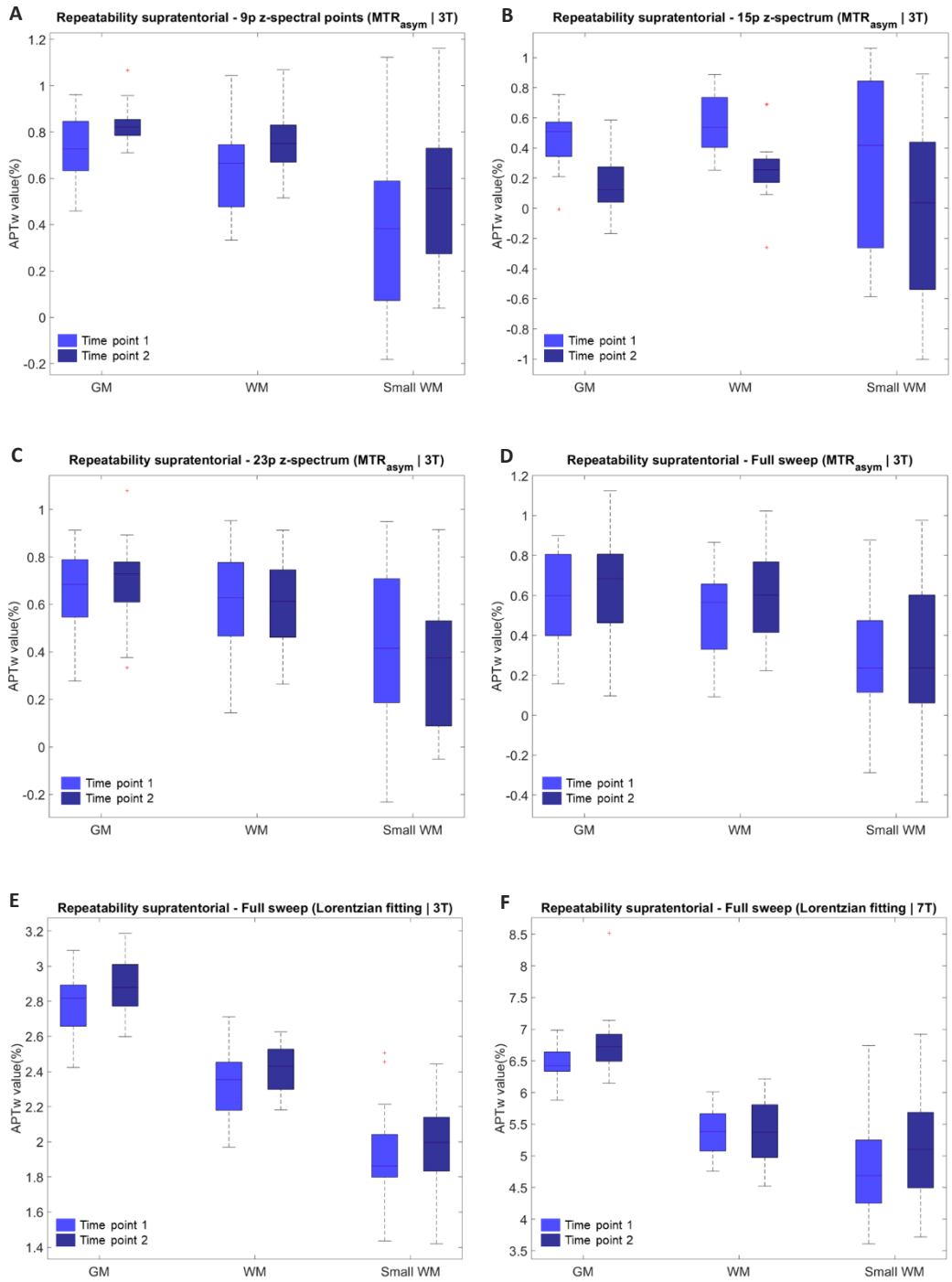

Figure 5.8: Boxplots of the supratentorial brain region for the different APTw acquisition and processing methods (A-E: 3T, F: 7T) to evaluate the repeatability of APTw values within each segment.

Table 5.1: APTw values (mean ± standard deviation) and repeatability metrics of the supratentorial brain tissue segments for the different APTw acquisition and processing methods

Magnetic field strength	Acquisition	Segment	APTw values (%) (mean ± STD)		RMSD	wCV (%)
			T=1	T-=2		
3T	9p z-spectrum*	GM	0.74±0.14	0.83±0.08	0.14	12.69
		WM	0.64±0.19	0.75±0.13	0.17	17.60
		Small WM	0.38±0.36	0.51±0.31	0.24	38.93
	15p z-spectrum*	GM	0.45±0.18	0.17±0.21	0.36	81.28
		WM	0.57±0.20	0.26±0.20	0.36	61.84
		Small WM	0.31±0.58	-0.01±0.55	0.43	203.21
	23p z-spectrum*	GM	0.66±0.18	0.69±0.17	0.16	16.76
		WM	0.61±0.33	0.62±0.28	0.19	22.35
		Small WM	0.42±0.23	0.35±0.18	0.27	50.17
	Full z-spectrum*	GM	0.60±0.23	0.65±0.27	0.30	34.02
		WM	0.53±0.22	0.61±0.23	0.31	38.59
		Small WM	0.29±0.29	0.31±0.41	0.33	77.17
	Full z-spectrum+	GM	2.79±0.17	2.89±0.16	0.27	6.64
		WM	2.33±0.20	2.41±0.13	0.24	7.23
		Small WM	1.91±0.28	2.00±0.24	0.25	9.02
7T	Full z-spectrum+	GM	6.47±0.28	6.78±0.50	0.69	7.35
		WM	5.39±0.39	5.40±0.49	0.70	9.14
		small WM	4.82±0.78	5.19±0.86	1.12	15.83

* z-spectrum processed with MTR_{asym}
\+ z-spectrum processed with Lorentzian fitting

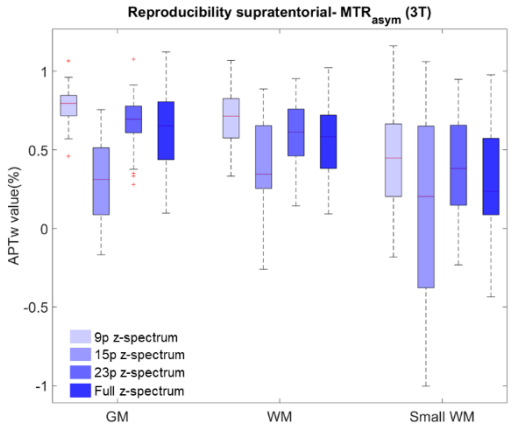

Figure 5.9: Boxplots of the supratentorial brain regions for the different APTw acquisition at 3T (processed with MTR_{asym}) for the evaluation of the reproducibility of APTw values within each segment.

Table 5.2: Reproducibility metrics of the supratentorial brain segments by comparing the shortened APTw acquisitions (i.e. 9p, 15p, 23p z-spectrum) with the full z-spectrum acquisition both processed with MTR_{asym} at 3T.

Comparison acquisition	Segment	RMSD	wCV (%)
9p z-spectrum vs full z-spectrum (3T)	GM	0.28	28.38
	WM	0.24	26.47
	Small WM	0.29	55.99
15p z-spectrum vs full z-spectrum (3T)	GM	0.48	71.75
	WM	0.37	53.09
	Small WM	0.46	144.74
23p z-spectrum vs full z-spectrum (3T)	GM	0.17	18.83
	WM	0.14	17.32
	Small WM	0.26	53.37

5.2.2 Infratentorial APTw imaging

Figure 5.10 and Figure 5.11 show agreement between APTw maps of the two acquisition session for different acquisitions at both 3T and 7T, respectively. Furthermore, the inhomogeneous B_1-magnitude at 7T has been issued as being repeatable within each subject (for example see Appendix B, Figure B.3). Considering the APTw maps processed with MTR_{asym}, the APTw values differ from positive to negative between the two sessions in the area around the pons. Similar to the supratentorial area, difference in APTw values are present between the processing methods (i.e. MTR_{asym} and Lorentzian fitting) for both 3T and 7T.

For all cerebellar tissue segments acquisition session had minor influence on the measured APTw values indicative of repeatability illustrated by boxplots in Figure 5.12. The boxplots belonging to the pons at 3T have a broad interquartile range compared to the cerebellar tissue segments, characteristic for heterogeneity of APTw values between subjects. As for the supratentorial brain region, the repeatability metrics of the infratentorial brain region (Table 5.3) show that the repeatability of APTw values improved when the full z-spectrum is processed by Lorentzian fitting. Especially, for the pons segments the Lorentzian fitting seriously surpass the MTR_{asym} at 3T in terms of precision.

The different acquisition methods at 3T has minor impact on the APTw values (MTR_{asym}) in the cerebellum, i.e. reproducible APTw values were obtained (Figure 5.13). Contrary, the 15p z-spectrum

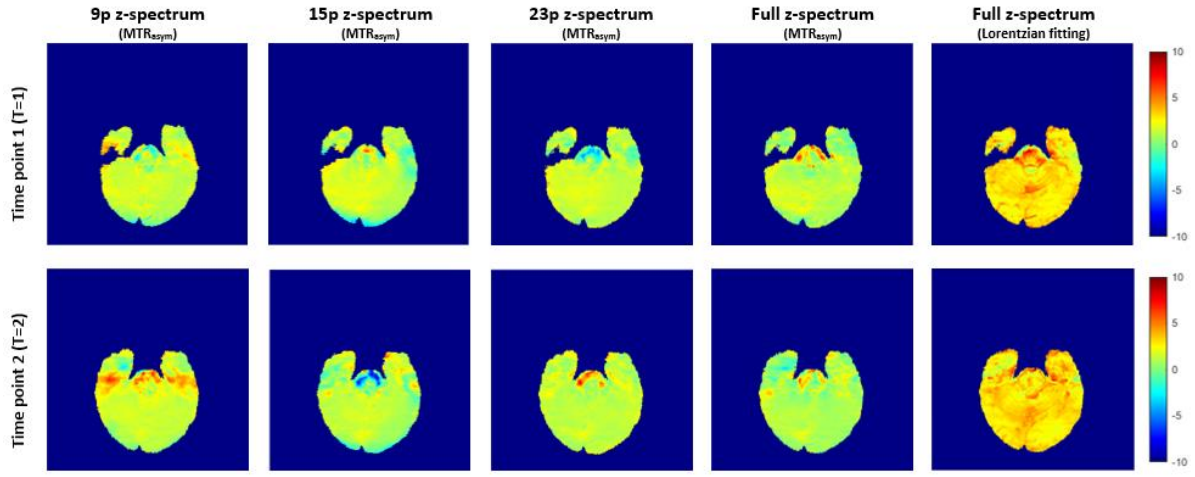

Figure 5.10: APTw maps of infratentorial brain region based on MTR_{asym} and/or Lorentzian fitting for acquisition with nine, fifteen, twenty-three z-spectral points and full z-spectrum acquisition at 3T. Upper row present the APTw maps measured at time point 1 and the lower row present the APTw maps measured at time point 2.

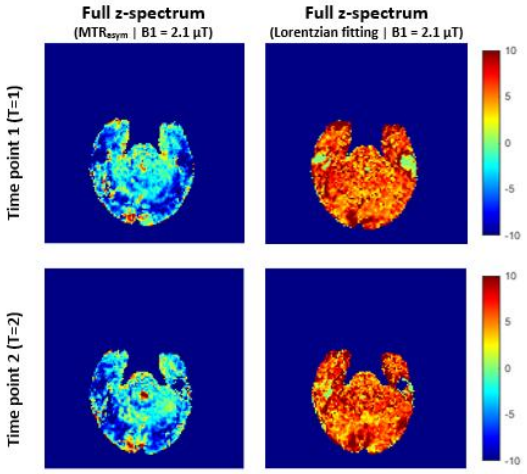

Figure 5.11: APTw maps of infratentorial brain region based on MTR_{asym} and Lorentzian fitting for full z-spectrum acquisition at 7T (B_1 = 2.1 µT). Upper row present the APTw maps measured at time point 1 and the lower row present the APTw maps measured at time point 2.

acquisition poorly reproduces the APTw values of the other acquisitions for the small segment of the pons. The RMSD and wCV mentioned in Table 5.4 address that the 9p z-spectrum acquisition reproduces the full z-spectrum acquisition best.

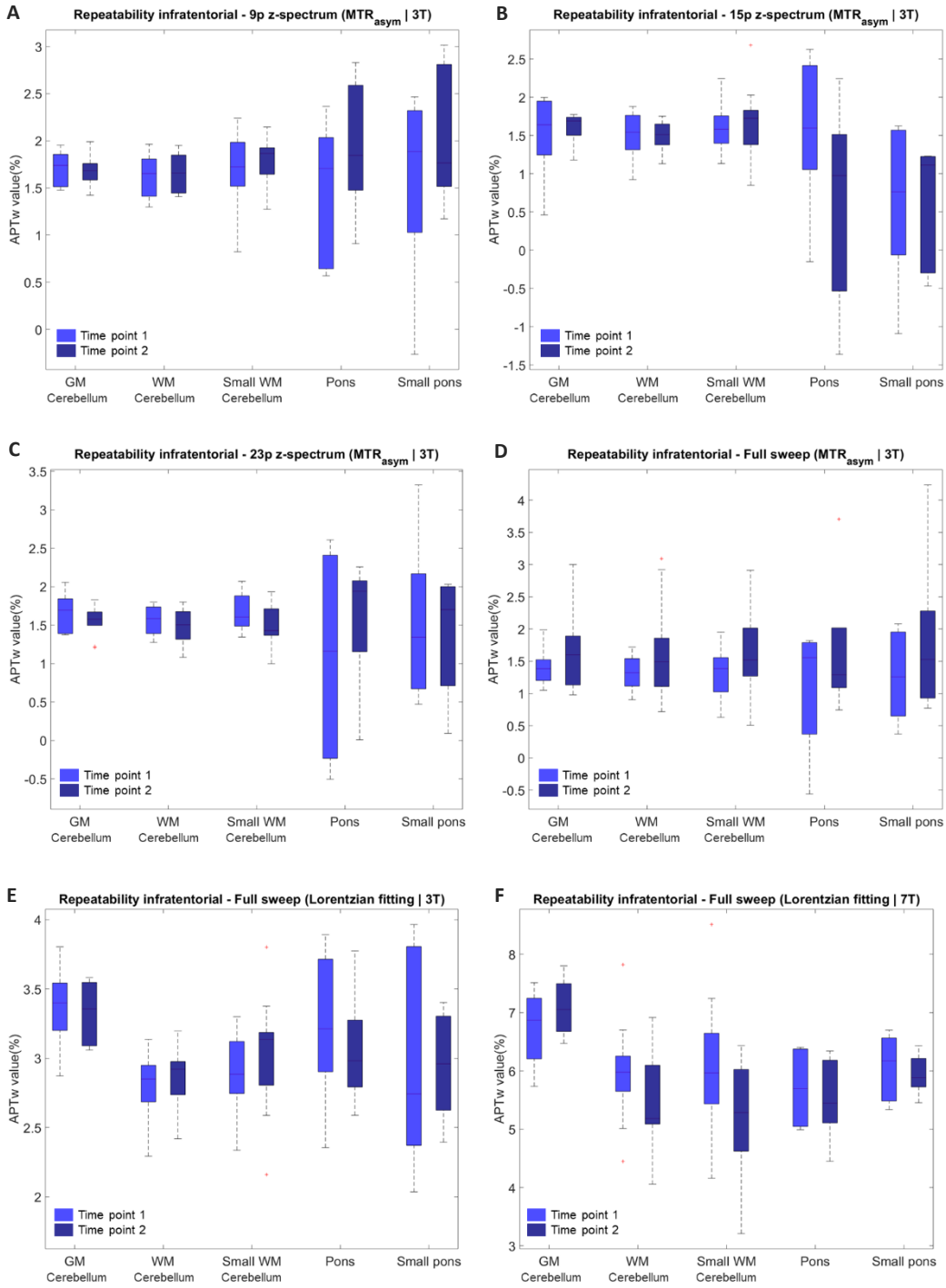

Figure 5.12: Boxplots of the infratentorial area for the different APTw acquisition and processing methods (A-E: 3T, F: 7T) to evaluate the repeatability of APTw values within each segment.

Table 5.3: APTw values (mean ± standard deviation) and repeatability metrics of the infratentorial brain segments for the different APTw acquisitions and processing methods.

Magnetic field strength	Acquisition	Segment	APTw values (%) (mean ± STD)		RMSD	wCV (%)
			T=1	T-=2		
3T	9p z-spectrum*	GM	1.71±0.18	1.70±0.18	0.27	11.37
		WM	1.62±0.24	1.66±0.20	0.26	11.24
		Small WM	1.68±0.42	1.80±0.24	0.52	21.24
		Pons	1.45±0.79	1.95±0.75	1.21	50.36
		Small pons	1.56±1.09	2.06±0.78	1.00	38.92
	15p z-spectrum*	GM	1.53±0.48	1.61±0.18	0.42	18.88
		WM	1.51±0.31	1.49±0.21	0.37	17.22
		Small WM	1.61±0.33	1.67±0.50	0.30	12.98
		Pons	1.57±1.08	0.57±1.40	2.03	133.57
		Small pons	0.63±1.11	0.57±0.85	1.50	177.24
	23p z-spectrum*	GM	1.67±0.24	1.54±0.20	0.33	14.72
		WM	1.56±0.19	1.48±0.24	0.30	14.13
		Small WM	1.66±0.24	1.47±0.29	0.43	19.256
		Pons	1.09±1.41	1.55±0.90	1.92	102.85
		Small pons	1.53±1.12	1.35±0.83	1.10	54.26
	Full z-spectrum*	GM	1.42±0.28	1.69±0.68	0.67	30.56
		WM	1.31±0.29	1.63±0.81	0.69	33.12
		Small WM	1.32±0.41	1.65±0.69	0.57	27.36
		Pons	1.05±1.01	1.68±1.16	1.67	86.62
		Small pons	1.27±0.73	1.83±1.39	1.77	80.53
	Full z-spectrum+	GM	3.35±0.28	3.33±0.20	0.41	8.76
		WM	2.79±0.25	2.85±0.25	0.42	10.43
		Small WM	2.87±0.32	3.05±0.45	0.58	13.79
		Pons	3.24±0.59	3.06±0.44	0.59	13.18
		Small pons	3.00±0.83	2.95±0.41	0.98	23.32
7T	Full z-spectrum+	GM	6.71±0.59	7.11±0.48	0.55	5.61
		WM	5.98±0.91	5.46±0.83	1.03	12.74
		Small WM	6.10±1.21	5.23±0.97	1.60	19.98
		Pons	5.70±0.68	5.54±0.75	0.61	7.68
		Small pons	6.05±0.60	5.95±0.37	0.38	4.42

* z-spectrum processed with MTR_{asym}
+ z-spectrum processed with Lorentzian fitting

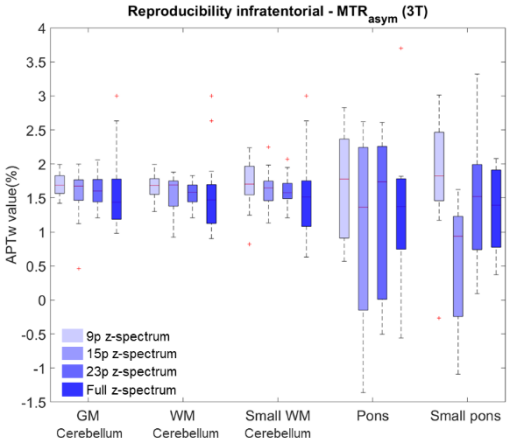

Figure 5.13 Boxplots of the infratentorial brain regions for the different APTw acquisition at 3T (processed with MTR_{asym}) for the evaluation of the reproducibility of APTw values within each segment.

Table 5.4: Reproducibility metrics of the infratentorial brain segments by comparing the shortened APTw acquisitions (i.e. 9, 15, 23 z-spectral points) with the full z-spectrum acquisition both processed with MTR_{asym} at 3T.

Comparison acquisition	Segment	RMSD	wCV (%)
9p z-spectrum vs full z-spectrum (3T)	GM	0.46	20.09
	WM	0.46	20.37
	Small WM	0.54	23.78
	Pons	0.87	40.19
	Small pons	1.13	47.52
15p z-spectrum vs full z-spectrum (3T)	GM	0.65	29.49
	WM	0.63	29.34
	Small WM	0.72	32.68
	Pons	1.11	64.59
	Small pons	1.51	99.57
23p z-spectrum vs full z-spectrum (3T)	GM	0.55	24.72
	WM	0.53	24.54
	Small WM	0.55	25.18
	Pons	1.05	55.00
	Small pons	1.14	53.99

6 Clinical study

6.1 Materials and methods

6.1.1 Study design

The aim of the MITCH (Metabolic Imaging of Tumours in Children) study is to determine the feasibility and robustness of APTw imaging and phosphorus magnetic resonance spectroscopy (^{31}P MRS) at 7T in the evaluation of treatment response in paediatric brain tumours. This study was approved by the medical ethical committee Utrecht. Written informed consent was obtained from each patient and/or patient's guardian. Each patient underwent an additional MRI scan at 7T three times (baseline and twice during follow-up) within three and six months after the baseline scan (Figure 6.1). The follow-up scans were planned in concordance with standard clinical MRI scans. In this thesis, only the APTw imaging of the study is considered; changes of the APTw values inside the tumour at the different time points were assessed.

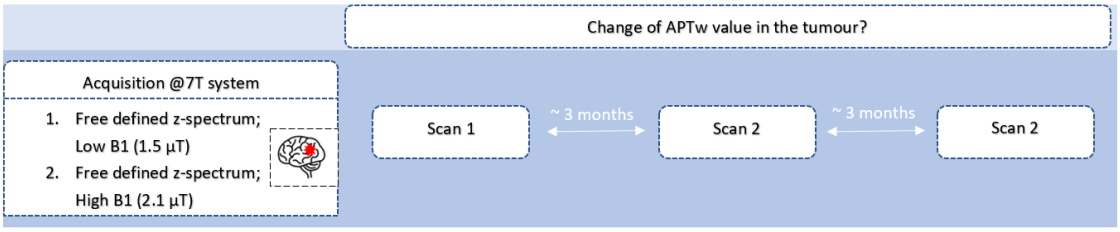

Figure 6.1: Scan protocol of MITCH study to determine feasibility and robustness of APTw imaging at 7T. Two acquisitions with different B1 were carried out.

6.1.2 Patient characteristics

Children between 6-18 years diagnosed with a possible LGG or DIPG and who are able to undergo MRI without anaesthesia are eligible to participate in this study. Patients are excluded from the study in case the tumour will be resected within one month, presence of claustrophobia or MRI incompatible foreign materials, such as metal implants, are present in the patient. Between January 2021 and September 2021 three patients participated in this study. Patient characteristics can be seen in Table 6.1.

6.1.3 APT-weighted image acquisition

The characteristics of the acquisition of the APTw images at 7T are described in section 3.2. Contrary to the in vivo study, the offsets are sampled from the negative to the positive offset. In each patient the slab is positioned encompassing the whole tumour. To be able to cover the whole tumour, slice thickness was doubled (FOV = 256 x 256 x 48 mm; resolution = 2.0 x 2.0 x 4.0 mm) in two cases (case 2 and 3). Orientation of the brain slab was discussed with an experienced neuro-radiologist (M.H.L.). Accordingly the brain slab was planned with consensus of two researchers (I.V.O with J.P.W or E.C.W). Screenshots of the planning were made, to ensure comparable orientation of the slab during follow-up. Figure 6.2 illustrate the orientation of the slabs for the three patients.

Table 6.1: Patient characteristics

	M/F	Age	Diagnosis	Mutation	Treatment
Case 1	M	11	Diffuse leptomeningeal glioneuronal tumour (DLGNT)	KIAA1549BRAF, TERT promotor	Vinblastine monotherapy (February 2021), Day101 (May 2021), stop treatment (June 2021)
Case 2	F	6	Optic pathway glioma (OPG)	-	Vinblastine monotherapy (March 2021)
Case 3	F	17	Subependymal giant cell astrocytoma (SEGA)	TSC-1/TSC-2	Everolimus (July 2021)

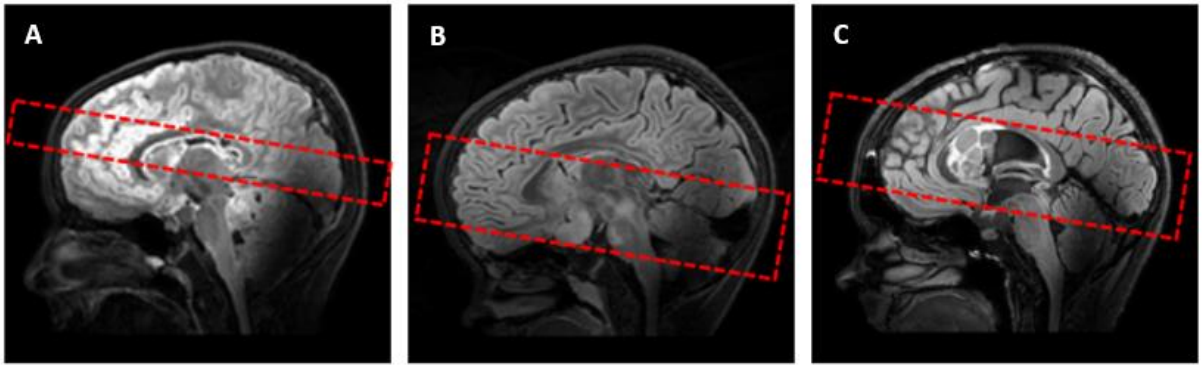

Figure 6.2: Positioning of brain slab for APTw image acquisition in three patients (case 1 (A), case 2 (B), case 3 (C)).

6.1.4 Image processing

Z-spectra were normalized and B_0-corrected first as described in section 3.2. Thereafter, the APTw maps were determined by Lorentzian fitting (section 3.2). The Lorentzian fitting incorporate five different pools (i.e. DS, MT, NOE, amines and amides (APT)). The parameters setting for the Lorentzian fitting, i.e. prior knowledge, are tabulated in Table A.3 of Appendix A.

6.1.5 Tumour segmentation

FLAIR images were aligned with the unsaturated z-spectral image using Elastix [69][70]. Rigid registration was performed, since the scans were performed in the same patient during the same session. Details of the registration parameters are mentioned in Appendix F.2.2. The performance of the registration was analysed by visual comparison of the registered FLAIR image and the unsaturated z-spectral image using MeVisLab (version 3.4.2; MeVis Medical Solutions AG, Fraunhofer MEVIS).

The registered FLAIR images were adopted for the manual segmentation of solid parts of the tumours. Slice-by-slice segmentation of the tumour was performed in the axial direction by using ITK-SNAP 3.2.0 [71]. All tumour segmentations were confirmed by a neuro-radiologist (M.H.L.).

6.1.6 Data analysis

Visual comparison of the APTw maps at different stage of treatment, baseline and follow-up twice, was performed for each patient individually. The comparison focused on the APTw values inside the tumour area(s) by means of boxplots and histograms. Quantitative analysis was based on changes in average APTw values of the tumour segment(s) between the different time points.

6.2 Results

6.2.1 Evaluation of registration

Figure 6.3 shows the registration result (i.e. registration of FLAIR image to the unsaturated CEST image) for each patient. The checkboard of the registered FLAIR with the unsaturated CEST image demonstrate good alignment in all patients.

6.2.2 APTw imaging of paediatric brain tumours

In two patients multiple segmentations of the tumour were made due to presence of diffuse and/or heterogenous tumours. Case 1 showed an extremely diffuse tumour in the whole brain from which two areas were segmented separately. The tumour of case 2 is an extensive tumour of the optic pathway with two areas, chiasm and pons, clinically marked as active tumour. Besides the whole tumour, also individual segments of these active tumour areas were created.

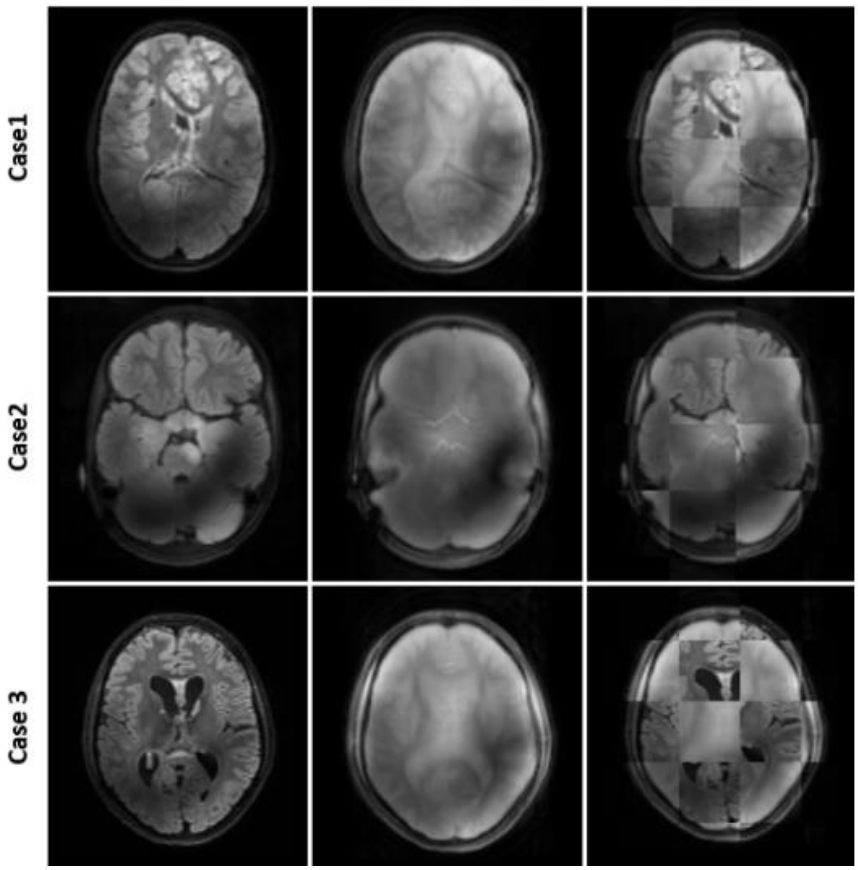

Figure 6.3: Final registration results for the three brain tumour cases. First column: registered FLAIR image. Second column: unsaturated CEST image. Third row: checkerboard view of registered FLAIR image and unsaturated CEST image.

Case 1. Figure 6.4 shows FLAIR images and APTw maps in a representative slice for the three scan sessions. Appendix I.1 incorporates an overview FLAIR images and APTw maps for all slices. At baseline, areas with high APTw values are spread diffusely over the brain. On the APTw maps of the first follow up, the high APTw values are mainly centred near the left atrium area of the brain. Relative to the baseline and first follow up, the second follow up shows predominant increase of APTw values around the frontal cortex. Focussing on the high APTw values in the frontal tumour segment (red segment), decrease in APTw values between baseline and first follow up occur in slice one over time. However, looking at the entire segment the decrease is hard to confirm, since the regions of lower and higher APTw values are organized differently, confirmed with nearly stable median of the boxplots and small percentage change of mean APTw values (Figure 6.5). Contrary, the boxplots corresponding to the tumour segment of the left atrium area (green segment) indicate increase in APTw values between baseline and first follow up, followed by an decrease between first and second follow up. Visually, higher APTw values are also seen in this area in the APTw map of the first follow up with respect to the baseline scan and second follow up. In Appendix I.1 the histograms are shown for the different scan sessions for each tumour mask individually.

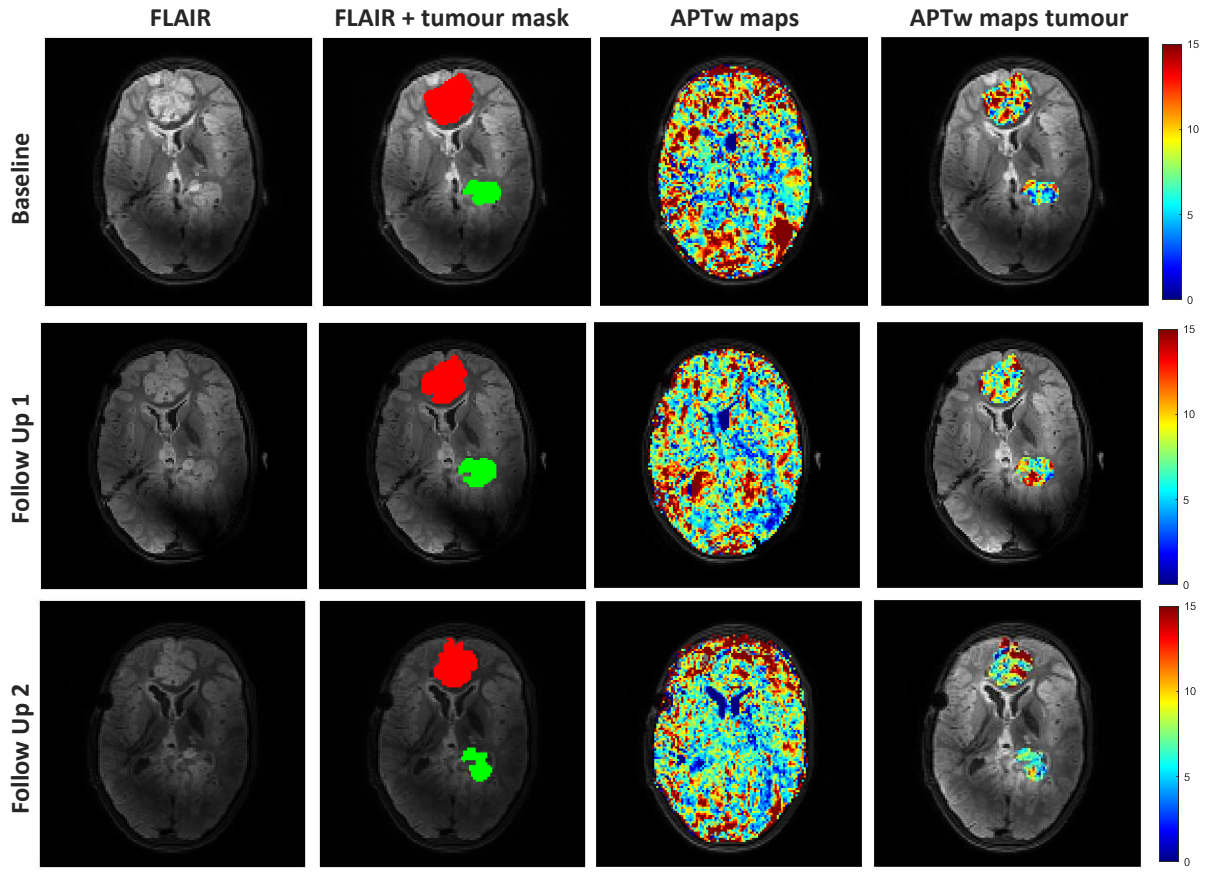

Figure 6.4: Longitudinal overview (baseline, first and second follow up) of FLAIR image and APTw map of case 1. Registered FLAIR image (first column), registered FLAIR including tumour masks (second column), APTw image (third column) and APTw image excise for the tumour mask only (fourth column)

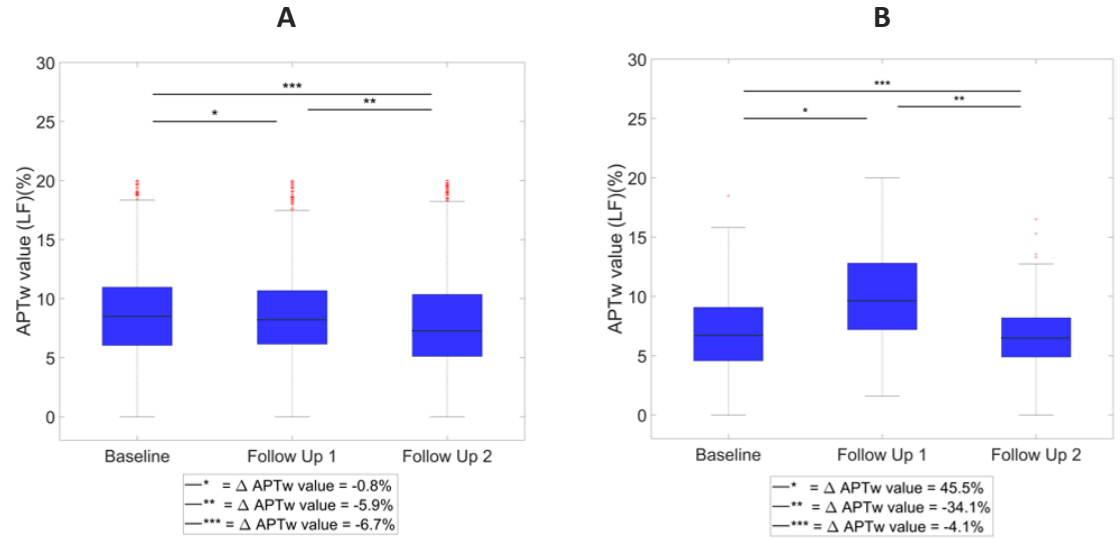

Figure 6.5: Boxplots corresponding to the baseline, first and second follow-up for two tumour areas showing difference in APTw values (A: frontal tumour mask ; B: tumour mask of atrium area)

Case 2. Figure 6.6 presents the registered FLAIR images and APTw maps in a slice incorporating three tumour mask for the three scan sessions. In Appendix I.2 an overview of registered FLAIR images and APTw maps including all slices is shown. Overall a slightly decrease in APTw values is visible in the tumour between baseline and first follow up. However, the APTw values of the tumour increase between first and second follow up. The boxplots and percentage change in APTw values affiliated with the complete tumour mask, present in Figure 6.7.A, substantiate this initial decrease and subsequent increase of the APTw values. The segment of the chiasmal part of the tumour (blue segment) shows an increase of APTw values based on visual comparison of APTw maps and boxplots of the three scan sessions supported by the percentage change of APTw values between the three scan sessions (Figure 6.7.B). The histograms associated with the different tumour segments for the three scan session are shown in Appendix I.2. Remarkably the course of the histograms is associated with the chiasmal part of the tumour segment over time, showing flattening of the histogram and shifting of the peak towards higher APTw values. The pons shows practically unchanged APTw values when comparing the three scan sessions. The change of APTw value in the chiasm is high relative to the change in APTw value considering the whole tumour, suggesting a heterogeneous pattern of metabolic activity inside the tumour.

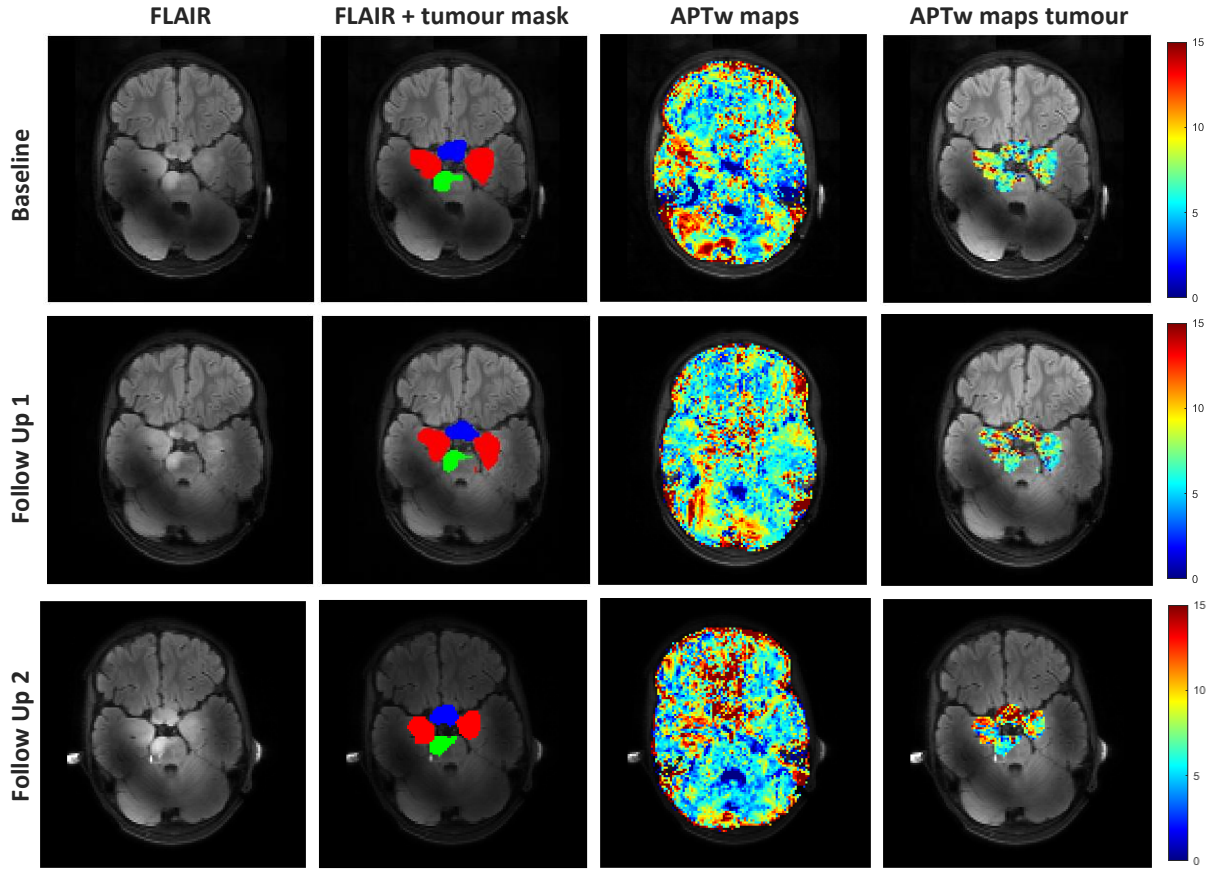

Figure 6.6: Longitudinal overview (baseline, first and second follow up) of FLAIR and APTw image of case 2 (slice 3). Registered FLAIR image (first column), registered FLAIR including tumour masks (second column), APTw image (third column) and APTw image excise for the tumour mask only (fourth column)

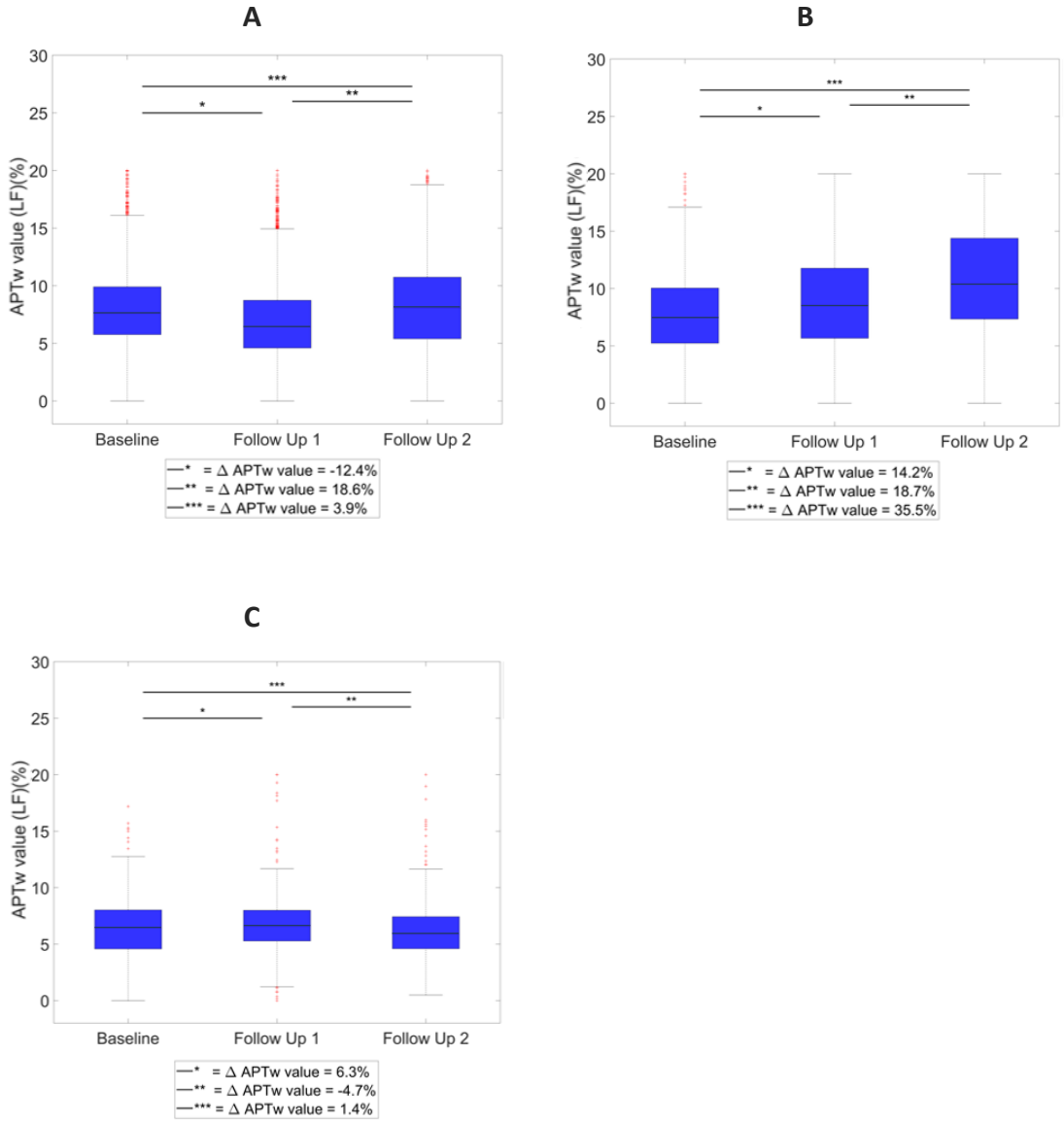

Figure 6.7: Boxplots corresponding to the baseline, first and second follow-up for three tumour areas showing difference in APTw values (A: complete tumour mask; B: chiasmal tumour mask; C: pons tumour mask).

Case 3. Registered FLAIR images and APTw maps of a representative slice for two time points are shown in Figure 6.8. An overview of registered FLAIR images and APTw maps including all slices is shown in Appendix I.3. The tumour, consisting of solid and cystic parts, is present in the septum pellucidum with continuation in the caudate nucleus. The APTw maps of the tumour show a decrease of APTw values comparing the baseline and first follow-up. The boxplots also show an shift towards lower APTw values, with a percentage decrease in average APTw value of 25% (Figure 6.9). Besides, shift towards lower APTw values is visible and the distribution of APTw values become less heterogenous, looking at the boxplots and histograms (Appendix I.3). Furthermore, the conventional MRI indicates a decrease in tumour volume of both the solid and cystic part of the tumour.

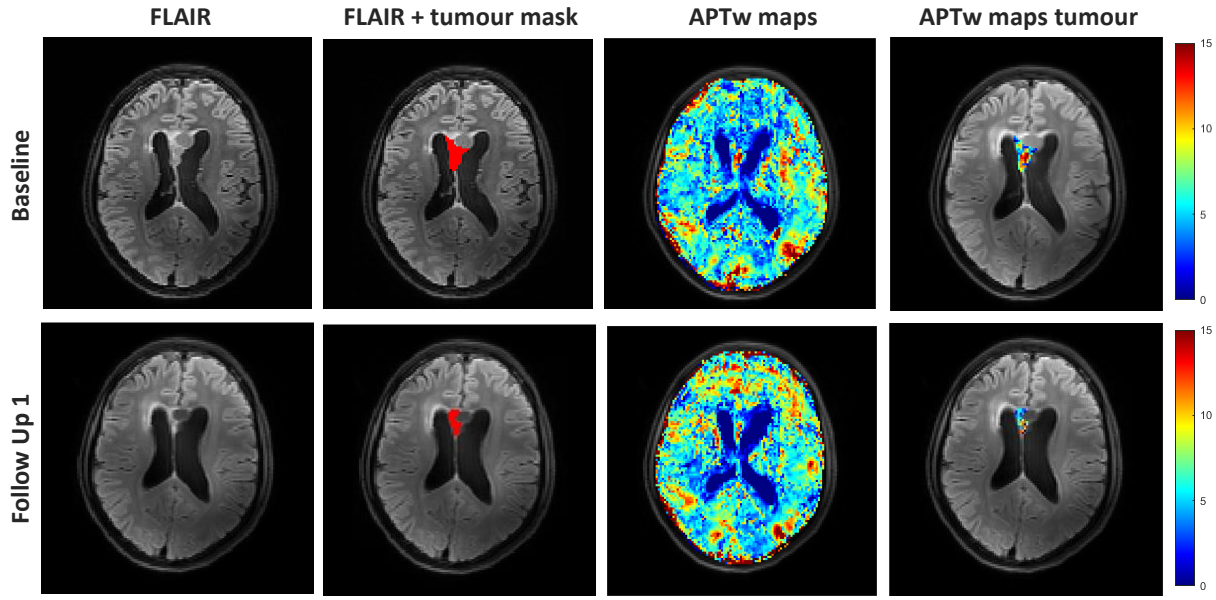

Figure 6.8 Longitudinal overview (baseline, first and second follow up) of FLAIR and APTw image of case 3. Registered FLAIR image (first column), registered FLAIR including tumour masks (second column), APTw image (third column) and APTw image excise for the tumour mask only (fourth column)

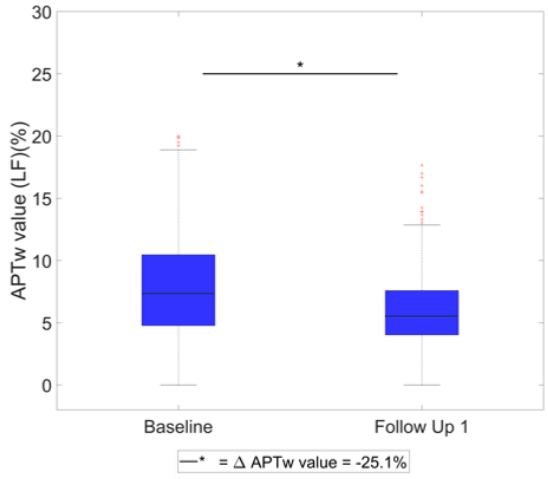

Figure 6.9: Boxplots corresponding to the baseline and first follow-up for the tumour areas.

7

Discussion & conclusion

To improve diagnosis and treatment evaluation of paediatric brain tumours, the applicability of APTw imaging in clinical decision making is investigated in terms of precision and feasibility. The phantom and in vivo study indicate best repeatable and robust APTw maps when full z-spectra were processed by Lorentzian fitting at both 3T and 7T. Furthermore, longitudinal APTw imaging of three paediatric brain tumours demonstrate heterogenous spatial distribution within one time point and a change of APTw values during treatment.

Translation of APTw imaging to clinical practice

Precision of APTw imaging has major consequences for application in clinical practice. APTw maps generated by Lorentzian fitting (i.e. full z-spectrum acquisition) at both 3T and 7T show the potential to discern changes in APTw values concerning precision, wCV ≤ 20%, which enables monitoring of treatment effects in brain tumours. This is supported by a significant difference of ~50% in APTw values that is reported between adult high-grade glioma showing treatment effects and showing tumour progression[28][29][72]. Furthermore, a longitudinal change of ~25% in APTw values is described in response to chemotherapy in orthotopic glioblastoma [30]. However, treatment-induced metabolic changes in low-grade glioma are expected to be inferior to changes in high-grade glioma. Nevertheless, it is supposed that metabolic changes in low-grade glioma can be detected as well considering the wCV.

Factors affecting the precision of APTw imaging

Discrepancy in APTw values between brain tissue types (i.e. GM and WM) and brain regions (i.e. supratentorial and cerebellum) could be explained by differences in their anatomical, histological and physiological features [73][74][75][76]. The amount of amides have no major effect on the repeatability: i.e. the wCV is comparable for different brain tissue types and brain regions. This is of relevance for clinical application, because high-grade glioma show increased cell proliferation and overexpression of proteins, and with that higher APTw values, relative to low-grade glioma [77]. Since the repeatability is independent of amide concentration, the precision assessed in this study can be translated towards both low-grade and high-grade glioma. However, the repeatability of the APTw values of the small WM segments is lower compared to full WM brain tissue segments, indicating the influence of the volume of segments on the repeatability of APTw values. Namely, smaller segments are prone to influence of outliers resulting in the diminished repeatability [68]. In general, this trend is observed regardless of the acquisition method (i.e. 9p, 15p, 23p or full z-spectrum) and processing method (MTR_{asym} or Lorentzian fitting). However, in the infratentorial brain region the 15p and full z-spectrum processed with MTR_{asym} showed improved repeatability for the small WM segments compared to the full WM segments. Since (residual) tumours can comprise a small volume the repeatability of small segments should be considered for the decision threshold in relation to the evaluation of tumour activity and treatment effects with APTw imaging.

In general, the repeatability in the supratentorial brain region is lower than previously reported when considering MTR_{asym} [36]. Presumably the repeatability is influenced by the segments of the frontal lobe (Appendix F) as a result of proximity to the ventricles and consequent effects of CSF flow or pulsation [73]. Nevertheless, the repeatability of mean APTw values in small WM segments of the parietal lobe is in agreement with a previous study [36]. The overall diminished repeatability is not present when the full z-spectrum acquisition is processed with Lorentzian fitting at either 3T or 7T. This implies that APTw maps constructed by means of Lorentzian fitting are more robust. The static phantom, i.e. without presence of contaminating effects that affect the MTR_{asym}, supports this finding, since no serious difference in repeatability between the full z-spectrum acquisition processed with MTR_{asym} and Lorentzian fitting is present. Repeatability of APTw imaging improved in all brain regions and tissue types when z-spectra were processed with Lorentzian fitting.

Compared to the supratentorial brain region and the cerebellum, the repeatability metrics belonging to the pons segments reveal that it is hard to obtain repeatable measures in this area at 3T using MTR_{asym}. Although the repeatability of the APTw maps acquired with the 9p z-spectrum acquisition in the pons is superior to previous findings [36], there is a low repeatability considering MTR_{asym} potentially explained by the vulnerability to B_0-inhomogeneity due to air-tissue and air-bone transitions [58][59]. The repeatability in the pons increases significantly with Lorentzian fitting which is robust for B_0-inhomogeneities. Additionally, the repeatability of APTw values in the pons obtained with the full z-spectrum acquisition at 7T outperformed the same acquisition at 3T. This could be explained the difference in slice thickness (2 mm vs 6 mm), resulting in a larger partial volume effects at 3T. Since the pons has an irregular shape and gradual course in cranio-caudal direction, partial volume effects are not inconvenient in this brain region.

Feasibility of APTw imaging in paediatric brain tumours at 7T

Preliminary results of APTw imaging at 7T involving three patients provided initial insights regarding feasibility of APTw imaging in paediatric brain tumours. In three out of six brain tumour segments (unequally distributed over the patients) longitudinal changes in APTw values were superior to the intrasubject variability, signifying a change in tumour metabolism. Most striking result is obtained in one of the patients who shows a heterogenous distribution of APTw values and 35% increase of mean APTw value together with an indolent course, e.g. no change of volume, considering the anatomical scans. The longitudinal change in mean APTw value might be indicative for increased tumour activity and consequently tumour aggressiveness which will aid in clinical decision making. Contrary, the 25% change in mean APTw value in case three have minor consequences for clinical decision making, since the anatomical scans already demonstrate reduction in tumour volume. APTw imaging of more paediatric brain tumours is needed to define guidelines for application in clinical decision making.

Limitations of the study

The observed repeatability of APTw imaging might have been negatively influenced by lack of image registration between the z-spectral images. Movement artefacts will be present in young children [78], resulting in inappropriate APTw maps and consequently registration of z-spectral images should be considered in the paediatric population. Furthermore, the fitting parameters for the Lorentzian fitting are not validated for both 3T and 7T in the phantom and in vivo. Accurate validation is hard, since phantom measurements are not able to mimic the heterogenous in-vivo environment causing confounding effects as MT and NOE [79]. We used starting values from literature and tune by manual grid searching until a correct fit was obtained by evaluating the goodness of the fitting. Accordingly, the resulted APTw maps where in consensus with literature [24][80]. Additionally, the APTw maps at 7T were created without B_1-correction despite the variety of B_1-magnitude across the field of view and significant influence of B_1-magnitude on the validity of APTw values [39][51][81]. Contrary, the inhomogeneous B_1-magnitude is considered not to influence the repeatability as our B_1-maps have showed to be consistent within each subject over time. However, B_1-correction should be considered when comparing APTw values between patients, between magnetic field strengths (i.e. 3T and 7T), between different hardware configuration, or in long-term follow-up.

Recommendations and future perspectives

From clinical perspective, evaluation of tumour activity based on APTw imaging at 3T is preferred. Considering scan duration and precision at 3T, the 9p z-spectrum (scan time= 03:45 min) shows a great potential for wide clinical application as the repeatability outperforms the repeatability of the 23p and full z-spectrum acquisitions processed with MTR_{asym}. However, the possibilities of processing the 9p z-spectrum by Lorentzian fitting must be investigated as this might increase the clinical applicability of APTw imaging at 3T. For brain tumours with a small volume or fast geometrical change, APTw imaging at 7T should be considered because of its higher spatial resolution. Further research should investigate

whether APTw imaging at 3T equals APTw imaging at 7T in the evaluation of tumour metabolism in paediatric brain tumours in specific tumour types, locations or tumour volumes.

Furthermore, more children should be included in the MITCH study to provide a more thorough assessment of the applicability of APTw imaging in paediatric neuro-oncology. In further research it is important to see whether findings of APTw imaging are supported by other sequences, e.g. ^{31}P MRS [82][83], in the detection of metabolic changes inside tumours. Additionally, the APTw maps should be correlated to clinical outcome parameters to define specific guidelines or cut off values for clinical application regarding diagnosis and treatment effects of paediatric brain tumours. Clinical outcome parameters include overall survival, clinical symptoms, radiological examination (i.e. tumour volume and contrast enhancement) and ophthalmological assessment when the tumour affects the optic pathway.

We encourage clinicians to use APTw imaging due to the present potential in evaluation of treatment effects by means of tumour metabolism considering the precision at either 3T or 7T especially when using Lorentzian fitting. APTw imaging is of special interest for brain tumours with an indolent course, such as optic pathway glioma, remaining stable on conventional MRI during treatment or in troublesome situations when doubt if true progression or pseudoprogression is present.

Conclusion

In conclusion, APTw maps belonging to the full z-spectrum acquisition and processed with Lorentzian fitting at both 3T and 7T, facilitate the use of APTw imaging as an imaging biomarker in monitoring brain tumour activity and subsequently brain tumour aggressiveness. The preliminary results of APTw imaging in paediatric brain tumours combined with the precision results seem to indicate the feasibility of APTw imaging at 7T in the detection of changes in paediatric brain tumour metabolism.

Bibliography

[1] Skion - Hersentumoren n.d. https://www.skion.nl/voor-patienten-en-ouders/ziektebeelden/542/ziektebeelden/545/hersentumoren/ (accessed February 8, 2021).

[2] Udaka YT, Packer RJ. Pediatric Brain Tumors. Neurologic Clinics 2018;36:533–56. https://doi.org/10.1016/j.ncl.2018.04.009.

[3] Duke ES, Packer RJ. Update on Pediatric Brain Tumors: the Molecular Era and Neuro-immunologic Beginnings. Current Neurology and Neuroscience Reports 2020;20:1–8. https://doi.org/10.1007/s11910-020-01050-6.

[4] Storm H, Engholm G, Mägi M, Aareleid T, Bossard N, Uhry Z, et al. Geographical variability in survival of European children with central nervous system tumours. European Journal of Cancer 2017;82:137–48. https://doi.org/10.1016/j.ejca.2017.05.028.

[5] Jagt- van Kampen CT, van de Wetering MD, Schouten–van Meeteren AYN. The timing, duration, and management of symptoms of children with an incurable brain tumor: a retrospective study of the palliative phase. Neuro-Oncology Practice 2015;2:70–7. https://doi.org/10.1093/nop/npu038.

[6] Keene DL, Johnston DL. Epidemiology of Central Nervous System Tumors. Pediatric Neuro-oncology, Springer New York; 2015, p. 9–12. https://doi.org/10.1007/978-1-4939-1541-5_3.

[7] Wells EM, Packer RJ. Pediatric brain tumors. CONTINUUM Lifelong Learning in Neurology 2015;21:373–96. https://doi.org/10.1212/01.CON.0000464176.96311.d1.

[8] de Blank P, Bandopadhayay P, Haas-Kogan D, Fouladi M, Fangusaro J. Management of pediatric low-grade glioma. Current Opinion in Pediatrics 2019;31:21–7. https://doi.org/10.1097/MOP.0000000000000717.

[9] Byer L, Kline C, Mueller S. Clinical trials in pediatric neuro-oncology: what is missing and how we can improve. CNS Oncology 2016;5:233–9. https://doi.org/10.2217/cns-2016-0016.

[10] Rashed WM, Maher E, Adel M, Saber O, Zaghloul MS. Pediatric diffuse intrinsic pontine glioma: where do we stand? Cancer and Metastasis Reviews 2019;38:759–70. https://doi.org/10.1007/s10555-019-09824-2.

[11] Fischer C, Petriccione M, Donzelli M, Pottenger E. Improving Care in Pediatric Neuro-oncology Patients: An Overview of the Unique Needs of Children with Brain Tumors. Journal of Child Neurology 2016;31:488–505. https://doi.org/10.1177/0883073815597756.

[12] Richterová R, Kolarovszki B. Primary Brain Tumors in Childhood. Brain Tumors - An Update, InTech; 2018. https://doi.org/10.5772/intechopen.74510.

[13] Crawford J. Childhood brain tumors. Pediatrics in Review 2013;34:63–78. https://doi.org/10.1542/pir.34-2-63.

[14] Karajannis M, Allen JC, Newcomb EW. Treatment of pediatric brain tumors. Journal of Cellular Physiology 2008;217:584–9. https://doi.org/10.1002/jcp.21544.

[15] Blionas A, Giakoumettis D, Klonou A, Neromyliotis E, Karydakis P, Themistocleous MS. Paediatric gliomas: diagnosis, molecular biology and management. Annals of Translational Medicine 2018;6:251–251. https://doi.org/10.21037/atm.2018.05.11.

[16] Pollack IF, Agnihotri S, Broniscer A. Childhood brain tumors: Current management, biological insights, and future directions. Journal of Neurosurgery: Pediatrics 2019;23:261–73. https://doi.org/10.3171/2018.10.PEDS18377.

[17] Chukwueke UN, Wen PY. Use of the Response Assessment in Neuro-Oncology (RANO) criteria in clinical trials and clinical practice. CNS Oncology 2019;8:CNS28. https://doi.org/10.2217/cns-2018-0007.

[18] Wen PY, Chang SM, van den Bent MJ, Vogelbaum MA, Macdonald DR, Lee EQ. Response assessment in neuro-oncology clinical trials. Journal of Clinical Oncology 2017;35:2439–49. https://doi.org/10.1200/JCO.2017.72.7511.

[19] Leao D, Craig P, Godoy L, Leite C, Policeni B. Response Assessment in Neuro-Oncology Criteria for Gliomas: Practical Approach Using Conventional and Advanced Techniques. AJNR American Journal of Neuroradiology 2020;41:10–20. https://doi.org/10.3174/AJNR.A6358.

[20] MacDonald SM. Central Nervous System Tumors in Children. Clinical Radiation Oncology, Elsevier Inc.; 2015, p. 1389-1402.e3. https://doi.org/10.1016/B978-0-323-24098-7.00067-8.

[21] Su C, Liu C, Zhao L, Jiang J, Zhang J, Li S, et al. Amide proton transfer imaging allows detection of glioma grades and tumor proliferation: Comparison with Ki-67 expression and proton MR spectroscopy imaging. American Journal of Neuroradiology 2017;38:1702–9. https://doi.org/10.3174/ajnr.A5301.
[22] Togao O, Yoshiura T, Keupp J, Hiwatashi A, Yamashita K, Kikuchi K, et al. Amide proton transfer imaging of adult diffuse gliomas: Correlation with histopathological grades. Neuro-Oncology 2014;16:441–8. https://doi.org/10.1093/neuonc/not158.
[23] Zhou J, Zhu H, Lim M, Blair L, Quinones-Hinojosa A, Messina SA, et al. Three-dimensional amide proton transfer MR imaging of gliomas: Initial experience and comparison with gadolinium enhancement. Journal of Magnetic Resonance Imaging 2013;38:1119–28. https://doi.org/10.1002/jmri.24067.
[24] Zhang J, Zhu W, Tain R, Zhou XJ, Cai K. Improved Differentiation of Low-Grade and High-Grade Gliomas and Detection of Tumor Proliferation Using APT Contrast Fitted from Z-Spectrum. Molecular Imaging and Biology 2018;20:623–31. https://doi.org/10.1007/s11307-017-1154-y.
[25] Togao O, Hiwatashi A, Yamashita K, Kikuchi K, Keupp J, Yoshimoto K, et al. Grading diffuse gliomas without intense contrast enhancement by amide proton transfer MR imaging: comparisons with diffusion- and perfusion-weighted imaging. European Radiology 2017;27:578–88. https://doi.org/10.1007/s00330-016-4328-0.
[26] Ma B, Blakeley JO, Hong X, Zhang H, Jiang S, Blair L, et al. Applying amide proton transfer-weighted MRI to distinguish pseudoprogression from true progression in malignant gliomas. Journal of Magnetic Resonance Imaging 2016;44:456–62. https://doi.org/10.1002/jmri.25159.
[27] Zhou J, Tryggestad E, Wen Z, Lal B, Zhou T, Grossman R, et al. Differentiation between glioma and radiation necrosis using molecular magnetic resonance imaging of endogenous proteins and peptides. Nature Medicine 2011;17:130–4. https://doi.org/10.1038/nm.2268.
[28] Jiang S, Eberhart C, Lim M, Heo H, Zhang Y, Blair L, et al. Identifying Recurrent Malignant Glioma after Treatment Using Amide Proton Transfer-Weighted MR Imaging: A Validation Study with Image-Guided Stereotactic Biopsy. Clinical Cancer Research : An Official Journal of the American Association for Cancer Research 2019;25:552–61. https://doi.org/10.1158/1078-0432.CCR-18-1233.
[29] Park JE, Kim HS, Park KJ, Kim SJ, Kim JH, Smith SA. Pre-and posttreatment glioma: Comparison of amide proton transfer imaging with MR spectroscopy for biomarkers of tumor proliferation. Radiology 2016;278:514–23. https://doi.org/10.1148/RADIOL.2015142979/ASSET/IMAGES/LARGE/RADIOL.2015142979.FIG5B.JPEG.
[30] Sagiyama K, Mashimo T, Togao O, Vemireddy V, Hatanpaa KJ, Maher EA, et al. In vivo chemical exchange saturation transfer imaging allows early detection of a therapeutic response in glioblastoma. Proceedings of the National Academy of Sciences of the United States of America 2014;111:4542–7. https://doi.org/10.1073/pnas.1323855111.
[31] Meissner JE, Korzowski A, Regnery S, Goerke S, Breitling J, Floca RO, et al. Early response assessment of glioma patients to definitive chemoradiotherapy using chemical exchange saturation transfer imaging at 7 T. Journal of Magnetic Resonance Imaging 2019;50:1268–77. https://doi.org/10.1002/jmri.26702.
[32] Regnery S, Adeberg S, Dreher C, Oberhollenzer J, Meissner JE, Goerke S, et al. Chemical exchange saturation transfer MRI serves as predictor of early progression in glioblastoma patients. Oncotarget 2018;9:28772–83. https://doi.org/10.18632/oncotarget.25594.
[33] Merchant TE, Pollack IF, Loeffler JS. Brain Tumors Across the Age Spectrum: Biology, Therapy, and Late Effects. Seminars in Radiation Oncology 2010;20:58–66. https://doi.org/10.1016/j.semradonc.2009.09.005.
[34] D'Arco F, Culleton S, de Cocker LJL, Mankad K, Davila J, Tamrazi B. Current concepts in radiologic assessment of pediatric brain tumors during treatment, part 1. Pediatric Radiology 2018;48:1–11. https://doi.org/10.1007/s00247-018-4194-9.
[35] Sullivan DC, Obuchowski NA, Kessler LG, Raunig DL, Gatsonis C, Huang EP, et al. Metrology standards for quantitative imaging biomarkers. Radiology 2015;277:813–25. https://doi.org/10.1148/radiol.2015142202.
[36] Lee J bin, Park JE, Jung SC, Jo Y, Kim D, Kim HS, et al. Repeatability of amide proton transfer–weighted signals in the brain according to clinical condition and anatomical location. European Radiology 2020;30:346–56. https://doi.org/10.1007/s00330-019-06285-7.

[37] Togao O, Hiwatashi A, Keupp J, Yamashita K, Kikuchi K, Yoshiura T, et al. Scan-rescan reproducibility of parallel transmission based amide proton transfer imaging of brain tumors. Journal of Magnetic Resonance Imaging : JMRI 2015;42:1346–53. https://doi.org/10.1002/JMRI.24895.
[38] Morrison MA, Lupo JM. 7-T Magnetic Resonance Imaging in the Management of Brain Tumors. Magnetic Resonance Imaging Clinics of North America 2021;29:83–102. https://doi.org/10.1016/j.mric.2020.09.007.
[39] Windschuh J, Zaiss M, Meissner JE, Paech D, Radbruch A, Ladd ME, et al. Correction of B1-inhomogeneities for relaxation-compensated CEST imaging at 7T. NMR in Biomedicine 2015;28:529–37. https://doi.org/10.1002/nbm.3283.
[40] Wu B, Warnock G, Zaiss M, Lin C, Chen M, Zhou Z, et al. An overview of CEST MRI for non-MR physicists. EJNMMI Physics 2016;3. https://doi.org/10.1186/s40658-016-0155-2.
[41] van Zijl PCM, Yadav NN. Chemical exchange saturation transfer (CEST): What is in a name and what isn't? Magnetic Resonance in Medicine 2011;65:927–48. https://doi.org/10.1002/mrm.22761.
[42] Vinogradov E, Sherry AD, Lenkinski RE. CEST: from basic principles to applications, challenges and opportunities. Journal of Magnetic Resonance (San Diego, Calif : 1997) 2013;229:155. https://doi.org/10.1016/J.JMR.2012.11.024.
[43] Enhancing brain tumor MRI with APT weighted imaging | FieldStrength | Philips n.d. https://www.philips.no/healthcare/education-resources/publications/fieldstrength/enhancing-brain-tumor-mri-with-apt (accessed February 16, 2021).
[44] Vinogradov E, Sherry AD, Lenkinski RE. CEST: From basic principles to applications, challenges and opportunities. Journal of Magnetic Resonance 2013;229:155–72. https://doi.org/10.1016/j.jmr.2012.11.024.
[45] Zaiß M, Schmitt B, Bachert P. Quantitative separation of CEST effect from magnetization transfer and spillover effects by Lorentzian-line-fit analysis of z-spectra. Journal of Magnetic Resonance 2011;211:149–55. https://doi.org/10.1016/j.jmr.2011.05.001.
[46] Krikken E, Khlebnikov V, Zaiss M, Jibodh RA, van Diest PJ, Luijten PR, et al. Amide chemical exchange saturation transfer at 7T: A possible biomarker for detecting early response to neoadjuvant chemotherapy in breast cancer patients. Breast Cancer Research 2018;20. https://doi.org/10.1186/s13058-018-0982-2.
[47] Atta-ur-Rahman, Choudhary MI. Nuclear Overhauser Effect. Solving Problems with NMR Spectroscopy, Elsevier; 1996, p. 187–211. https://doi.org/10.1016/b978-012066320-0/50006-9.
[48] van de Ven K, Keupp J. Instruction for use APT Extensions. Best: n.d.
[49] Zaiss M, Schmitt B, Bachert P. Quantitative separation of CEST effect from magnetization transfer and spillover effects by Lorentzian-line-fit analysis of z-spectra. Journal of Magnetic Resonance (San Diego, Calif : 1997) 2011;211:149–55. https://doi.org/10.1016/J.JMR.2011.05.001.
[50] Hollas JM. Modern spectroscopy. 3rd ed. Chichester: John Wiley & Sons, Ltd; 1996.
[51] Schuenke P, Windschuh J, Roeloffs V, Ladd M, Bachert P, Zaiss M. Simultaneous mapping of water shift and B 1 (WASABI)-Application to field-Inhomogeneity correction of CEST MRI data. Magnetic Resonance in Medicine 2017;77:571–80. https://doi.org/10.1002/MRM.26133.
[52] Amines and Amides | Chemistry for Majors n.d. https://courses.lumenlearning.com/chemistryformajors/chapter/amines-and-amides/ (accessed June 11, 2021).
[53] Orlowski P, Chappell M, Park CS, Grau V, Payne S. Modelling of pH dynamics in brain cells after stroke. Interface Focus 2011;1:408–16. https://doi.org/10.1098/RSFS.2010.0025.
[54] Jin T, Autio J, Obata T, Kim SG. Spin-locking versus chemical exchange saturation transfer MRI for investigating chemical exchange process between water and labile metabolite protons. Magnetic Resonance in Medicine 2011;65:1448–60. https://doi.org/10.1002/mrm.22721.
[55] Jung Y, Park J, Kim S-G, Park S-H. Diffusion-weighted Chemica Exchange Saturation Transfer Imaging at 7T Human MRI. ISMRM, Daejeon: 2021.
[56] Yao J, Wang C, Raymond C, Bergstrom B, Chen X, Das K, et al. A physical phantom for amine chemical exchange saturation transfer (CEST) MRI. Magnetic Resonance Materials in Physics, Biology and Medicine 2021. https://doi.org/10.1007/s10334-020-00902-z.

[57] Jones CK, Schlosser MJ, van Zijl PCM, Pomper MG, Golay X, Zhou J. Amide proton transfer imaging of human brain tumors at 3T. Magnetic Resonance in Medicine 2006;56:585–92. https://doi.org/10.1002/MRM.20989.
[58] Zhou J, Blakeley J, Hua J, Kim M, Laterra J, Pomper M, et al. Practical data acquisition method for human brain tumor amide proton transfer (APT) imaging. Magnetic Resonance in Medicine 2008;60:842–9. https://doi.org/10.1002/MRM.21712.
[59] Li S, Dardzinski B, Collins C, Yang Q, Smith M. Three-dimensional mapping of the static magnetic field inside the human head. Magnetic Resonance in Medicine 1996;36:705–14. https://doi.org/10.1002/MRM.1910360509.
[60] Parizel PM, van den Hauwe L, de Belder F, van Goethem J, Venstermans C, Salgado R, et al. Magnetic resonance imaging of the brain. Clinical MR Imaging: A Practical Approach. 3rd ed., Berlin: Springer Berlin Heidelberg; 2010, p. 107–95. https://doi.org/10.1007/978-3-540-74504-4_2.
[61] Iskurt A, Becerikli Y, Mahmutyazicioglu K. Automatic identification of landmarks for standard slice positioning in brain MRI. Journal of Magnetic Resonance Imaging 2011;34:499–510. https://doi.org/10.1002/JMRI.22717.
[62] Nigro S, Cerasa A, Zito G, Perrotta P, Chiaravalloti F, Donzuso G, et al. Fully Automated Segmentation of the Pons and Midbrain Using Human T1 MR Brain Images. PLOS ONE 2014;9:e85618. https://doi.org/10.1371/JOURNAL.PONE.0085618.
[63] Oba H, Yagishita A, Terada H, Barkovich AJ, Kutomi K, Yamauchi T, et al. New and reliable MRI diagnosis for progressive supranuclear palsy. Neurology 2005;64:2050–5. https://doi.org/10.1212/01.WNL.0000165960.04422.D0.
[64] Bach Cuadra M, Duay V, Thiran J-Ph. Atlas-based Segmentation. Handbook of Biomedical Imaging: Methodologies and Clinical Research, Boston: Springer, Boston, MA; 2015, p. 221–44. https://doi.org/10.1007/978-0-387-09749-7_12.
[65] Fonov V, Evans AC, Botteron K, Almli CR, McKinstry RC, Collins DL. Unbiased average age-appropriate atlases for pediatric studies. NeuroImage 2011;54:313–27. https://doi.org/10.1016/J.NEUROIMAGE.2010.07.033.
[66] Fonov V, Evans A, McKinstry R, Almli C, Collins D. Unbiased nonlinear average age-appropriate brain templates from birth to adulthood. NeuroImage 2009;47:S102. https://doi.org/10.1016/S1053-8119(09)70884-5.
[67] Tohka J, Krestyannikov E, Dinov ID, MacKenzie Graham A, Shattuck DW, Ruotsalainen U, et al. Genetic algorithms for finite mixture model based voxel classification in neuroimaging. IEEE Transactions on Medical Imaging 2007;26:696–711. https://doi.org/10.1109/TMI.2007.895453.
[68] Jafari-Khouzani K, Paynabar K, Hajighasemi F, Rosen B. The effect of region of interest size on the repeatability of quantitative brain imaging biomarkers. IEEE Transactions on Bio-Medical Engineering 2019;66:864. https://doi.org/10.1109/TBME.2018.2860928.
[69] Klein S, Staring M, Murphy K, Viergever M, Pluim J. elastix: a toolbox for intensity-based medical image registration. IEEE Transactions on Medical Imaging 2010;29:196–205. https://doi.org/10.1109/TMI.2009.2035616.
[70] Shamonin D, Bron E, Lelieveldt B, Smits M, Klein S, Staring M. Fast parallel image registration on CPU and GPU for diagnostic classification of Alzheimer's disease. Frontiers in Neuroinformatics 2014;7. https://doi.org/10.3389/FNINF.2013.00050.
[71] Yushkevich P, Piven J, Hazlett H, Smith R, Ho S, Gee J, et al. User-guided 3D active contour segmentation of anatomical structures: significantly improved efficiency and reliability. NeuroImage 2006;31:1116–28. https://doi.org/10.1016/J.NEUROIMAGE.2006.01.015.
[72] Park K, Kim H, Park J, Shim W, Kim S, Smith S. Added value of amide proton transfer imaging to conventional and perfusion MR imaging for evaluating the treatment response of newly diagnosed glioblastoma. European Radiology 2016;26:4390–403. https://doi.org/10.1007/S00330-016-4261-2.
[73] Sartoretti T, Sartoretti E, Wyss M, Schwenk Á, Najafi A, Binkert C, et al. Amide Proton Transfer Contrast Distribution in Different Brain Regions in Young Healthy Subjects. Frontiers in Neuroscience 2019;0:520. https://doi.org/10.3389/FNINS.2019.00520.

[74] Arslanoglu A, Bonekamp D, Barker PB, Horská A. Quantitative proton MR spectroscopic imaging of the mesial temporal lobe. Journal of Magnetic Resonance Imaging 2004;20:772–8. https://doi.org/10.1002/JMRI.20195.
[75] Jacobs M, Horská A, van Zijl P, Barker P. Quantitative proton MR spectroscopic imaging of normal human cerebellum and brain stem. Magnetic Resonance in Medicine 2001;46:699–705. https://doi.org/10.1002/MRM.1248.
[76] Azevedo F, Carvalho L, Grinberg L, Farfel J, Ferretti R, Leite R, et al. Equal numbers of neuronal and nonneuronal cells make the human brain an isometrically scaled-up primate brain. The Journal of Comparative Neurology 2009;513:532–41. https://doi.org/10.1002/CNE.21974.
[77] Zhou J, Heo HY, Knutsson L, van Zijl PCM, Jiang S. APT-weighted MRI: Techniques, current neuro applications, and challenging issues. Journal of Magnetic Resonance Imaging 2019;50:347–64. https://doi.org/10.1002/JMRI.26645.
[78] Afacan O, Erem B, Roby DP, Roth N, Roth A, Prabhu SP, et al. Evaluation of motion and its effect on brain magnetic resonance image quality in children. Pediatric Radiology 2016;46:1728. https://doi.org/10.1007/S00247-016-3677-9.
[79] Msayib Y, Harston GWJ, Tee YK, Sheerin F, Blockley NP, Okell TW, et al. Quantitative CEST imaging of amide proton transfer in acute ischaemic stroke. NeuroImage : Clinical 2019;23:101833. https://doi.org/10.1016/J.NICL.2019.101833.
[80] Deshmane A, Zaiss M, Lindig T, Herz K, Schuppert M, Gandhi C, et al. 3D gradient echo snapshot CEST MRI with low power saturation for human studies at 3T. Magnetic Resonance in Medicine 2019;81:2412–23. https://doi.org/10.1002/MRM.27569.
[81] Vaughan J, Garwood M, Collins C, Liu W, DelaBarre L, Adriany G, et al. 7T vs. 4T: RF power, homogeneity, and signal-to-noise comparison in head images. Magnetic Resonance in Medicine 2001;46:24–30. https://doi.org/10.1002/MRM.1156.
[82] Wijnen JP, Scheenen TWJ, Klomp DWJ, Heerschap A. 31P Magnetic resonance spectroscopic imaging with polarisation transfer of phosphomono- and diesters at 3 T in the human brain: relation with age and spatial differences. NMR in Biomedicine 2010;23:968–76. https://doi.org/10.1002/NBM.1523.
[83] Wijnen JP, Scheenen TWJ, Klomp DWJ, Heerschap. A. e. Combined 31P and 1H Magnetic Resonance Spectroscopic Imaging of phosphomono- and diesters in human brain tumors at 3T. International Society for Magnetic Resonance in Medicine, Stockholm: 2010.
[84] Jahng G-HJ-H. Physical Modeling of Chemical Exchange Saturation Transfer Imaging. Progress in Medical Physics 2017;28:135–43. https://doi.org/10.14316/PMP.2017.28.4.135.

Appendices

Appendix A: Lorentzian fitting parameters

APTw maps can be subtracted from the z-spectrum by using the Lorentzian fitting metrics. To apply this metric, parameters need to be predefined. For the Lorentzian fitting of acquisition with a full z-spectrum different parameters are defined for 5-pool and 6-pool Lorentzian fitting at 3T (*Table A.1* and *Table A.2* respectively) and 7T (*Table A.3* and *Table A.4* respectively)[24][39][80][84].

Table A.1: Fitting parameters for 5-pool Lorentzian fitting at 3T [24][80].

	Start	Lower	Upper
A_{water}	0.45	0.0045	1.0
Γ_{water}	2.2	1.1	4.4
δ_{water}	0.0	-1.0	1.0
A_{MT}	0.15	0.0015	1.0
Γ_{MT}	40	20	80
δ_{MT}	-1.5	-1.65	-1.35
A_{amide}	0.05	0.0005	0.5
Γ_{amide}	1.0	0.5	2.0
δ_{amide}	3.5	3.15	3.85
A_{NOE}	0.0	0.0	0.01
Γ_{NOE}	0.0	0.0	2.0
δ_{NOE}	-3.5	-3.85	-3.15
A_{amine}	0.025	0.0005	0.5
Γ_{amine}	1.0	0.5	2.0
δ_{amine}	2.0	1.8	2.2

A is the amplitude. The chemical shift δ and FWHM Γ are given in ppm.

Table A.2: Fitting parameters for 6-pool Lorentzian fitting at 3T [24][80][84].

	Start	Lower	Upper
A_{water}	0.85	0.0085	1.0
Γ_{water}	0.5	0.25	1.0
δ_{water}	0.0	-1.0	1.0
A_{MT}	0.15	0.0015	1.0
Γ_{MT}	40	20	80
δ_{MT}	-1.5	-1.65	-1.35
A_{amide}	0.05	0.0005	0.5
Γ_{amide}	1.0	0.5	2.0
δ_{amide}	3.5	3.15	3.85
A_{NOE}	0.0	0.0	0.01
Γ_{NOE}	0.0	0.0	2.0
δ_{NOE}	-3.5	-3.85	-3.15
A_{amine}	0.025	0.0005	0.5
Γ_{amine}	1.0	0.5	2.0
δ_{amine}	2.0	1.8	2.2
$A_{hydroxyl}$	0.02	0.0002	0.2
$\Gamma_{hydroxyl}$	0.2	0.0	0.9
$\delta_{hydroxyl}$	0.9	0.8	1.0

A is the amplitude. The chemical shift δ and FWHM Γ are given in ppm.

Table A.3: Fitting parameters for 5-pool Lorentzian fitting at 7T [39].

	Start	Lower	Upper
A_{water}	0.9	0.02	1.0
Γ_{water}	1.4	0.3	10
δ_{water}	0.0	-1.0	1.0
A_{MT}	0.1	0.0	1.0
Γ_{MT}	25	10	100
δ_{MT}	-2.0	-4.0	-2.0
A_{amide}	0.025	0.0	0.2
Γ_{amide}	0.5	0.4	3.0
δ_{amide}	3.5	3.0	4.0
A_{NOE}	0.02	0.0	0.4
Γ_{NOE}	3.0	1.0	5.0
δ_{NOE}	-3.5	-4.5	-2.0
A_{amine}	0.01	0.0	0.2
Γ_{amine}	0.5	0.4	3.0
δ_{amine}	2.2	1.0	2.5

A is the amplitude. The chemical shift δ and FWHM Γ are given in ppm.

Table A.4: Fitting parameters for 6-pool Lorentzian fitting at 7T [39][84].

	Start	Lower	Upper
A_{water}	0.9	0.02	1.0
Γ_{water}	1.4	0.3	10
δ_{water}	0.0	-1.0	1.0
A_{MT}	0.1	0.0	1.0
Γ_{MT}	25	10	100
δ_{MT}	-2.0	-4.0	-2.0
A_{amide}	0.025	0.0	0.2
Γ_{amide}	0.5	0.4	3.0
δ_{amide}	3.5	3.0	4.0
A_{NOE}	0.02	0.0	0.4
Γ_{NOE}	3.0	1.0	5.0
δ_{NOE}	-3.5	-4.5	-2.0
A_{amine}	0.01	0.0	0.2
Γ_{amine}	0.5	0.4	3.0
δ_{amine}	2.2	1.0	2.5
$A_{hydroxyl}$	0.01	0.0001	0.1
$\Gamma_{hydroxyl}$	0.2	0.0	0.9
$\delta_{hydroxyl}$	0.9	0.8	1.0

A is the amplitude. The chemical shift δ and FWHM Γ are given in ppm.

Appendix B: WASABI acquisition and processing

Water frequency shift and B_1 (WASABI) amplitude mapping can be obtained simultaneously by using the WASABI acquisition based on Rabi oscillations [51]. The WASABI spectra were acquired with a gradient echo sequence. It consist of two short preparation pulse of 2.5 ms (total pulse duration of 5 ms) with an RF amplitude of B_1=3.78 µT. Acquisition is performed for 31 frequency offsets sampled equidistantly between Δω = ±1.5 ppm, and a far offset at Δω = 600 ppm for normalization. The imaging parameters were TR = 3.75 ms; TE = 1.8 ms; matrix = 128 x 128 x 12; FOV = 256 x 256 x 24 mm; resolution = 2.0 x 2.0 x 2.0 mm; flip angle = 5°. The WASABI spectra consist of a oscillation pattern which can be described by Equation B.1 [51].

$$Z(\Delta\omega) = ||c - d \cdot \sin^2\left(\tan^{-1}\left(\frac{\gamma \cdot B_1}{\Delta\omega - \delta\omega}\right)\right) \cdot \sin^2\left(\sqrt{(\gamma \cdot B_1)^2 + (\Delta\omega - \delta\omega)^2} \cdot \frac{t_p}{2}\right)|| \quad \text{(B.1)}$$

With known input parameters $\Delta\omega$ is the radiofrequency offset relative to the Larmor frequency, $Z(\Delta\omega)$ is the z-magnetization, γ is the gyromagnetic ratio and t_p the pulse duration. The c and d parameters consider the relaxation and magnetization influences characteristic for the pulse. B_0-inhomogeneity is defined as the shift ($\delta\omega$) of the direct water saturation with respect to 0 ppm. The B_1-inhomogeneity can be characterised by the periodicity of the WASABI spectrum [51]. Figure X gives an example of a WASABI spectrum. By acquisition of a WASABI spectrum and fitting with Equation B.1, $\delta\omega$ and B_1 can be acquired simultaneously.

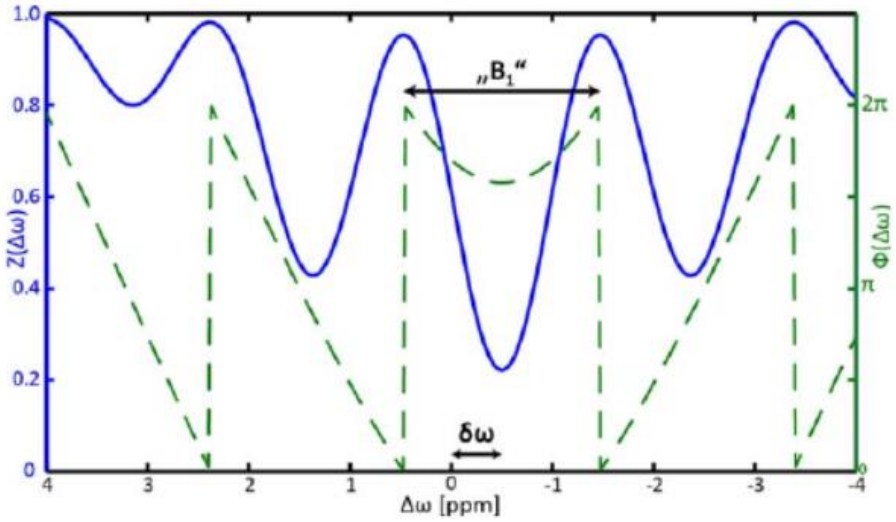

Figure B.1: Simulated WASABI z-spectrum at 3T with tp = 5 ms and B_1 = 3.7 µT. The spectrum gives information about the B_0 shift (δω) and the RF amplitude (B_1) encoded by the periodic change. [50]

To fit the WASABI spectra, free available MATLAB script from M. Zaiss were adopted. After normalization of the WASABI spectrum, a lookup table was created for all possible combination of the c, d, $\delta\omega$ and B_1. The parameter settings for the lookup table were defined by *Schuenke et al*. (c = [0.2:0.05:1]; d= [0.5:0.1:2.0]; $\delta\omega$= [-1:0.025:1]; B_1=[1.0:0.15:5.55]) [50]. The combination of parameters showing the smallest difference between the measured and simulated z-spectrum was determined for each voxel individually. Thereafter, fitting of equation B.1 was performed by using the parameters of the previous step as starting points [51]. The fitting results in c, d, $\delta\omega$ and B_1maps. Typical examples of the resulting B_0- and B_1- map belonging to the WASABI acquisition performed in the repeatability study, are present for the supratentorial and infratentorial brain in Figure B.2 and Figure B.3 respectively.

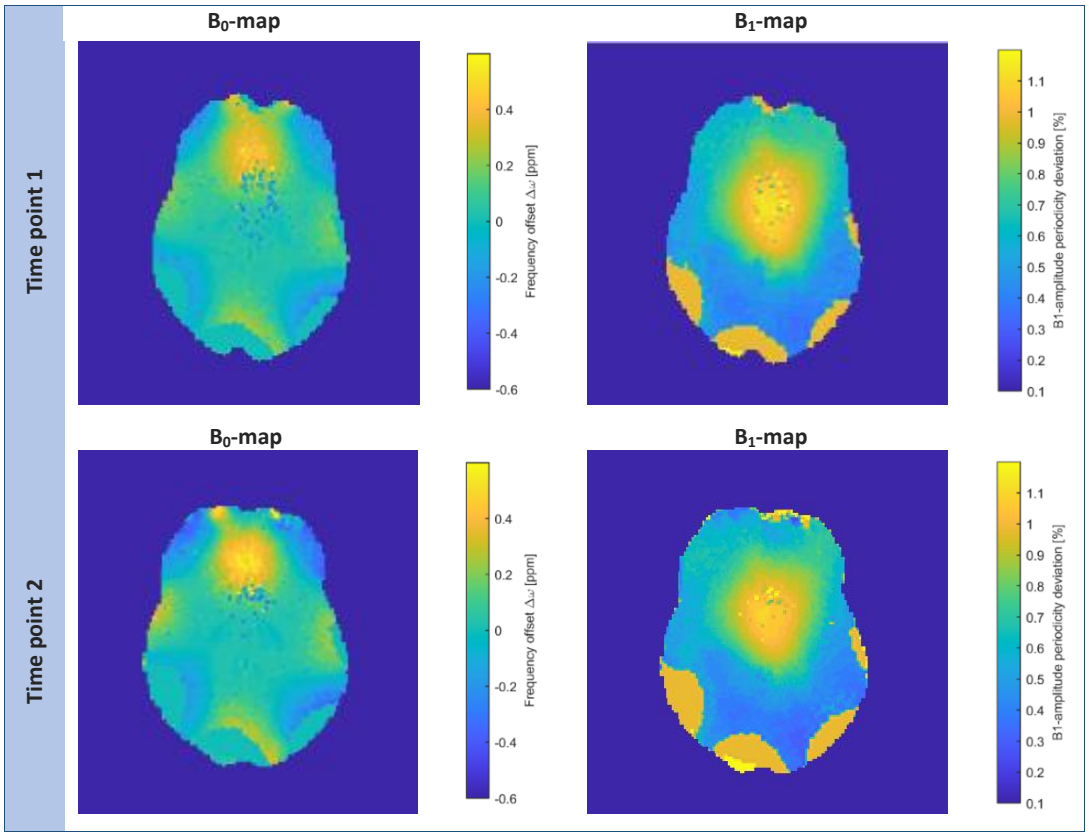

Figure B.2: B_0- and B_1- map belonging to the WASABI acquisition of the supratentorial brain at time point 1 (upper row) and time points 2 (lower row)

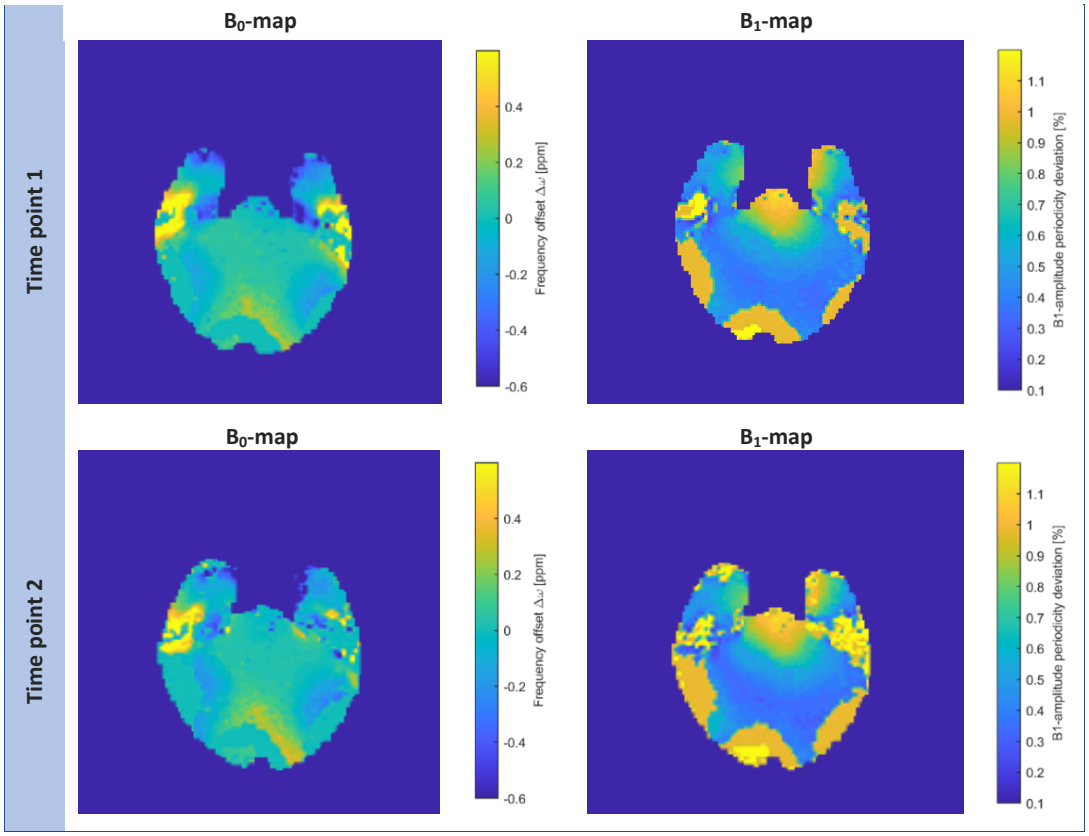

Figure B.3: B_0- and B_1- map belonging to the WASABI acquisition of the infratentorial brain at time point 1 (upper row) and time points 2 (lower row)

Appendix C: Detailed z-spectra of the phantom

Figure C.1 and C.2 show the normalized and B_0-corrected z-spectra acquired with the full z-spectrum acquisition corresponding to the individual ROIs (i.e. 20 mM NAM, 50 mM NAM, 100 mM NAM, 10 mM Glu and 20 mM Gly) and the two acquisition sessions at 3T and 7T respectively.

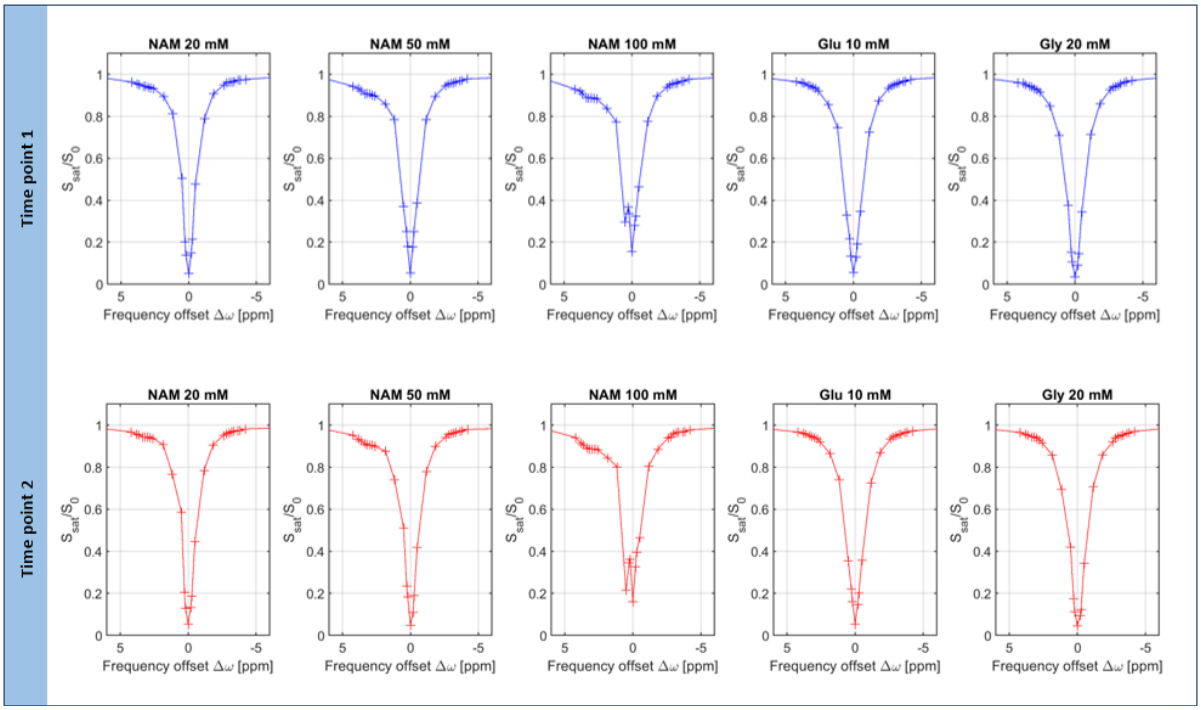

Figure C.1: Visualization of the full z-spectrum acquisition at 3T. Z-spectra are present for the five different ROIs. The upper part (blue z-spectra) are the z-spectra measured at time point 1 and the lower part (red z-spectra) are the z-spectra measured at time point 2.

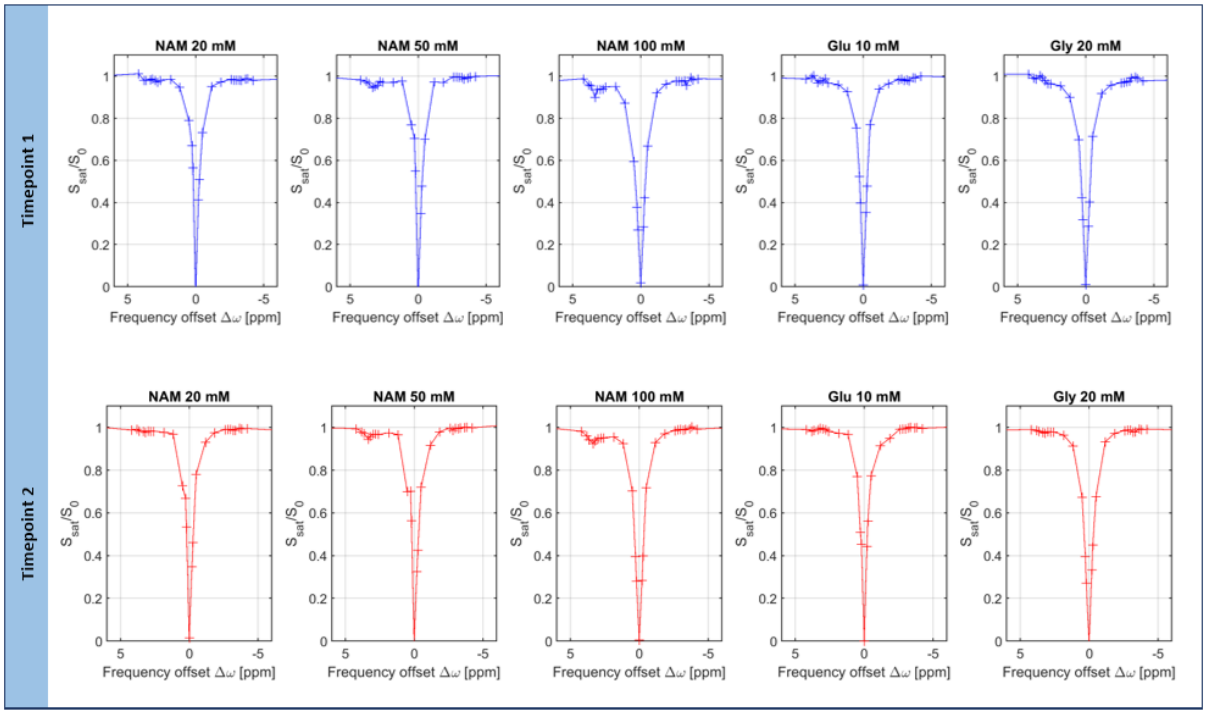

Figure C.2: Visualization of the full z-spectrum acquisition at 7T. Z-spectra are present for the five different ROIs. The upper part (blue z-spectra) are the z-spectra measured at time point 1 and the lower part (red z-spectra) are the z-spectra measured at time point 2.

Appendix D: Specification structuring elements morphological operations

Table D.1 listed the dimensional characteristics, diameter in pixels, of the elliptical structuring elements used to create small WM segments by morphological operations.

Table D.1: Diameter structuring elements depending on brain regions and type of morphological operation

	Opening/closing				Erosion		
	x	y	z		x	y	z
Frontal lobe	15	15	15		12	12	12
Parietal lobe	15	15	15		3	3	10
Cerebellum	10	10	10		4	4	3
Pons*	22	22	8		20	20	3

*Before opening/closing an additional closing is performed to merge left and right segment of the pons (size structuring element: 4 4 4)

Appendix E: Pipeline to obtain GM and WM masks for brain lobes

Figure E.1 show the pipeline to obtain maskers of GM and WM for the different brain lobes in the MNI-152 nonlinear symmetric atlas.

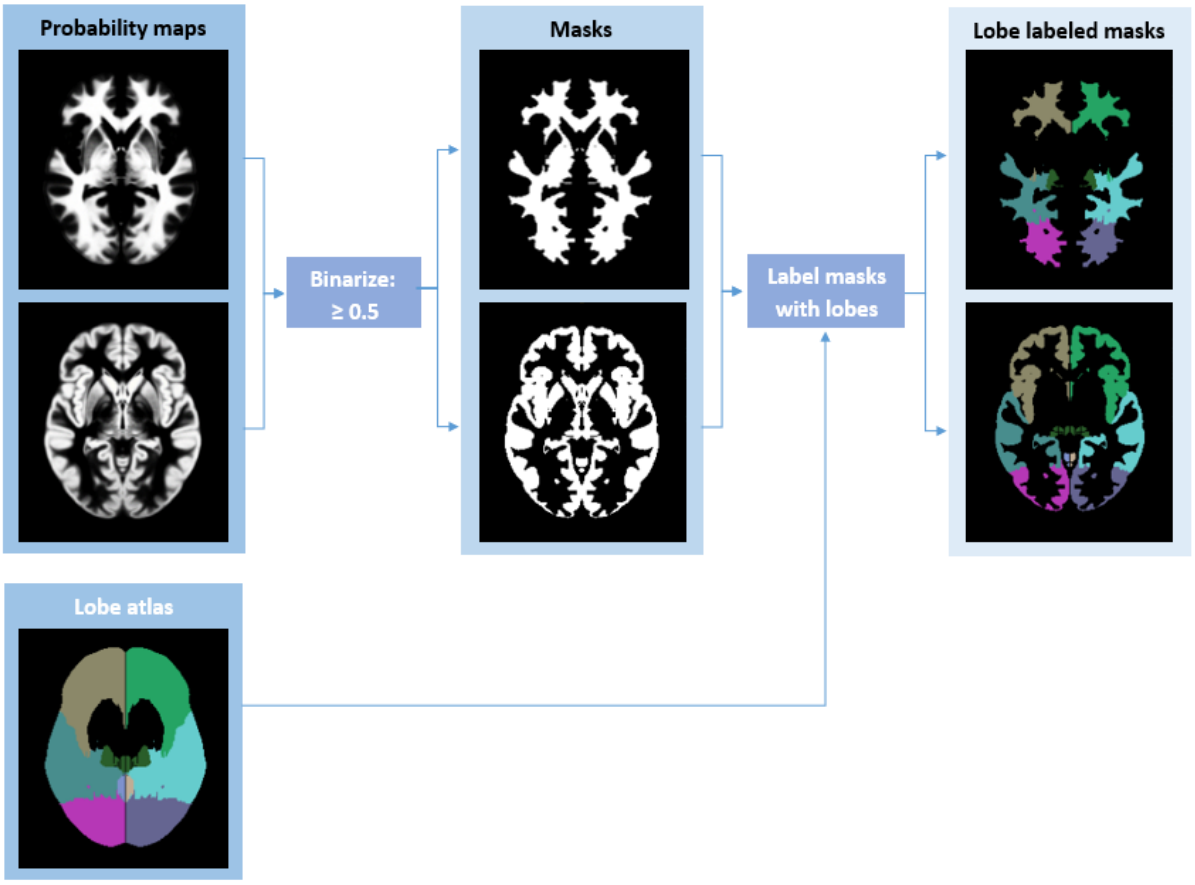

Figure E.1: Multiple steps to obtain lobe labelled masks of GM and WM by combining probability maps and labels of brain lobes available in the MNI-152 nonlinear symmetric atlas.

Appendix F: Parameter files registration

To perform atlas-based segmentation, multiple registration steps are performed. Appendix F.1 includes the parameter files corresponding to the registration of T1w image of the MNI-152 atlas to the T1w image of the subject. Appendix F.2 contains the parameters files belonging to the registration of T1w image of the subject to the unsaturated z-spectral image for 3T and 7T.

F.1 Registration of T1w image MNI-152 atlas to T1w image subject

F.1.1 Parameter file rigid transform

```
//ImageTypes
(FixedInternalImagePixelType "float")
(FixedImageDimension 3)
(MovingInternalImagePixelType "float")
(MovingImageDimension 3)

(UseDirectionCosines "true")

//Components
(Registration "MultiResolutionRegistration")
(FixedImagePyramid "FixedRecursiveImagePyramid")
(MovingImagePyramid "MovingRecursiveImagePyramid")

(Interpolator "BSplineInterpolator")
(Metric "AdvancedMattesMutualInformation")
(Optimizer "AdaptiveStochasticGradientDescent")
(ResampleInterpolator "FinalBSplineInterpolator")
(Resampler "DefaultResampler")
(Transform "EulerTransform")

(ErodeMask "false")
(NumberOfResolutions 4)
(FixedImagePyramidSchedule 8 4 8 4 2 4 2 1 2 1 1 1)
(MovingImagePyramidSchedule 4 4 4 2 2 2 1 1 1 1 1 1)

(HowToCombineTransforms "Compose")
(AutomaticTransformInitialization "true")
(AutomaticScalesEstimation "true")
(AutomaticTransformInitializationMethod "CenterOfGravity" )

(WriteTransformParametersEachIteration "false")
(WriteResultImage "true")
(CompressResultImage "false")
(WriteTransformParametersEachResolution "false")
(ShowExactMetricValue "false")
(ResultImagePixelType "short")
(ResultImageFormat "mhd")

//Maximum number of iterations in each resolution level:
(MaximumNumberOfIterations 1500)

//Number of grey level bins in each resolution level:
(NumberOfMovingHistogramBins 32)
(NumberOfFixedHistogramBins 32)

//Number of spatial samples used to compute the mutual information in each resolution
level:
(ImageSampler "RandomCoordinate")
(NumberOfSpatialSamples 2000)
(NewSamplesEveryIteration "true")
(MaximumNumberOfSamplingAttempts 15)
(MaximumStepLength 1)

//Order of B-Spline interpolation used in each resolution level:
(BSplineInterpolationOrder 3)
```

```
//Order of B-Spline interpolation used for applying the final deformation:
(FinalBSplineInterpolationOrder 3)

//Default pixel value for pixels that come from outside the picture:
(DefaultPixelValue 0)
```

F.1.2 Parameter file affine transform

```
//ImageTypes
(FixedInternalImagePixelType "float")
(FixedImageDimension 3)
(MovingInternalImagePixelType "float")
(MovingImageDimension 3)

(UseDirectionCosines "true")

//Components
(Registration "MultiResolutionRegistration")
(FixedImagePyramid "FixedSmoothingImagePyramid")
(MovingImagePyramid "MovingSmoothingImagePyramid")

(Interpolator "BSplineInterpolator")
(Metric "AdvancedMattesMutualInformation")
(Optimizer "AdaptiveStochasticGradientDescent")
(ResampleInterpolator "FinalBSplineInterpolator")
(Resampler "DefaultResampler")
(Transform "AffineTransform")

(ErodeMask "false")
(NumberOfResolutions 4)

(FixedImagePyramidSchedule 8 4 8 4 2 4 2 1 2 1 1 1)
(MovingImagePyramidSchedule 4 4 4 2 2 2 1 1 1 1 1 1)

(HowToCombineTransforms "Compose")
(AutomaticScalesEstimation "true")

(WriteTransformParametersEachIteration "false")
(WriteTransformParametersEachResolution "false")
(WriteResultImage "true")
(CompressResultImage "false")
(ShowExactMetricValue "false")
(ResultImagePixelType "short")
(ResultImageFormat "mhd")

//Maximum number of iterations in each resolution level:
(MaximumNumberOfIterations 1500)

//Number of grey level bins in each resolution level:
(NumberOfMovingHistogramBins 32)
(NumberOfFixedHistogramBins 32)

//Number of spatial samples used to compute the mutual information in each resolution
level:
(ImageSampler "RandomCoordinate")
(NumberOfSpatialSamples 2000)
(NewSamplesEveryIteration "true")
(MaximumNumberOfSamplingAttempts 8)
(MaximumStepLength 2)

//Order of B-Spline interpolation used in each resolution level:
(BSplineInterpolationOrder 3)

//Order of B-Spline interpolation used for applying the final deformation:
(FinalBSplineInterpolationOrder 3)
```

```
//Default pixel value for pixels that come from outside the picture:
(DefaultPixelValue 0)
```

F.1.3 Parameter file Bspline transform

```
//ImageTypes
(FixedInternalImagePixelType "float")
(FixedImageDimension 3)
(MovingInternalImagePixelType "float")
(MovingImageDimension 3)

(UseDirectionCosines "true")

//Components
(Registration "MultiResolutionRegistration")
(FixedImagePyramid "FixedSmoothingImagePyramid")
(MovingImagePyramid "MovingSmoothingImagePyramid")

(Interpolator "BSplineInterpolator")
(Metric "AdvancedMattesMutualInformation")
(Optimizer "StandardGradientDescent")
(ResampleInterpolator "FinalBSplineInterpolator")
(Resampler "DefaultResampler")
(Transform "BSplineTransform")

(ErodeMask "false")
(NumberOfResolutions 4)
(FixedImagePyramidSchedule 8 4 8 4 2 4 2 1 2 1 1 1)
(MovingImagePyramidSchedule 4 4 4 2 2 2 1 1 1 1 1 1)
(FinalGridSpacingInPhysicalUnits 5.0 5.0 5.0)

(HowToCombineTransforms "Compose")
//(AutomaticTransformInitialization "true")
//(AutomaticScalesEstimation "true")

(WriteTransformParametersEachIteration "false")
(WriteTransformParametersEachResolution "false")
(WriteResultImage "true")
(CompressResultImage "false")
(ShowExactMetricValue "false")
(ResultImagePixelType "short")
(ResultImageFormat "mhd")

//Maximum number of iterations in each resolution level:
(MaximumNumberOfIterations 2000)

//Number of grey level bins in each resolution level:
(NumberOfMovingHistogramBins 32)
(NumberOfFixedHistogramBins 32)

//Number of spatial samples used to compute the mutual information in each resolution
level:
(ImageSampler "RandomCoordinate")
(NumberOfSpatialSamples 2000)
(NewSamplesEveryIteration "true")
(MaximumNumberOfSamplingAttempts 8)

//Order of B-Spline interpolation used in each resolution level:
(BSplineInterpolationOrder 1)

//Order of B-Spline interpolation used for applying the final deformation:
(FinalBSplineInterpolationOrder 3)

//Default pixel value for pixels that come from outside the picture:
(DefaultPixelValue 0)

//SP: Param_a in each resolution level. a_k = a/(A+k+1)^alpha
(SP_a 10000)
```

```
//SP: Param_A in each resolution level. a_k = a/(A+k+1)^alpha
(SP_A 100.0 )

//SP: Param_alpha in each resolution level. a_k = a/(A+k+1)^alpha
(SP_alpha 0.600000)
```

F.2 Registration of anatomical image to unsaturated z-spectral image

F.2.1 Parameter file rigid transform for 3T

```
//ImageTypes
(FixedInternalImagePixelType "float")
(FixedImageDimension 3)
(MovingInternalImagePixelType "float")
(MovingImageDimension 3)

(UseDirectionCosines "true")

//Components
(Registration "MultiResolutionRegistration")
(FixedImagePyramid "FixedRecursiveImagePyramid")
(MovingImagePyramid "MovingRecursiveImagePyramid")

(Interpolator "BSplineInterpolator")
(Metric "AdvancedMattesMutualInformation")
(Optimizer "AdaptiveStochasticGradientDescent")
(ResampleInterpolator "FinalBSplineInterpolator")
(Resampler "DefaultResampler")
(Transform "EulerTransform")

(ErodeMask "false")
(NumberOfResolutions 6)

(FixedImagePyramidSchedule 16 16 2 8 8 1  4 4 1  2 2 1  1 1 1  1 1 1)
(MovingImagePyramidSchedule 32 16 24  16 8 12  8 4 12  4 2 6  2 1 2  1 1 1)

(HowToCombineTransforms "Compose")
(AutomaticParameterEstimation "true")
(AutomaticTransformInitialization "true")
(AutomaticScalesEstimation "true")
(AutomaticTransformInitializationMethod "CenterOfGravity" )

(WriteTransformParametersEachIteration "false")
(WriteResultImage "true")
(CompressResultImage "false")
(WriteTransformParametersEachResolution "false")
(ShowExactMetricValue "false")
(ResultImagePixelType "short")
(ResultImageFormat "mhd")

//Maximum number of iterations in each resolution level:
(MaximumNumberOfIterations 2000)


//Number of grey level bins in each resolution level:
(NumberOfHistogramBins 32)
(NumberOfMovingHistogramBins 32)
(NumberOfFixedHistogramBins 32)

//Number of spatial samples used to compute the mutual information in each resolution
level:
(ImageSampler "RandomCoordinate")
(NumberOfSpatialSamples 5000)
(MaximumNumberOfSamplingAttempts 15)
(NewSamplesEveryIteration "true")
(CheckNumberOfSamples "true")

//Order of B-Spline interpolation used in each resolution level:
(BSplineInterpolationOrder 3)
```

```
//Order of B-Spline interpolation used for applying the final deformation:
(FinalBSplineInterpolationOrder 3)

//Default pixel value for pixels that come from outside the picture:
(DefaultPixelValue 0)
```

F.2.2 Parameter file rigid transform for 7T

```
//ImageTypes
(FixedInternalImagePixelType "float")
(FixedImageDimension 3)
(MovingInternalImagePixelType "float")
(MovingImageDimension 3)

(UseDirectionCosines "true")

//Components
(Registration "MultiResolutionRegistration")
(FixedImagePyramid "FixedRecursiveImagePyramid")
(MovingImagePyramid "MovingRecursiveImagePyramid")

(Interpolator "BSplineInterpolator")
(Metric "AdvancedMattesMutualInformation")
(Optimizer "AdaptiveStochasticGradientDescent")
(ResampleInterpolator "FinalBSplineInterpolator")
(Resampler "DefaultResampler")
(Transform "EulerTransform")

(ErodeMask "false")
(NumberOfResolutions 6)

(FixedImagePyramidSchedule 16 16 2 8 8 1  4 4 1  2 2 1  1 1 1  1 1 1)
(MovingImagePyramidSchedule 32 16 8  16 8 4  8 4 4  4 2 2  2 1 1  1 1 1)

(HowToCombineTransforms "Compose")
(AutomaticParameterEstimation "true")
(AutomaticTransformInitialization "true")
(AutomaticScalesEstimation "true")
(AutomaticTransformInitializationMethod "CenterOfGravity" )

(WriteTransformParametersEachIteration "false")
(WriteResultImage "true")
(CompressResultImage "false")
(WriteTransformParametersEachResolution "false")
(ShowExactMetricValue "false")
(ResultImagePixelType "short")
(ResultImageFormat "mhd")

//Maximum number of iterations in each resolution level:
(MaximumNumberOfIterations 2000)


//Number of grey level bins in each resolution level:
(NumberOfHistogramBins 32)
(NumberOfMovingHistogramBins 32)
(NumberOfFixedHistogramBins 32)

//Number of spatial samples used to compute the mutual information in each resolution level:
(ImageSampler "RandomCoordinate")
(NumberOfSpatialSamples 5000)
(MaximumNumberOfSamplingAttempts 15)
(NewSamplesEveryIteration "true")
(CheckNumberOfSamples "true")

//Order of B-Spline interpolation used in each resolution level:
(BSplineInterpolationOrder 3)

//Order of B-Spline interpolation used for applying the final deformation:
(FinalBSplineInterpolationOrder 3)

//Default pixel value for pixels that come from outside the picture:
(DefaultPixelValue 0)
```

Appendix G: Evaluation of registration in vivo study

Appendix G.1 and Appendix G.2 show the results of the different registration steps (i.e. T1w image (MNI-152 atlas) to T1w image of subject to unsaturated CEST image) at 3T and 7T for the supratentorial and infratentorial brain slab of one subject respectively.

G.1 Evaluation of registration supratentorial brain region

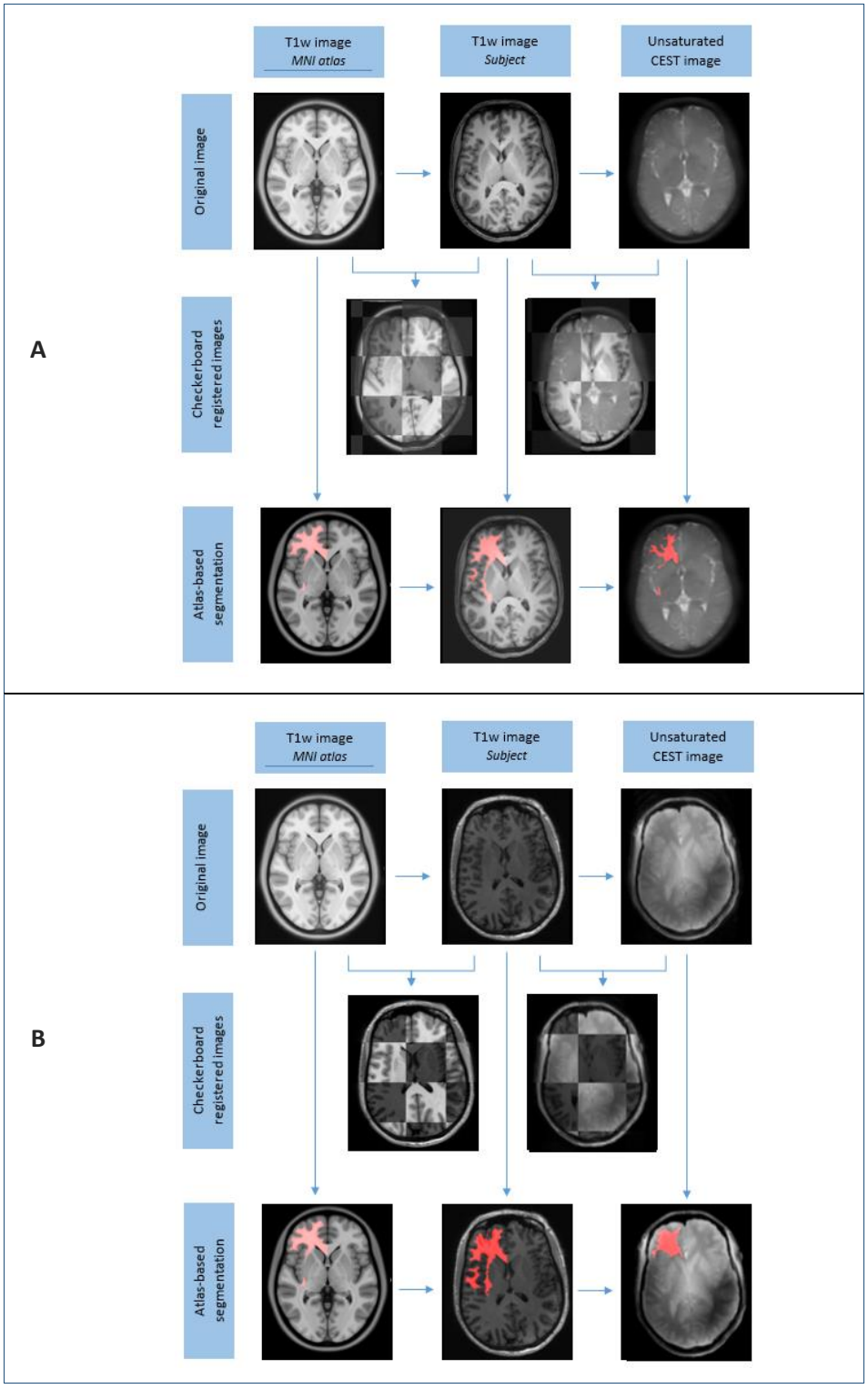

Figure G.1 Final registration results for the supratentorial slab of one subject at 3T (panel A) and 7T (panel B). First column; original images (left to right: T1w image MNI, T1w image subject and unsaturated CEST images). Second row; two steps of registration validation using checkerboard. Third row; registration of segment from MNI to CEST brain slab.

G.2 Evaluation of registration infratentorial brain

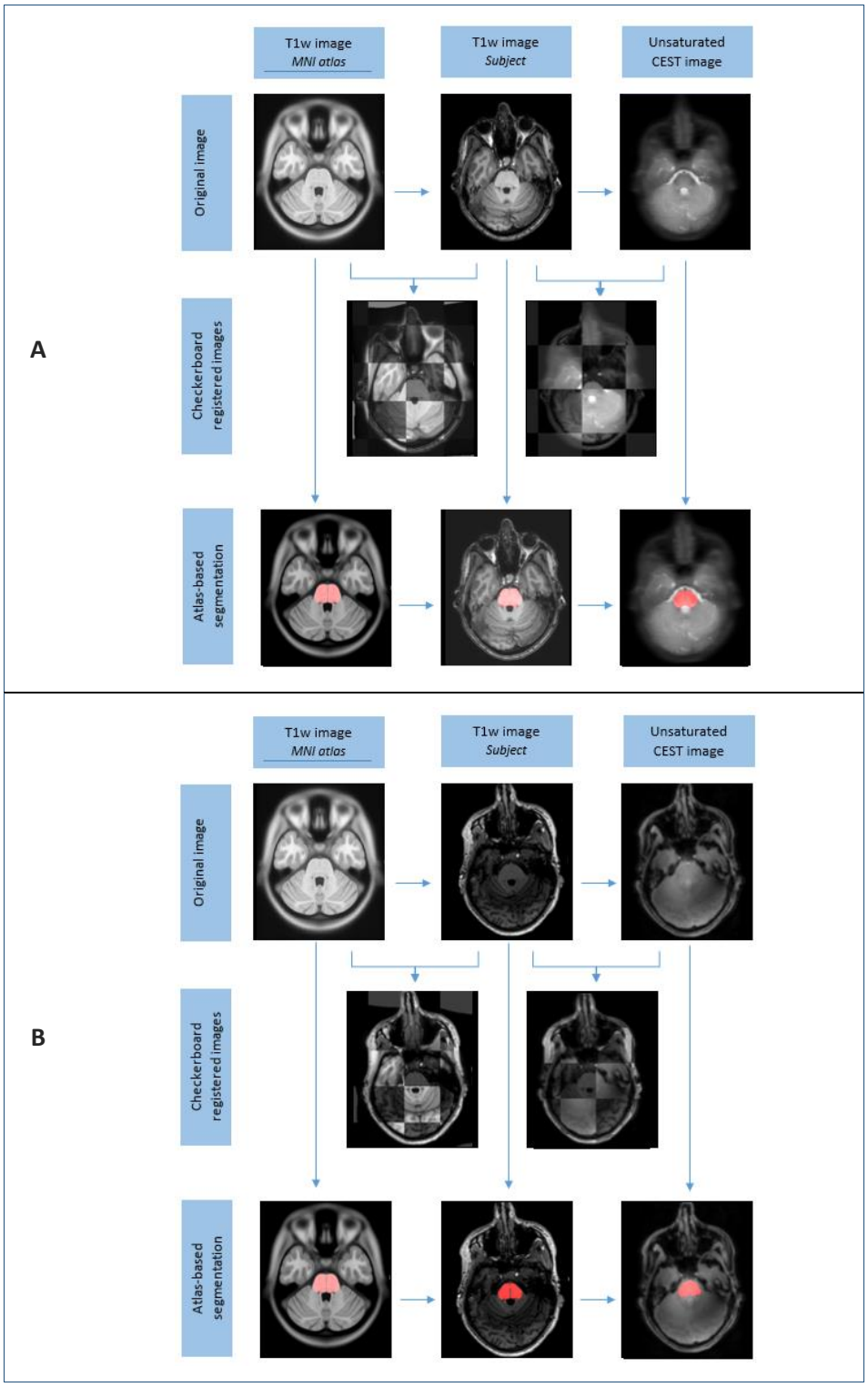

Figure G.2 Final registration results for the infratentorial slab of one subject at 3T (panel A) and 7T (panel B). First column; original images (left to right: T1w image MNI, T1w image subject and unsaturated CEST images). Second row; two steps of registration validation using checkerboard. Third row; registration of segment from MNI to CEST brain slab.

Appendix H: APTw values for subdivided supratentorial segments

Figure H.1 presents the boxplots to evaluate the repeatability of APTw values of the brain tissue segments belonging to the frontal and parietal lobe (i.e. supratentorial area). The corresponding repeatability metrics are present in Table H.1.

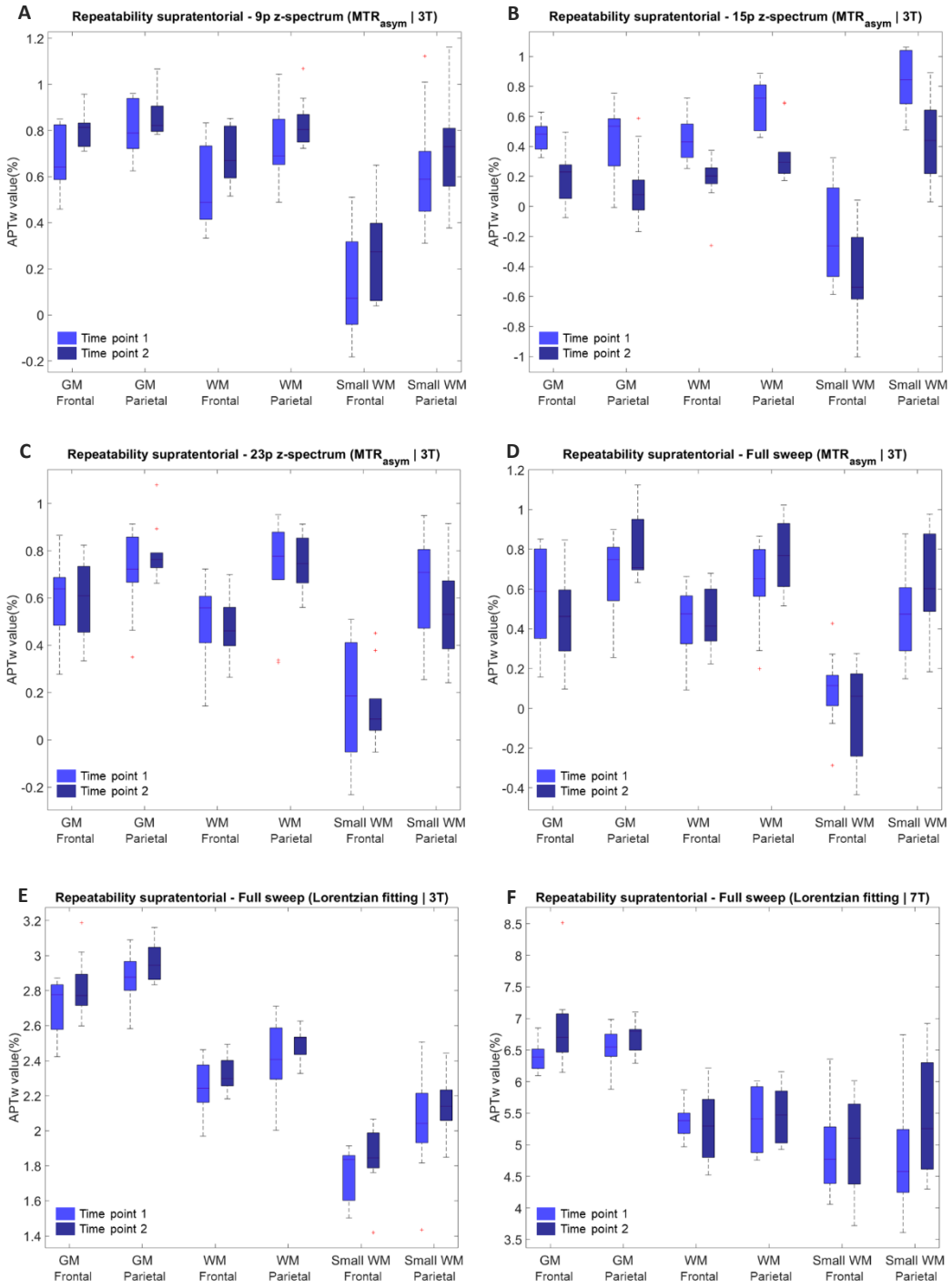

Figure H.1: Boxplots of the frontal and parietal lobe (i.e. supratentorial area) for the different APTw acquisition and processing methods (A-E: 3T, F: 7T) to evaluate the repeatability of APTw values within each segment.

Table H.1: APTw values (mean ± standard deviation) and repeatability metrics of the frontal and parietal lobe (i.e. supratentorial area) for the different APTw acquisitions and processing methods.

Magnetic field strength	Acquisition	Segment	APTw values (%) (mean ± STD)		RMSD	wCV (%)
			T=1	T-=2		
3T	9p z-spectrum*	GM frontal lobe	0.67±0.13	0.80±0.07	0.16	15.11
		GM parietal lobe	0.81±0.12	0.86±0.09	0.12	10.38
		WM frontal lobe	0.54±0.17	0.68±0.12	0.18	20.76
		WM parietal lobe	0.74±0.16	0.83±0.11	0.17	15.11
		Small WM frontal	0.12±0.23	0.29±0.22	0.21	74.35
		Small WM parietal	0.64±0.25	0.73±0.21	0.27	28.08
	15p z-spectrum*	GM frontal lobe	0.47±0.10	0.22±0.18	0.33	68.44
		GM parietal lobe	0.44±0.23	0.12±0.23	0.38	96.49
		WM frontal lobe	0.45±0.16	0.18±0.18	0.33	73.29
		WM parietal lobe	0.68±0.15	0.35±0.19	0.40	54.38
		Small WM frontal	-0.20±0.32	-0.47±0.34	0.40	-85.35
		Small WM parietal	0.82±0.20	0.44±0.26	0.46	51.42
	23p z-spectrum*	GM frontal lobe	0.20±0.17	0.59±0.17	0.11	13.59
		GM parietal lobe	0.71±0.18	0.79±0.12	0.19	18.33
		WM frontal lobe	0.50±0.19	0.48±0.13	0.15	21.79
		WM parietal lobe	0.72±0.22	0.75±0.12	0.23	21.97
		Small WM frontal	0.19±0.24	0.14±0.16	0.22	94.60
		Small WM parietal	0.65±0.23	0.55±0.21	0.32	37.13
	Full z-spectrum*	GM frontal lobe	0.55±0.24	0.47±0.23	0.21	29.50
		GM parietal lobe	0.66±0.21	0.82±0.19	0.37	35.18
		WM frontal lobe	0.43±0.18	0.45±0.15	0.27	43.55
		WM parietal lobe	0.63±0.22	0.77±0.18	0.34	35.01
		Small WM frontal	0.09±0.19	-0.01±0.24	0.19	341.60
		Small WM parietal	0.48±0.24	0.63±0.25	0.42	53.25
	Full z-spectrum+	GM frontal lobe	2.71±0.16	2.82±0.18	0.31	7.87
		GM parietal lobe	2.86±0.15	2.96±0.11	0.22	5.29
		WM frontal lobe	2.26±0.15	2.32±0.10	0.23	7.07
		WM parietal lobe	2.41±0.23	2.50±0.09	0.26	7.36
		Small WM frontal	1.76±0.15	1.84±0.18	0.16	6.53
		Small WM parietal	2.06±0.31	2.16±0.18	0.31	10.43
7T	Full z-spectrum+	GM frontal lobe	6.39±0.24	6.85±0.70	0.86	9.15
		GM parietal lobe	6.53±0.31	6.71±0.25	0.49	5.23
		WM frontal lobe	5.38±0.28	5.30±0.55	0.64	8.54
		WM parietal lobe	5.39±0.49	5.49±0.44	0.74	9.63
		Small WM frontal	4.88±0.72	4.97±0.76	1.07	15.42
		Small WM parietal	4.76±0.87	5.39±0.93	1.16	16.16

* z-spectrum processed with MTR_{asym}

+ z-spectrum processed with Lorentzian fitting

Appendix I: Overview of APTw maps in paediatric brain tumours

An overview of the registered FLAIR images (including tumour maskers) and APTw maps (full and specific for the tumour masks) are present for the different cases in Appendix I.1, I.2 and I.3. Furthermore, these appendices incorporate the histograms for the different tumour masks and scan sessions.

I.1 Additional results of case 1

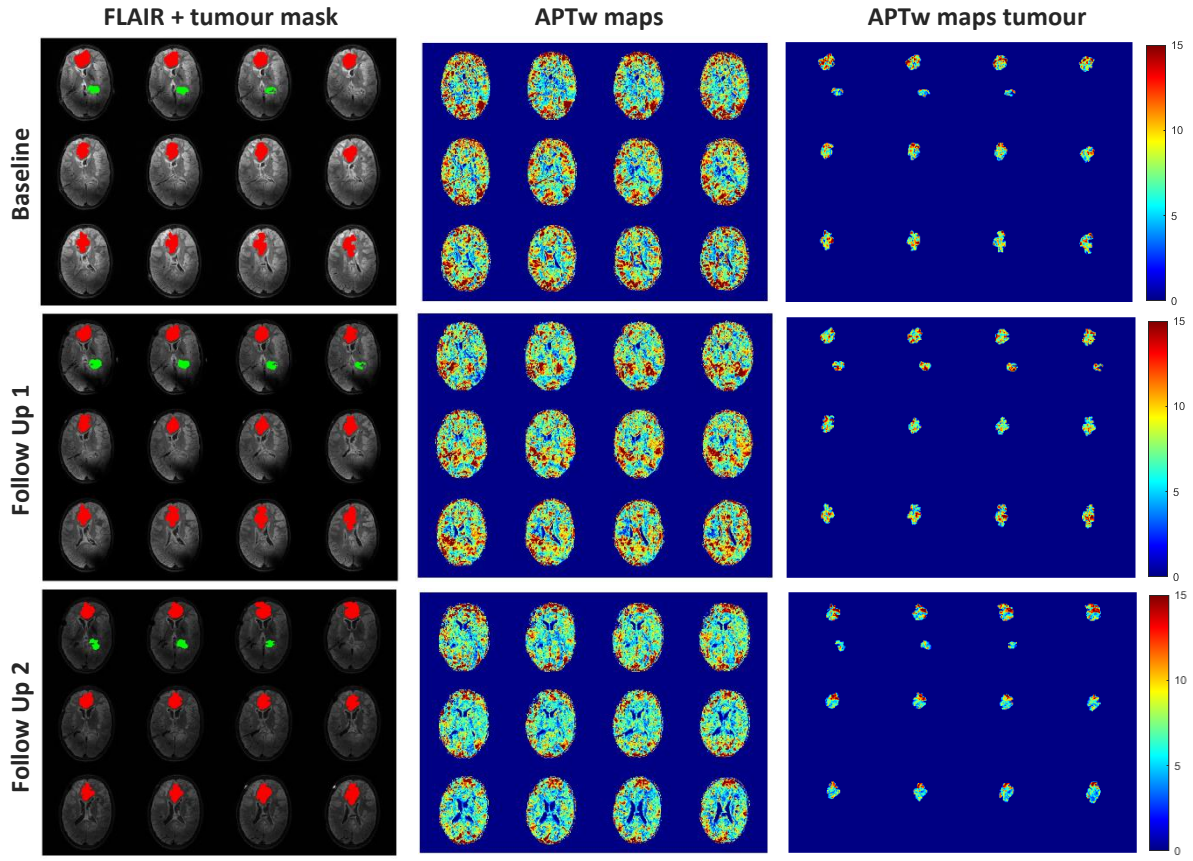

Figure I.1.1: Overview of FLAIR and APTw image of case 1 for all slices and scan session (baseline (first row), first follow-up (second row), second follow-up (third row). Registered FLAIR including tumour masks (first column), APTw image (second column) and APTw image excise for the tumour mask only (third column)

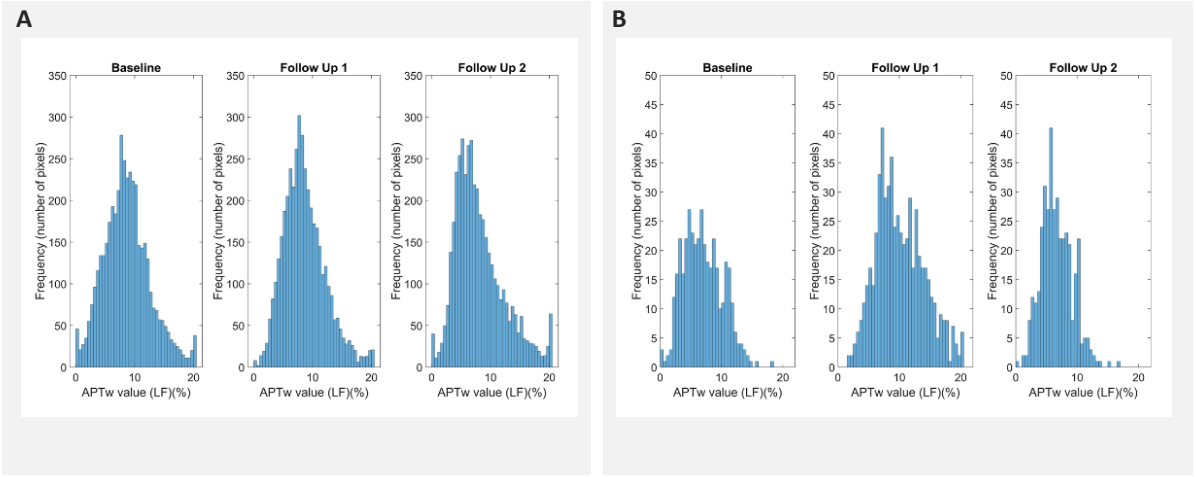

Figure I.1.2: Histograms corresponding to the baseline, first and second follow-up for two tumour areas (A: frontal tumour mask ; B: tumour mask of atrium area)

I.2 Additional results of case 2

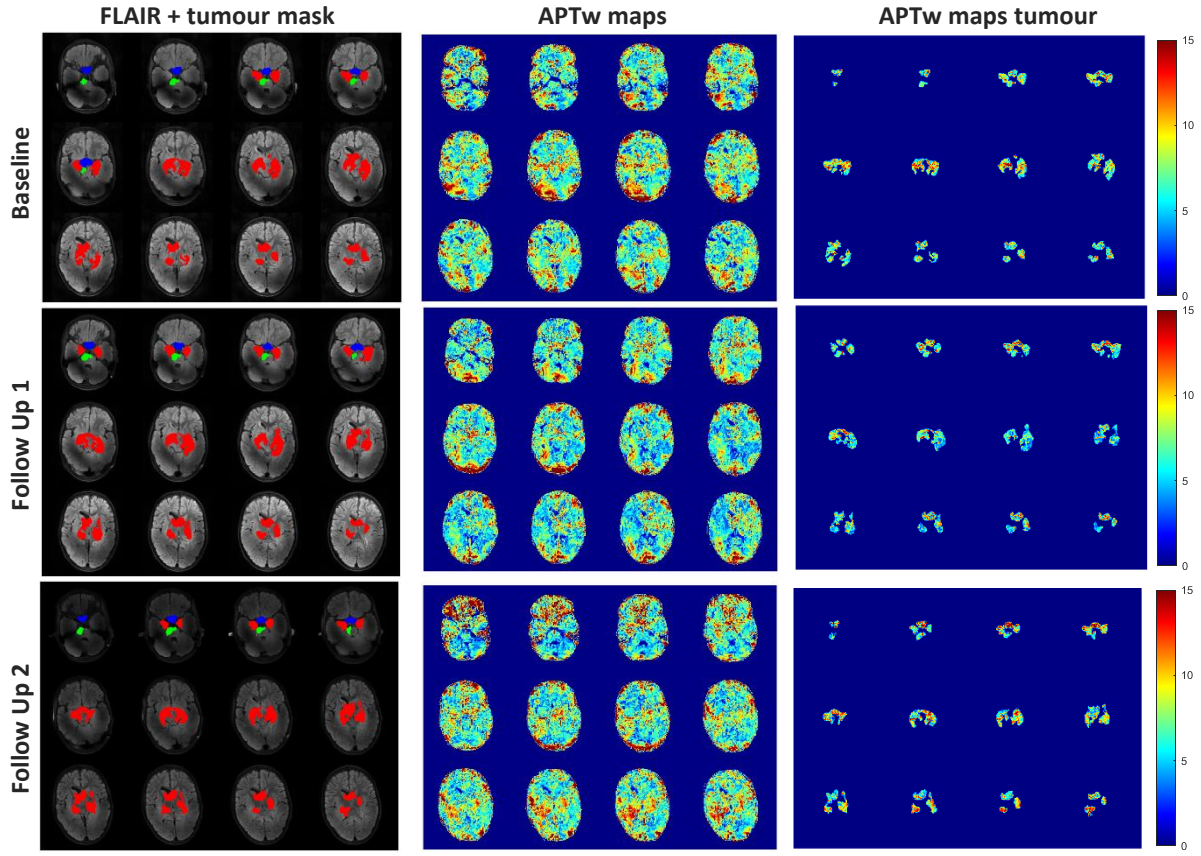

Figure I.2.1: Overview of FLAIR and APTw image of case 2 for all slices and scan session (baseline (first row), first follow-up (second row), second follow-up (third row). Registered FLAIR including tumour masks (first column), APTw image (second column) and APTw image excise for the tumour mask only (third column)

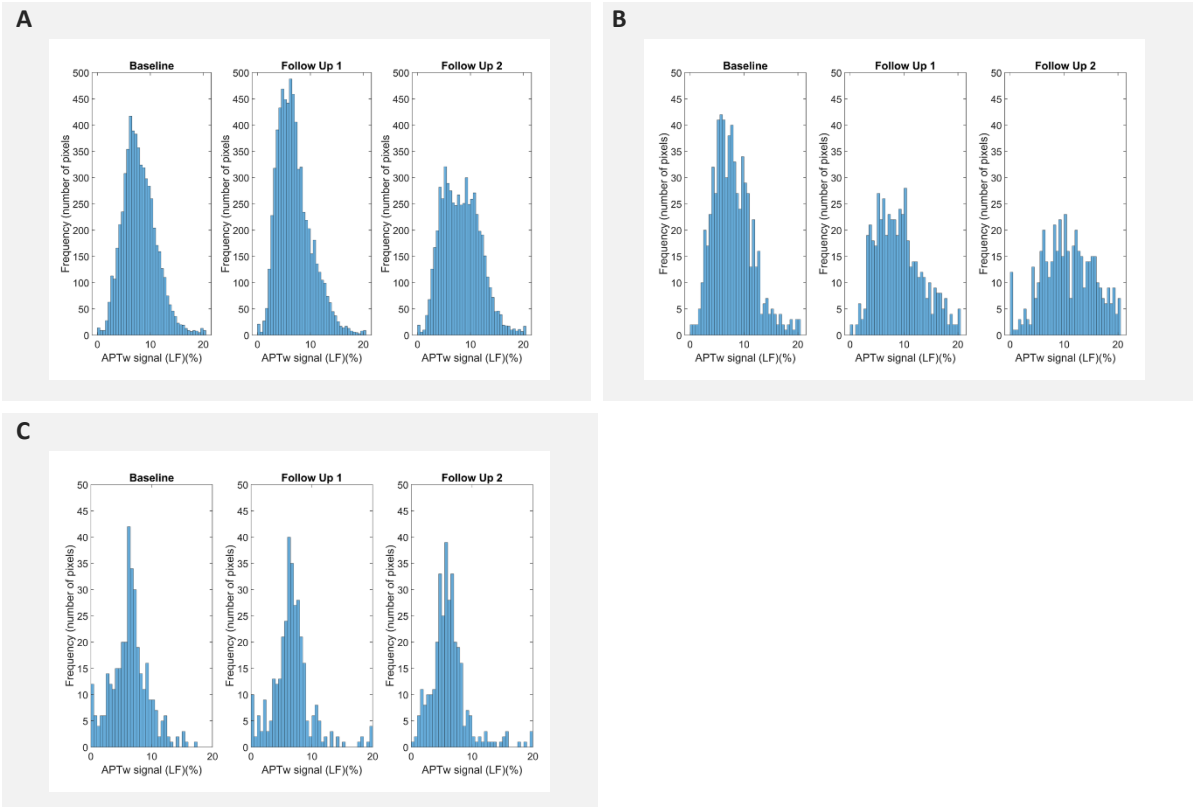

Figure I.2.2: Histograms corresponding to the baseline, first and second follow-up for three tumour areas (A: complete tumour mask; B: chiasmal tumour mask; C: pons tumour mask.

I.3 Additional results of case 3

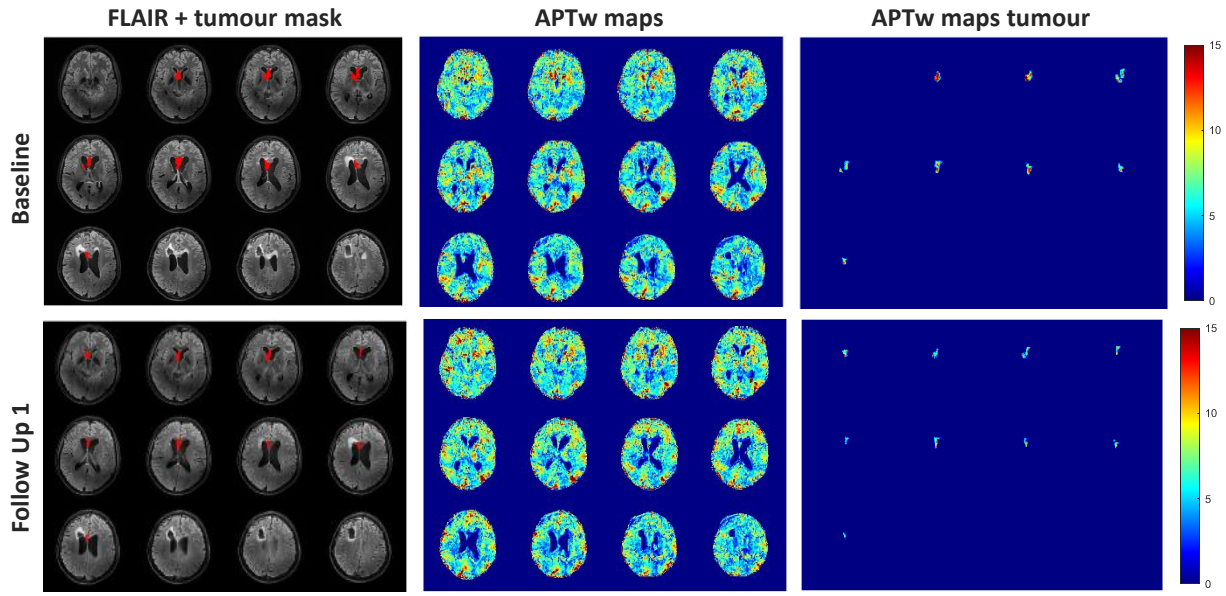

Figure I.3.1: Overview of FLAIR and APTw image of case 3 for all slices and scan session (baseline (first row), first follow-up (second row). Registered FLAIR including tumour masks (first column), APTw image (second column) and APTw image excise for the tumour mask only (third column)

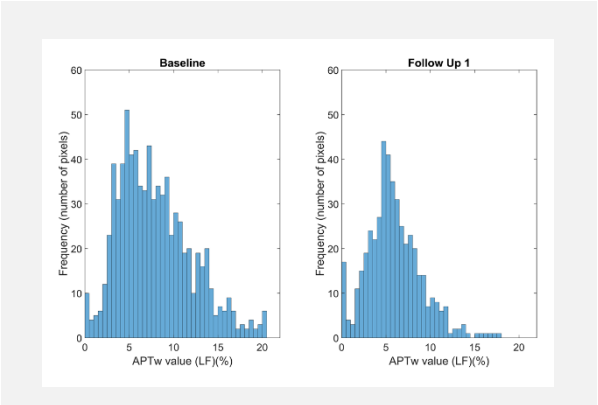

Figure I.3.2: Histograms corresponding to the baseline and first follow-up belonging to the tumour